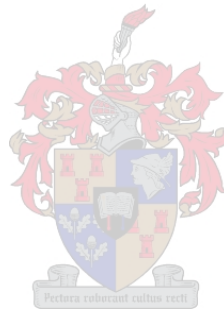


**Computational Fluid Dynamic Modelling of  
an Electric Smelting Furnace in the  
Platinum Recovery Process**

Johan Jacobus Bezuidenhout

Thesis submitted in fulfilment  
of the requirements for the Degree  
of



MASTER OF SCIENCE IN ENGINEERING  
(EXTRACTIVE METALLURGICAL ENGINEERING)  
in the Department of Process Engineering  
at Stellenbosch University

Supervised by:  
Prof. J.J. Eksteen and Prof S.M. Bradshaw

December 2008

## **Declaration**

By submitting this thesis electronically, I declare that the entirety of the work contained therein is my own, original work, that I am the owner of the copyright thereof (unless to the extent explicitly otherwise stated) and that I have not previously in its entirety or in part submitted it for obtaining any qualification.

Date: 17 December 2008

Copyright © 2008 Stellenbosch University

All rights reserved

# ABSTRACT

---

The electric smelting furnace is found at the heart of the platinum recovery process where the power input from the electrodes produces a complex interplay between heat transfer and fluid flow. A fundamental knowledge of the dynamic system hosted by the electric furnace is valuable for maintaining stable and optimum operation. However, describing the character of the system hosted by the electric furnace poses great difficulty due to its aggressive environment. A full-scale three-dimensional Computational Fluid Dynamics (CFD) model was therefore developed for the circular, three-electrode Lonmin smelting furnace.

The model was solved as time dependent to incorporate the effect of the three-phase AC current, which was supplied by means of volume sources representing the electrodes. The slag and matte layers were both modelled as fluid continuums in contact with each other through a dynamic interface made possible by the Volume of Fluid (VOF) multi-phase model. CO-gas bubbles forming at electrode surfaces and interacting with the surrounding fluid slag were modelled through the Discrete Phase Model (DPM).

To account for the effect of concentrate melting, distinctive smelting zones were identified within the concentrate as assigned a portion of the melting heat based on the assumption of a radially decreasing smelting rate from the centre of the furnace. The tapping of slag and matte was neglected in the current modelling approach but compensation was made for the heating-up of descending material by means of an energy sink based on enthalpy differences.

Model cases with and without CO-gas bubbles were investigated as well as the incorporation of a third phase between the slag and matte for representing the 'mushy' chromite/highly viscous slag commonly found in this region. These models were allowed to iterate until steady state conditions has been achieved, which for most of the cases involved several weeks of simulation time.

The results that were obtained provided good insight into the electrical, heat and flow behaviour present within the molten bath. The current density profiles showed a large portion of the current to flow via the matte layer between the electrodes. Distributions for the electric potential and Joule heat within the melt was also developed and showed the highest power to be generated within the immediate vicinity of the electrodes and 98% of the resistive heat to be generated within the slag.

Heat was found to be uniformly distributed due the slag layer being well mixed. The CO-gas bubbles was shown to be an important contributor to flow within the slag, resulting in a order of magnitude difference in average flow magnitude compared to the case where only natural buoyancy is at play.

The highest flow activity was observed halfway between electrodes where the flow streams from the electrodes meet. Consequently, the highest temperatures are also observed in these regions. The temperature distribution within the matte and concentrate layers can be characterized as stratified. Low flow regions were identified within the matte and bottom slag layer which is where chromite and magnetite deposits are prone to accumulate.

The model results were partially validated through good agreement to published results where actual measurements were done while also falling within the typical operating range for the actual furnace. The modelling of the electric furnace has been valuably furthered, however for complete confidence in the model results, further validation is strongly recommended.

# OPSOMMING

---

Die elektriese smeltoond word gevind in die hart van die platinum herwinningsproses waar die kragtoevoer vanaf die elektrodes 'n komplekse interaksie tussen warmte-oordrag en die vloeï van vloeistof veroorsaak. 'n Fundamentele kennis van die dinamiese sisteem wat deur die elektriese oond gehuisves word is van groot waarde vir die handhaaf van stabile en optimum bedryf. Ongelukkig is die beskrywing van die gesmelte massa se karakter baie moeilik weens sy uiterse omgewing. Om hierdie rede is 'n volskaalse, drie-dimensionele, berekeningsvloeïdinamiese model ontwikkel vir die ronde, drie-elektrode Lonmin smeltoond.

Die model is afhanklik van tyd opgelos om die drie-fasige karakter van die wisselstroom te inkorporeer. Die stroom is voorsien deur toevoeg-volumes wat die elektrodes voorstel. Beide die slak en die mat was as vloeïstowwe gemodelleer in kontak met mekaar deur 'n dinamiese tussenvlak wat moontlik gemaak is deur die Volume van Vloeïstof multi-fase model. CO-gas borrels wat by die elektrode oppervalk ontstaan en wisselerking uitoefen op die slak is deur die Diskrete multi-fase model gemodelleer.

Om die effek van konsentraat smelting in ag te neem, was duidelike smeltsones binne die konsentraat laag geïdentifiseer en 'n deel van die smeltenergie toegeken volgens die aanname van 'n afnemende smelt-tempo vanaf die middelpunt van die oond. Die tap van slak en mat was nie in ag geneem nie maar daar is daarvoor gekompenseer deur die opwarm van dalende materiaal as 'n energie sink te inkorporeer.

Modelle met en sonder CO-gas borrels was ondersoek sowel as 'n derde fase tussen die slak en mate om die taai chroom/hoë viskose slak, wat algemeen hier voorkom, voor te stel. Hierdie modelle was toegelaat om te itereer totdat gestadigde toestande bereik is, wat in die meeste gevalle etlike weke geneem het.

Die resultate wat verkry is het goeie insig in die elektriese, warmte en vloeï gedrag binne die gesmelte bad verleen. Die stroom digtheïdsprofiele toon 'n groot deel van die stroom om via die matlaag tussen die elektrodes te vloeï. Verspreidings van elektriese potensiaal en Joule hitte is ontwikkel binne die bad en toon dat die hoogste warmte in die direkte area rondom die elektrodes gegenereer word en ook dat 98% van die resestiewe hitte in die slak ontstaan.

'n Uniforme hitte verspreïding is bepaal as gevolg van die goed vermengde slak. Die CO-borrels is getoon om 'n groot bydrae tot die vloeï in die slak te lewer wat 'n ordegrootte toename in die

gemiddelde vloeigrootte tot gevolg het in vergelyking met die toestand waar slegs natuurlike konveksie ter sprake is.

Die hoogste vloeiaktiwiteit is bevind halfpad tussen die elektrodes waar die vloeistrome vanaf die elektrodes bymekaar kom. Gevolglik word die hoogste temperature in dié streke aangetref. Die temperatuur verspreiding in die mat en konsentraat laag toon 'n gelaagde profiel. Gebiede met lae vloei word aangetref in die mat en bodem van die slak waar chroom en magnetiet neerslae geneig is om te akkumuleer.

Die model resultate was gedeeltelik gevalideer deur goeie ooreenstemming met gepubliseerde resultate waar werklike metings gemaak was asook deur binne die werklike bedryfsraamwerk van die oond te val. Die modellering van die elektriese smeltoond is bevorder hoewel verdere validasie streng aanbeveel word.

# ACKNOWLEDGEMENTS

---

My greatest thanks go to the Heavenly Father for giving me a world of opportunity and under Whose grace this project was undertaken. Thank You for answering so many prayers and for showing me the path when the view was not clear.

Many thanks go to:

Professor Jacques Eksteen for your excellent supervision, support and mentoring during this project. Thank you for providing me with so many opportunities and for introducing me to the part of the world you so well know.

Professor Steven Bradshaw for co-supervising this project. Thank you for having an open door for discussions and for providing very useful suggestions. My gratitude for administering the last year of the project.

Lonmin Platinum, specifically Riaan Bezuidenhout and Burger van Beek, for providing me with the privilege of conducting this project. Thank you for supporting the project both financially and through the devoted interest. My appreciation also for the visit to the smelter, allowing me to see the "real thing" and gather valuable information required for the modelling.

Neil Snyders from Lonmin Platinum (previously Anglo Platinum) for your invaluable modelling advice. Thank you for sharing your findings from your modelling experience and in the process sparing me costly pitfalls.

Jan Hendrik Grobler from the CSIR for your modelling advice regarding the implementation of three-phase current flow coupled with MHD modelling.

Qfinsoft, the agents for FLUENT in South Africa. Thanks to Danie de Kock and especially Stephan Schmitt for your quick and thorough responses to numerous FLUENT queries. Without your support this project would definitely not have been possible.

Greg Georgalli for providing me with some of the best laughs I had this year and for helping me with the Factsage analysis.

My partner in CFD, Schalk Cloete, for sharing your knowledge of FLUENT and ideas. Thank you also for being an excellent travel companion.

The National Research Foundation of South Africa for providing financial support for the final year of the project. The financial contribution from the Ernst and Ethel Eriksen trust is also kindly acknowledged.

Danie Diedericks for keeping my simulations running while I was away. Our early morning discussions will be a great miss.

Family and friends for your precious support and love. It is your constant prayers that carried me through the whole of my Master's.

Johan Bezuidenhout



# CONTENTS

---

<b>CHAPTER 1 INTRODUCTION.....</b>	<b>1</b>
1.1 PROBLEM STATEMENT .....	2
1.2 OBJECTIVES .....	3
1.3 PLAN OF DEVELOPMENT .....	4
1.4 THESIS OVERVIEW .....	5
<b>CHAPTER 2 ELECTRIC SMELTING AND MODELLING - A REVIEW.....</b>	<b>6</b>
2.1 PGM CONTAINING ORES.....	6
2.2 THE METALLURGICAL PROCESS .....	7
2.2.1 Concentrate preparation.....	7
2.2.2 Electric smelting .....	7
2.2.3 Converting .....	9
2.2.4 Refining .....	9
2.3 THE ELECTRIC SMELTING FURNACE .....	9
2.3.1 Electric furnace layout and main components.....	9
2.3.2 Heat transfer and potential distribution from the electrodes .....	11
2.4 FURNACE OPERATING CONDITIONS AND THEIR EFFECT .....	13
2.4.1 Furnace reactions .....	13
2.4.2 Electrode immersion .....	14
2.4.3 Slag and matte depth.....	14
2.4.4 Slag physical properties.....	15
2.4.5 Variability in concentrate feed.....	16
2.4.6 Chromite and magnetite deposits.....	17
2.5 PREVIOUS MODELLING ATTEMPTS.....	18
2.5.1 Model approaches and formulations.....	18
2.5.2 Geometric effects.....	22
2.5.3 Electrical current, power and potential behaviour.....	22
2.5.4 Flow distribution .....	24
2.5.5 Temperature distribution.....	25
<b>CHAPTER 3 COMPUTATIONAL BACKGROUND .....</b>	<b>28</b>
3.1 THE GOVERNING EQUATIONS .....	29
3.2 ELECTRICAL MODELLING .....	30
3.2.1 Electro-magnetic modelling requirement.....	30
3.2.2 Implementing electrical modelling.....	32

3.3 MULTI-PHASE MODELLING .....	33
3.3.1 <i>The volume of fluid (VOF) multi-phase model</i> .....	34
3.3.2 <i>The discrete phase model (DPM)</i> .....	35
3.4 COMPUTATIONAL SOLUTION .....	36
<b>CHAPTER 4 METHODOLOGY .....</b>	<b>39</b>
4.1 MODEL DEVELOPMENT.....	39
4.1.1 <i>Deciding on a model geometry</i> .....	39
4.1.2 <i>Deciding on the extent of modelling</i> .....	40
4.1.3 <i>Steps towards creating the complete furnace model</i> .....	40
4.2 CREATING THE SOLUTION DOMAIN .....	42
4.2.1 <i>Geometry</i> .....	42
4.2.2 <i>Assigning zones and boundary conditions</i> .....	45
4.2.3 <i>Creating the grid</i> .....	46
4.3 MODEL SPECIFICATIONS .....	49
4.3.1 <i>Physical properties</i> .....	49
4.3.2 <i>Boundary conditions</i> .....	51
4.3.3 <i>Operating conditions</i> .....	51
4.3.4 <i>Energy sinks</i> .....	51
4.3.5 <i>Power inputs</i> .....	55
4.3.6 <i>Multiphase settings</i> .....	56
4.3.7 <i>Magneto-hydrodynamic settings</i> .....	59
4.3.8 <i>Solver settings</i> .....	59
4.4 MODEL ASSUMPTIONS .....	60
4.4.1 <i>Reducing the current frequency</i> .....	60
4.4.2 <i>Neglecting slag and matte tapping</i> .....	61
4.4.3 <i>Constant matte and slag conductivity</i> .....	63
4.4.4 <i>Neglecting furnace freeboard and roof</i> .....	63
4.4.5 <i>Assigning smelting zones</i> .....	64
4.4.6 <i>Neglecting radiation effects</i> .....	64
4.4.7 <i>Neglecting turbulence effects</i> .....	64
4.4.8 <i>Point-force representation of particles</i> .....	65
4.4.9 <i>Additional neglected heat-losses</i> .....	66
4.4.10 <i>Approximation to the furnace refractory</i> .....	66
4.5 PROCESSING SYSTEM SPECIFICATIONS.....	66
4.6 MONITORING SOLUTION CONVERGENCE .....	68
<b>CHAPTER 5 RESULTS AND DISCUSSION .....</b>	<b>70</b>
5.1 CURRENT DENSITY DISTRIBUTION .....	70

5.1.1	<i>Current flow path</i>	70
5.1.2	<i>The mode of current flow</i>	72
5.1.3	<i>The effect of electrode immersions on current flow</i>	73
5.1.4	<i>The effect of electrode immersion on the required slag electrical conductivity</i>	76
5.2	ELECTRIC POTENTIAL DISTRIBUTION	77
5.3	ENERGY BALANCE AND POWER DISTRIBUTION	79
5.3.1	<i>Effect of slag electrical conductivity on heat generation</i>	80
5.3.2	<i>Heat distribution within the melt</i>	81
5.3.3	<i>Effect of electrode immersion on the heat distribution</i>	82
5.3.4	<i>Surface heat flux</i>	83
5.4	TEMPERATURE DISTRIBUTION	85
5.4.1	<i>Characteristics of temperature distribution within the slag layer</i>	85
5.4.2	<i>The temperature within the intermediate and matte layers</i>	86
5.4.3	<i>Model predictions compared to actual operation</i>	87
5.4.4	<i>Model comparison with previous studies</i>	89
5.5	VELOCITY DISTRIBUTION	91
5.5.1	<i>Flow within the slag layer</i>	91
5.5.2	<i>Flow within the matte layer</i>	93
5.5.3	<i>The slag-matte interface</i>	93
5.5.4	<i>Flow within the bath in the absence of CO-bubble induced motion and a high viscosity intermediate layer</i>	93
5.5.5	<i>Importance of bubble induced flow</i>	96
5.5.6	<i>The effect of including turbulence modelling</i>	99
5.5.7	<i>Flow comparison between models</i>	100
<b>CHAPTER 6</b>	<b>CONCLUSIONS</b>	<b>102</b>
6.1	ELECTRICAL CURRENT	102
6.2	ELECTRIC POTENTIAL	103
6.3	ENERGY BALANCE AND POWER DISTRIBUTION	103
6.4	FLUID FLOW	103
6.5	TEMPERATURE	104
6.6	GENERAL	105
<b>CHAPTER 7</b>	<b>RECOMMENDATIONS</b>	<b>106</b>
<b>CHAPTER 8</b>	<b>REFERENCES</b>	<b>108</b>
<b>APPENDIX A</b>	<b>ESTIMATION OF PROCESS MATERIAL PROPERTIES</b>	<b>114</b>
A.1	SLAG LAYER THERMOPHYSICAL PROPERTIES	114
A.1.1	<i>Density [kg.m<sup>-3</sup>]:</i>	114
A.1.2	<i>Viscosity [kg.m<sup>-1</sup>.s<sup>-1</sup>]:</i>	116

A.1.3 Specific Heat Capacity [ $J.kg^{-1}.K^{-1}$ ]: .....	117
A.1.4 Thermal Conductivity [ $W.m^{-1}.K^{-1}$ ]: .....	118
A.1.5 Electrical Conductivity [ $mho.m^{-1}$ ]: .....	119
A.2 MATTE LAYER THERMOPHYSICAL PROPERTIES .....	121
A.2.1 Density [ $kg.m^{-3}$ ]: .....	121
A.2.2 Viscosity [ $kg.m^{-1}.s^{-1}$ ]: .....	122
A.2.3 Specific Heat Capacity [ $J.kg^{-1}.K^{-1}$ ]: .....	123
A.2.4 Thermal Conductivity [ $W.m^{-1}.K^{-1}$ ]: .....	124
A.2.5 Electrical Conductivity [ $mho.m^{-1}$ ]: .....	124
A.3 CONCENTRATE LAYER PHYSICAL PROPERTIES .....	124
A.3.1 Density [ $kg.m^{-3}$ ]: .....	124
A.3.2 Specific Heat Capacity [ $J.kg^{-1}.K^{-1}$ ]: .....	124
A.3.3 Thermal Conductivity [ $W.m^{-1}.K^{-1}$ ]: .....	125
A.3.4 Electrical Conductivity [ $mho.m^{-1}$ ]: .....	125
A.4 SLAG-MATTE SURFACE TENSION ESTIMATION .....	125
A.5 REFERENCES .....	126
<b>APPENDIX B SUPPORTING CALCULATIONS .....</b>	<b>128</b>
B.1 COMPARISON BETWEEN BUOYANCY AND LORENTZ FORCES .....	128
B.1.1 Buoyancy driven flow: .....	128
B.1.2 Lorentz-Force driven flow: .....	129
B.1.3 Buoyancy-Lorentz force driven flow transition criteria: .....	130
B.2 FLOW CRITERIA WITHIN THE SLAG BATH .....	131
<b>APPENDIX C USER DEFINED FUNCTIONS (UDF'S) .....</b>	<b>132</b>
C.1 CURRENT INPUT .....	132
C.2 SLAG ENERGY SINK .....	132
C.3 CONCENTRATE ENERGY SINK .....	133
C.4 ENERGY SINK FOR THE ELECTRODES .....	134
<b>APPENDIX D RESIDUAL MONITORING .....</b>	<b>135</b>

# LIST OF SYMBOLS

SYMBOL	DESCRIPTION	UNITS
$A$	Area	$m^2$
$b$	Induced magnetic field	Tesla
$B$	Magnetic field	Tesla
$C_D$	Drag coefficient	
$C_p$	Heat capacity at constant pressure	J/kg.K
$D_H$	Hydraulic diameter	m
$d$	Diameter	m
$d_p$	Particle diameter	m
$E$	Total energy/ activation energy	J, kJ
$f$	Body forces	N
$F$	Lorentz force	N
Gr	Grashoff number	
g	Gravitational acceleration	$m/s^2$
$H$	Total enthalpy	energy/mass
$h$	Heat transfer coefficient	$W/m^2.K$
$h$	Specific enthalpy	J/kg
$J$	Current density	$A/m^2$
$k$	Kinetic energy per unit mass	J/kg
$k$	Thermal conductivity	$W/m.K$
$l$	Length	m
$L$	Length	m
$L_T$	Axial length scale	m
$m$	Mass	g,kg
$\dot{m}$	Mass flow rate	kg/s
$M_w$	Molecular weight	g/mol
Nu	Nusselt number	
$p$	Pressure	Pa
Pe	Peclet number	
Pr	Prandtl number	
$Q$	Energy flow rate	W
$q$	Heat flux	$W/m^2$
$r$	Radius	m

Re	Reynolds number	
Ra	Raleigh number	
$R_j$	Reaction source term for species /	
$T$	Absolute temperature	K
$T_{or} T_M$	Reference temperature	K
$t$	Time	s
$R$	Radius	m
$S_\phi$	Source term	
$S_h$	Volumetric rate of heat generation	
$u$	x-direction velocity	m/s
$u_p$	Particle velocity	
$u_b$	Boundary velocity	m/s
$U$	Free-stream velocity	m/s
$v$	y-direction velocity	m/s
$V$	Volume	m <sup>3</sup>
$\vec{v}$	Overall velocity vector	m/s
$w$	z-direction velocity	m/s
$X$	Mole fraction	
$Y$	Mass fraction	
$\alpha$	Thermal diffusivity	m <sup>2</sup> /s
$\alpha$	Volume fraction	
$\sigma$	Electrical conductivity	mho/m
$\beta$	Coefficient of thermal expansion	K <sup>-1</sup>
$\Delta$	Change in variable	
$\varphi$	Electric potential	V
$\phi$	Denoting any particular dependant variable	
$\kappa$	Electrical conductivity	mho/m, mho/cm
$\mu$	Dynamic viscosity	Pa.s
$\mu_m$	Magnetic permeability	H/m
$\nu$	Kinematic viscosity	m <sup>2</sup> /s
$\rho$	Density	kg/m <sup>3</sup>
$\tau$	Shear stress	Pa

## SUBSCRIPTS

---

<i>ave</i>	Average
<i>matte</i>	Referring to variables or properties assigned to the matte phase
<i>m</i>	Referring to a magnetic property
<i>slag</i>	Referring to variables or properties assigned to the slag phase
<i>wall</i>	Referring to variables or conditions at the boundary wall
<i>x,y,z</i>	Directional indications

## ABBREVIATIONS

---

CFD	Computational Fluid Dynamics
CICSAM	Comprehensive Interface Capturing Scheme for Arbitrary Meshes
DPM	Discrete Phase Model
D-P-S	Discrete Phase Sources
Gambit	Geometry and Mesh Building Intelligent Toolkit
PISO	Pressure-Implicit with Splitting of Operators
PRESTO!	PREssure Staggering Option
P-V-C	Pressure Velocity Coupling
SIMPLE	Semi-Implicit Method for Pressure-Linked Equations
UDS	Upwind Differencing Scheme
VOF	Volume of Fluid
1 <sup>st</sup> O-U	First Order Upwind

## MATHEMATICAL CONVENTIONS

---

The operator,  $\nabla$ , known as grad or del represents the maximum gradient vector at a point in the field, whose components' magnitude are made up of partial derivatives, presented below for a Cartesian coordinate system.

$$\nabla = \frac{\partial}{\partial x} \vec{i} + \frac{\partial}{\partial y} \vec{j} + \frac{\partial}{\partial z} \vec{k}$$

---

# CHAPTER 1

## INTRODUCTION

---

The development of the South African platinum industry has taken a giant leap from the first mining explorations in 1920 to where it is today. The platinum group metals (PGM) were initially recovered by traditional milling and gravity table concentration methods but were soon replaced by flotation concentration in 1926. The fast expansion of the platinum industry led to matte-smelting being adapted for platinum recovery even though it was mainly used for extracting gold, silver, copper, nickel and cobalt at the time. The first of multiple blast furnaces was built in 1936 for this purpose but the process was considered inefficient due to the high expense of coke and labour and the large volumes of process off-gas being a pollution problem. Reverberatory smelting, used for copper smelting, was never used for platinum recovery due the considerably higher, 100-200°C, liquidus temperature of the slag resulting from platinum ores. It was not until 1969 that the novel technology of electric smelting was applied in the construction of the 19.5MVA Elkem electric furnace with 6 in-line submerged electrodes. Electric smelting offered an efficient and profitable advantage over fuel driven processes by providing a direct application of energy [Jones 1999 and 2005].

At present, South Africa is the world's primary platinum producer, leading international production by 80% and having 88% of recoverable resources entrapped in the reefs of Merensky, UG2 and the Platreef of the Bushveld complex. However, current platinum supply falls far short of meeting the escalating demand. According to current statistics, the supply deficit will reach 265 000 ounces this year, amounting to seven years for which the market has seen a shortfall [Hopkins 2008]. With the platinum price having tripled in the past five years, platinum has become a very attractive investment opportunity. Demand is expected to increase steadily and therefore placing high pressure on the platinum suppliers.

To increase global supply, the platinum producer Lonmin Platinum acquired a 28MW AC circular electric smelting furnace in 2002, the largest of its kind used for the purpose of PGM recovery [Jones



1999]. This furnace was designed to process a blend of Merensky and UG2 ore, providing for a foreseen depletion of the Merensky reserve. However, the smelting of higher UG2 ratios, being a higher chromite bearing concentrate, created problems in the form of chromite-spinel precipitation within the furnace, causing process disruption and reduction in furnace capacity. This resulted in the furnace operating at higher temperatures in the hope of improving chromite-spinel solubility.

## **1.1 Problem statement**

---

The electric smelting furnace is best described as a complex system. The extensive heat generated through resistive heating promotes the separation of a gangue-rich slag layer and a precious metal-rich matte layer based on the principle of density differences. The furnace therefore hosts a multidimensional, multi-phase system where flow is induced by gas-bubbles from the electrode tips, buoyancy and slight magnetic influence. Each material layer contained within the furnace walls possesses a character expressed by a unique set of non-linear properties that describe its interaction with the heat and current gradients brought forth by the electrodes.

This dynamic system is susceptible to a large number of influences of which the material layer depth, feed composition and electrode immersions are the main control parameters that are continuously adjusted by a sophisticated control system to maintain optimum operation. It is evident that a comprehensive knowledge of the furnace behaviour is required to expand and improve the current operation and throughput. The extreme process conditions do not permit uncomplicated evaluation of the furnace interior and one is left with only external parameters to mirror the behaviour on the inside.

Commercial Computational Fluid Dynamics (CFD) was initially developed for mechanical applications but has fairly recently found its way to the modelling of processes in the metallurgical engineering industry. CFD can be viewed as a powerful engineering toolkit for creating virtual computer prototypes of processes that would under the actual operating conditions be impossible to predict and quantify. A CFD model that could resemble the electric smelting furnace as closely as possible is therefore regarded as an invaluable asset for describing the interior dynamics that could lead to potential optimization of the present unit.

Previous CFD models on the electric furnace of various complexities have been attempted but still fall short of providing a complete and accurate model representation. Several phenomena such as multiphase layers, gas dispersion, smelting of material and the dynamic AC electrical power supply are yet to be addressed.

## 1.2 Objectives

---

*"Although the power and capabilities of CFD are continually rising, the first-order complexities of the electric furnace bath (e.g. buoyancy-driven multi-phase fluid flow coupled with melting/smelting and solidification, transitional boundary layers, gas evolution, and highly non-linear property variations) still make it difficult to obtain even a single trustworthy solution."*

(Utigard 2000)

It is believed that by taking advantage of the most recent advances in commercial CFD coupled with Magnetohydrodynamic (MHD) modelling software the modelling of the Lonmin electric smelting furnace can be forwarded towards an ideal and holistic representation. A modern approach to modelling will improve the understanding of the furnace dynamics by acquiring insight into:

- the impact of the furnace multi-phase character on the dynamics hosted by the melt. Of particular interest will be the influence on flow and heat transfer distribution within the molten bath.
- the electrical current distribution from the electrodes. The modelling of current flow will allow characterization of the mode and estimation of the quantity of current flow between electrodes and by way of the matte layer.
- the electric potential gradients corresponding to current flow within the melt with which to identify regions under possible magneto-hydrodynamic strain, especially in the matte layer.
- the location and amount of power generation within the melt that will assist in establishing a furnace energy balance and so create an idea of the power dissipation in the different material layers.
- the temperature distribution within the material layers developing in furnace and the identification of hot-spots and potential areas where accretions are likely to be found.
- the flow dispersion and the extent of mixing that are likely to result due to buoyancy forces acting on the molten material and CO-gas bubbles forming at the immersed electrode tips due to combustion of the carbon electrodes.

- the effect of electrode immersion on the furnace dynamics as portrayed by the current and power distributions.

A personal objective is to create appreciation for the potential of CFD as a novel approach to Engineering, especially in the metallurgical industry.

## **1.3 Plan of development**

---

In order to meet the project objectives, a furnace model representing the actual furnace system as closely as possible has to be created. For this to be achieved, the following has to be performed:

- Due to a lack of experience and knowledge prior to modelling, an understanding of the furnace operation has to be acquired. The characteristics of the furnace have to be identified in order to determine the modelling scope and devise a modelling strategy.
- A representative CAD furnace geometry has to be created based on the actual furnace dimensions and effectively converted into a computational domain that can successfully be compiled by the CFD software.
- Physical properties, which are most likely temperature dependant, have to be obtained for the material layers present in the furnace as well as the furnace refractory.
- Descriptive conditions have to be assigned to the computational domain which must also be subjected to the proper mathematical models so as to ensure a physical viable model.
- Approximations have to be developed for incorporating the physical phenomena present in the furnace system that falls outside the bounds of the current CFD software and computational processing capabilities.
- The model must be allowed to generate justified numerical results that have to be processed and interpreted in order to formulate a discussion and draw conclusions. Possible validation of the results will strengthen confidence in the model outcome.

## 1.4 Thesis overview

---

The main body of the thesis is presented in four chapters that form the backbone in the development of a model for the electric smelting furnace. A brief outline of these chapters is provided:

### **Chapter 2**

A review of the process and mechanisms involved in electric smelting is presented along with a survey of previous modelling attempts found in open literature.

### **Chapter 3**

A background on the mathematical modelling incorporated in CFD as used to describe the furnace model.

### **Chapter 4**

A step by step discussion on the reasoning and method followed in developing the model.

### **Chapter 5**

The outcomes of the furnace model are grouped according to the electrical thermal and flow behaviour predicted by the model that are interpreted and discussed in this chapter.

The references are found in the last chapter, followed by an extensive Appendix for supporting the claims made in the thesis main body.

---

# CHAPTER 2

## **ELECTRIC SMELTING AND MODELLING - A REVIEW**

---

It was mentioned that the dynamic behaviour of the electric smelting furnace is determined by an interacting set of parameters that could range from micro-scale effects such as internal transport phenomena to those of more prominent effects such as electrode immersion or material layer depth. In order to obtain a background understanding prior to modelling, a review considering the electric smelting furnace and its influences was conducted. The investigation into electric smelting included consideration of the mechanism of smelting, smelting dynamics and operating conditions that will require thought during modelling. To serve as a basis for the current study, previous modelling attempts regarding the topic of electric smelting were assessed and discussed.

### **2.1 PGM containing ores**

---

The Platinum Group Metals (PGM's) are most commonly deposited with copper-nickel sulphides, contained in magmatic rocks. The UG2 reef lies 20 to 330m underneath the Merensky reef but possesses its own distinct mineralogy. The minerals contained in Merensky ore are embedded in a silicate matrix that holds a higher sulphide content compared to UG2 ore, which has its minerals embedded in the chromite matrix [Jones, 2005]. The latter is the reason for operating the smelting furnace at elevated conditions compared to smelting pure Merensky ore in the hope of reducing the formation of chromite spinel, as will be discussed later.

It can be seen from Table 2.1.1 below that the PGM content of UG2 ore is valuably higher than the Merensky ore, however it contains significantly less base metal sulphides (6-7%) compared to Merensky ore (17-18%). The major difference between UG2 and Merensky ore is considered

to be the concentrations of pyroxene,  $(\text{Mg,Fe})\text{SiO}_3$ , which is the main source for introducing FeO, base metal and chromite to the system [Eksteen, 2007].

*Table 2.1.1 Concentrate compositions for the major PGM containing reefs mined by Lonmin (all given as percentage except the PGM concentration which is given as g/t) [Jones, 1999].*

Ore type	Al <sub>2</sub> O <sub>3</sub>	CaO	Co	Cr <sub>2</sub> O <sub>3</sub>	Cu	FeO	MgO	Ni	S	SiO <sub>2</sub>	PGM
Merensky	1.8	2.8	0.08	0.4	2.0	23	18	3.0	9	41	130
UG2	3.6	2.7	0.06	2.8	1.2	15	21	2.1	4.1	47	340

## 2.2 The metallurgical process

---

PGM containing ore is processed with the extraction of PGM's as primary objective and that of base metals as secondary objective. Different approaches to the metallurgical process are adopted by the various platinum producers and include different designs for electric smelting. However, it is the process surrounding the three-electrode circular Lonmin furnace that will be discussed briefly.

### 2.2.1 Concentrate preparation

Concentrates from various origins are blended in specific proportion before being pneumatically fed to the electric smelting furnace. In an attempt to reduce the energy requirement for smelting, the concentrate is dried by means of a flash drier prior to entering the furnace. This step also reduces the occurrence of "blowbacks" in the furnace due to decomposing water molecules resulting from fast evaporation [Jones, 2005; Tseidler, 1964].

### 2.2.2 Electric smelting

Concentrate is fed into the circular furnace by an automated control system that matches the feed-rate to the power input and energy losses [Jones, 2004]. Also fed through specific locations in the furnace roof are limestone (used as flux) and reverts (tap spillings and converter overflows). Electrical energy is converted to resistive heating and is supplied to the furnace bath by means of three graphite electrodes penetrating through the furnace roof into the material layers.

During the smelting process, the components of the charge separate into two or more layers of which the most prominent are: the slag layer, consisting mostly of molten oxides and silicates (gangue), and a Ni-Cu-Fe-S matte layer, containing a solution of the valuable metallic sulphides. As mentioned, the technique of matte-slag separation relies on difference in density between the two layers, with the matte layer being denser (typical SG of 5 compared to the slag layer with an SG of 3) [Jones 2004]. A solid layer of concentrate, referred to as “black top” operation, is maintained on top of the slag layer for limiting radiation heat transfer from the bath to the furnace roof and walls [Jones 1999].

Droplets of molten matte form within the slag layer and become larger by coalescing with other droplets and settle out to form the matte layer on the hearth of the furnace. The segregation of matte prills is very dependant on the slag viscosity. For this reason limestone is introduced to serve as a flux for reducing the slag viscosity and liquidus temperature.

The matte and slag depths are manually determined by using a sounding bar that is pushed into the material layers. The slag and matte layers are tapped separately from the furnace: the matte phase periodically, depending on the requirement, and the slag almost continuously [Jones 2005]. The slag layer within the furnace has a dual function in providing means of discharging iron and gangue from the system and to function as the main resistance for heat generation, the mechanism of which will be discussed in *Chapter 2.3*.

*Table 2.2.1 Lonmin matte analysis (given as percentages except the PGM account is given as g/t) [Jones 1999].*

Ore type	Co	Cr	Cu	Fe	Ni	S	PGM
Merensky	0.5	0.23	9.7	37	17	28	1000
UG2	0.5	0.29	9.8	35	17	28	2500

*Table 2.2.2 Lonmin slag analysis (given as percentages) [Jones 1999].*

Ore type	Al <sub>2</sub> O <sub>3</sub>	CaO	Co	Cr <sub>2</sub> O <sub>3</sub>	Cu	FeO	MgO	Ni	SiO <sub>2</sub>
Merensky	2.0	9.8	0.05	1.2	0.09	28	19	0.15	44
UG2	3.9	13	0.02	2.4	0.13	9.2	22	0.11	47

The tables above provide typical analyses for the matte and slag layers for electric smelting done by the Lonmin smelters. The matte is rich in iron, nickel, copper, cobalt,

sulphur and the PGM's, which have little tendency to dissolve in the slag phase. The matte is tapped into ladles and transferred to the Pierce-Smith converter whereas the slag is granulated and transported to the slag plant for further recovery of the valuable metals. The furnace off-gas passes through an afterburner so to oxidize the large volumes of CO gas before being cleaned by an electrostatic precipitator and processed by the SO<sub>2</sub> plant.

### **2.2.3 Converting**

Molten matte is transported to the Pierce-Smith converters where it is blown with oxygen-enriched air with the objective of converting the remaining iron sulphide to oxide and potentially removing all the iron as slag, leaving a nickel-rich matte containing the PGM's [Betteridge 1984]. In order to flux the iron oxide, silica sand is added to the converter contents to form an iron silica slag that is skimmed off, granulated and conveyed to the slag plant. The converter matte mostly consists of Ni<sub>3</sub>S<sub>2</sub>, FeS Cu<sub>2</sub>S and the PGM's that is poured into ladles and transferred to the Leaching plant [Jones 2005].

### **2.2.4 Refining**

The converter matte is milled before being subjected to a sulphuric acid leaching process to extract the copper and nickel, which are further processed by the Base-Metal Refinery. The PGM's are concentrated in the leach residue which is transferred to the Precious Metal Refinery where 99.99% pure platinum is produced [Jones 2005, Cramer 2001].

## **2.3 The electric smelting furnace**

---

The modelling of the electric furnace requires knowledge of the electric furnace design along with the mechanism of heat transfer from the electrodes to the molten bath. These concepts are described below.

### **2.3.1 Electric furnace layout and main components**

#### The electrodes

Three Soderberg-type electrodes are used where carbon paste is self-baked into 1.4m diameter electrodes protruding into the furnace bath. The high conductivity of carbon makes it ideal to use as electrode material, allowing current to pass through without internal heat generation while simultaneously acting as reducing agent. The electrodes are consumed within the furnace bath over a period of time, the consumption rate being



a function of the reaction within the slag that varies with the depth of immersion. The electrodes are semi-automatically slipped into the molten contents depending on the power requirement [Robiette 1973, Schreiter 2006].

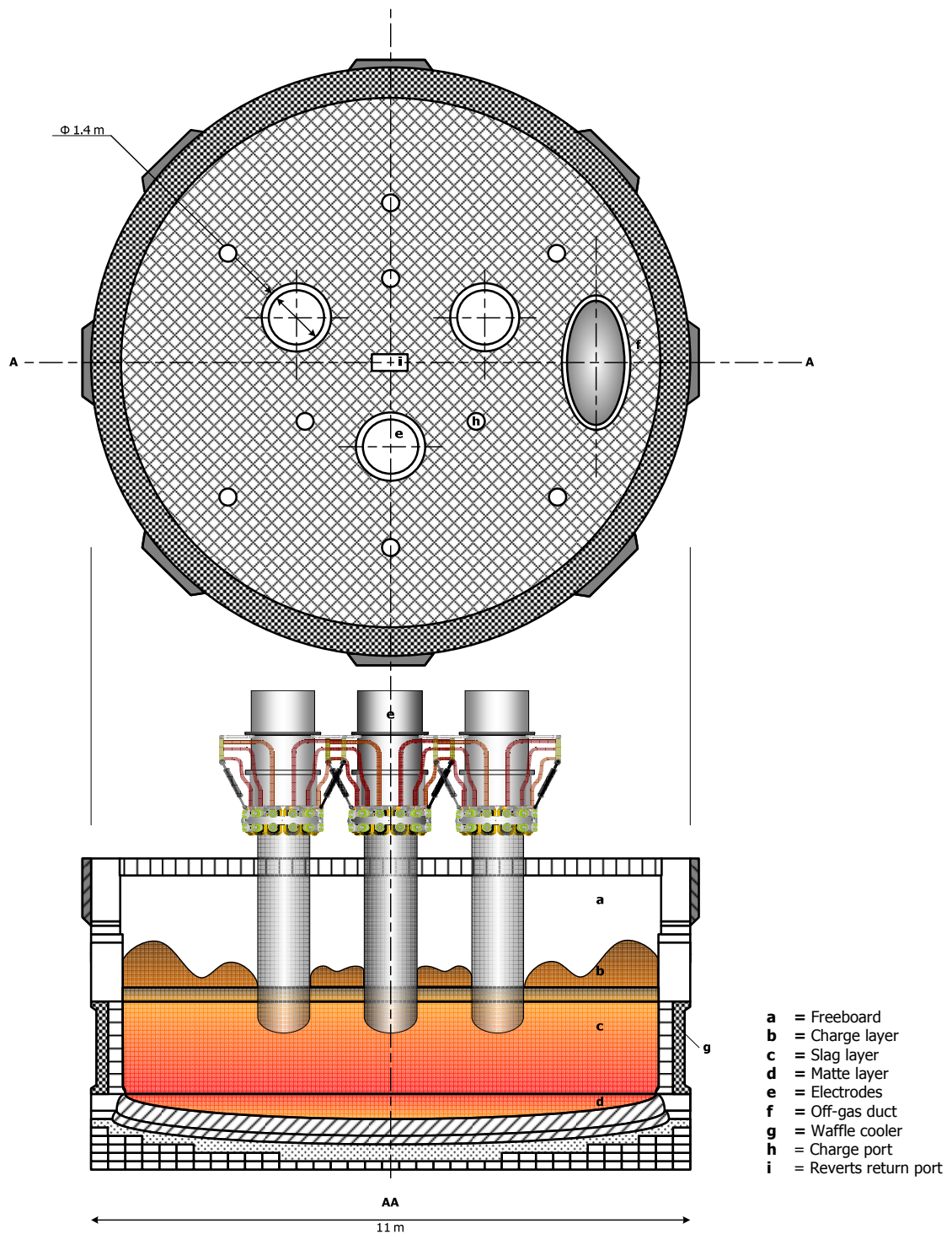


Figure 2.3.1 Schematic of the three-electrode electric smelting furnace.

The three electrodes of the furnace can be arranged in delta or star configuration but are predominantly operated as a delta connection since a broader range of operating conditions can be achieved, e.g. higher reachable furnace power. Current is supplied to

each electrode by means of contact clamps mounted around the electrode surface before entry through the furnace roof.

#### The furnace shell and cooling systems

The furnace shell consists of numerous refractory linings to allow efficient insulation of the molten contents and prevent heat losses to the surroundings. To protect the furnace refractory against the fierce reactions and extreme temperatures, a freeze lining (a layer of solidified material) is maintained along the uppermost wall of the furnace interior. This is made possible by a specially designed side cooling system. The bottom of the furnace, if necessary, is cooled by forced air ventilation. The furnace is a closed-type furnace, with a roof allowing penetration by the electrodes, charging pipes and the off-gas duct [Schreiter 2006].

#### The material layers

Furnace charge is fed through various ducts with the largest portion being deposited in the hottest area within the furnace, i.e. between the electrodes. A charge layer of thickness no greater than the electrode immersion depth in the slag is considered good practice [Tseidler 1964]. The charge layer settles to become molten, forming the underlying slag layer, while matte droplets diffuse through the slag layer and settle on the furnace hearth to form the matte layer as previously mentioned. Intermediate layers of material precipitate are also likely to form, causing operational difficulties which will be discussed later.

#### Tap holes and off-gas discharge

Tap holes are situated at opposite ends of the furnace to allow tapping by means of a drilling machine. The off-gas vent is situated in the side of the furnace roof ensuring a slight negative pressure to be maintained within.

### **2.3.2 Heat transfer and potential distribution from the electrodes**

Within the electric smelting circuit, the resistances of the electrodes and furnace refractory are negligible compared to the resistance formed by the furnace charge and slag layer. As the charge descends and becomes molten, the electrical resistance is significantly lowered and a conductive path is created for current flow between the electrodes [Robiette 1973]. The electrical resistance of the slag layer is significantly higher than that of the matte layer, which is a fairly good conductor. Thus the resistivity of the slag layer is the major source of heat generation (also called Joule heating) within the furnace.

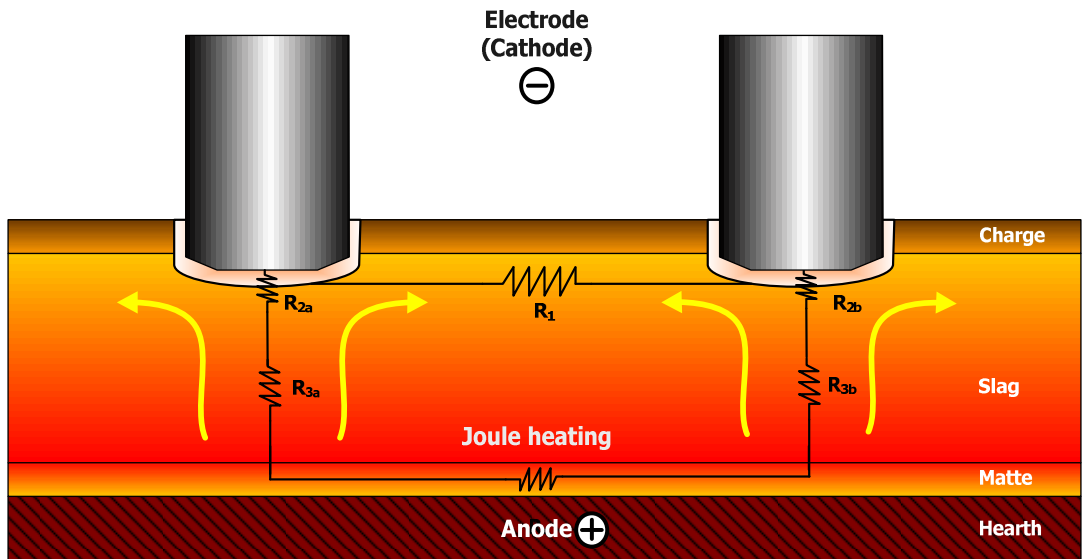


Figure 2.3.2 Schematic representation of the submerged arc mode of heat transfer and resistances occurring within the molten bath.



Figures 2.3.3 Photos of the furnace interior (a) Immersed electrode (b) Electrodes slightly raised.

The reduction taking place at the submerged electrode surface results in the formation of CO-gas bubbles that, in turn, form a gas-layer that covers the surface of the immersed electrode [Tseidler 1964]. Under moderate conditions the gas would exert an insulating effect; however the extreme temperatures and applied electric field make it reasonable for the breakdown potential of the gas to be reached. This implies ionization of the neutral gas molecules that create a significant drop in potential with further increase in current. Under the current operating conditions this is likely to concentrate conduction

into a narrow channel to form numerous micro-arcs at the surface of the electrode cathode [Llewellyn-Jones 1996, Tseidler 1964].

The localized voltage drop results in a large heat release in the narrow vicinity around the electrode, approximated as one third of the total heat output of the furnace [Tseidler 1964]. The heat released will therefore not only depend on the resistivity of the slag but of the micro-arcs as well. It is reported [Tseidler 1964] that up to 80% of the over-all voltage loss could occur at low depth electrode immersions but under sufficient immersion (approximately 800mm) the potential drop could be 35-40%. The phenomenon of arcing is also elucidated through the study by Sheng *et al.* (1998) who eliminated electrical conductivity, temperature and the Fe/SiO<sub>2</sub> ratio of the slag as probable causes for the observed potential drop at the electrode surface of a large-scale industrial furnace and resided in arcing as the most plausible cause.

The superheated slag at the electrode tip is moved up and around the electrode towards the furnace walls due to buoyancy momentum created primarily by the forming gas-bubbles and natural convective forces. Heat is transferred to the matte and floating charge layer by convection and conduction [Matyas *et al.* 1992]. It is therefore required that the slag layer be maintained at a higher temperature than the matte, which could mean a matte tapping temperature 160°C below the slag liquidus temperature. A very steep temperature gradient is therefore expected within the slag layer due to the thermal conductivity of the matte layer being more than 10 times higher [Utigard *et al.* 1976].

## **2.4 Furnace operating conditions and their effect**

---

The economy of the electric smelting furnace is supported by its method of operation. Its ability to handle variability in the concentrate feed, process instabilities and temperature variations, especially during tapping times, relies on competent control for the best trade-off among the furnace variables. The conditions that affect furnace operation were identified and discussed in the hope of acquiring a much-needed understanding for model representation and evaluation of the modelling outcome.

### **2.4.1 Furnace reactions**

The kinetics and sequence of the smelting reactions occurring within the furnace are temperature dependent. These reactions, mainly endothermic, are specific in their occurrence, varying during the different stages of furnace operation and at different

locations within the furnace - depending on the temperature profile throughout the furnace.

Celmer *et al.* (1986) identified two temperature ranges, i.e. a low temperature range in which only solid and gas–solid reactions are presumed to form and a high temperature range where reactions between gas, liquid and solid are likely to occur. The high temperature reactions are responsible for the formation of the iron-, metallic sulphide-rich matte layer. These reactions occur mainly by oxide reduction by carbon from the electrodes and additional coke to serve as reducing agent. The slag layer is considered to form mainly as a result of the reaction between iron-sulphide and silica [Mabiza 2006]:  $2\text{FeO} + \text{SiO}_2 = 2\text{FeO}.\text{SiO}_2$ . Further discussion on the reactions occurring within the electric smelting furnace is presented in the study by Celmer *et al.* (1986).

#### **2.4.2 Electrode immersion**

The overall electrical resistance within the slag is increased when the electrode immersion is decreased [Sheng *et al.* 1998]. Slight electrode immersion is responsible for high slag resistances and accompanying higher current densities that result in the rounding of the electrode tips [Sheng *et al.* 1998]. Increased electrode immersion will cause higher conversion of energy into heat between the electrodes and matte. A very deep electrode penetration will cause a high current flux ( $\text{A}/\text{m}^2$ ) in the matte, leading to overheating and high turbulence within the matte layer [Barth 1960, Eksteen 2007]. Appropriate immersion into the slag will generate sufficient heat at the slag surface, providing high temperature where melting is required [Barth 1960]. However, the larger the electrode area exposed to the material and therefore the electrode immersion, the smaller the effect of micro-arc resistance and the accompanying loss of furnace power [Tseidler 1964].

As stated by Barth (1960) and experimentally demonstrated in the study by Urquhart *et al.* (1976), approximately a quarter to a third of the total current passes between the electrodes and two third to three quarters between the electrode tip and the low-resistivity matte layer. The fraction of the current passing directly towards the matte is considerably lowered when the immersion depth is reduced, therefore allowing the bulk slag to be more effectively heated [Urquhart 1976].

#### **2.4.3 Slag and matte depth**

Control of the slag layer thickness is of high importance in the management of the furnace as it is the primary mode of heat generation and way of discarding iron and

gangue. A thin slag layer would cause the electrodes to be positioned too close to the matte layer. The bulk of the current will pass via the matte layer, leading to possible overheating of the hearth.

A thick slag layer allows deeper immersion of the electrodes, reduction in micro-arc resistance and therefore higher energy release within the bath [Tseidler 1964]. However, an excessively thick slag layer will permit precipitation of the high-melting components in the lower, cooler, layers of the slag. The matte layer will also be inadequately heated since the bulk of the current will flow through the slag while tapping of both slag and matte will be hampered due to the heavy hydraulic pressure resting on the tap-holes [Tseidler 1964, Barth 1960].

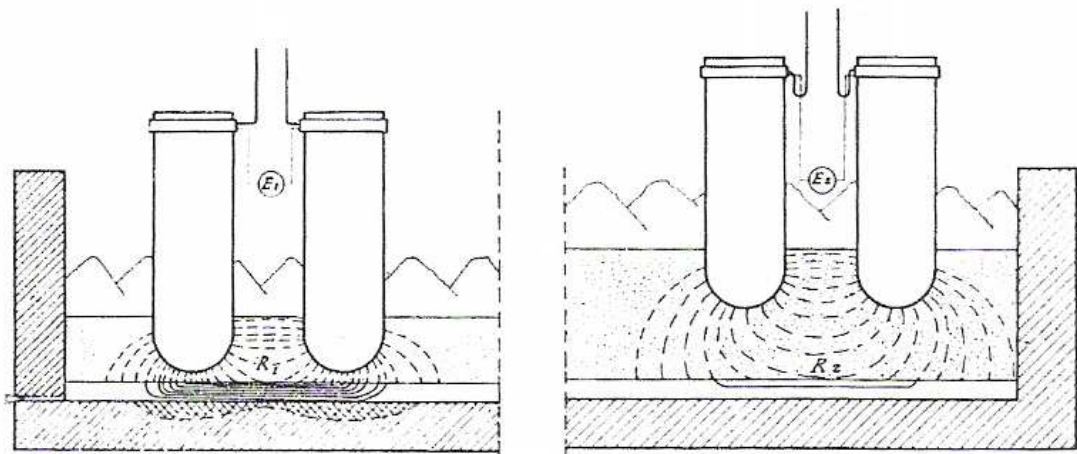


Figure 2.4.3.1 Current paths within the melt as presented in Barth (1960).

#### 2.4.4 Slag physical properties

The formation of a slag layer having suitable chemical and physical properties for optimum furnace operation predicates a successful smelting operation [Neill 2004]. The effect of the slag physical properties on the system is briefly addressed for background knowledge when the model properties are specified.

##### Viscosity and density

The slag should have a low viscosity to allow adequate separation and settling of molten metal droplets towards the matte phase. The viscosity of the slag is temperature dependent and will therefore vary according to the heat distribution throughout the furnace [Eric 2004]. The viscosity and the slag conductivity are oppositely related since an increase in the slag conductivity and hence a decrease the slag resistivity will result in a decreasing viscosity [Eric and Hejja 1995]. The slag and matte densities are also

temperature dependent, which would induce stirring effects as a result of natural convection forces.

#### Conductivity (reciprocal of resistivity)

As discussed previously, low slag conductivity (compared to a highly conductive matte layer) is desired for a corresponding increase in Joule heating. Sheng *et al.* (1998) observed that an increase in temperature within the furnace will result in an increase in the conductivity of the slag, which will result in more power being drawn into the furnace that will further increase the furnace temperature. This will lead to unstable furnace operation and effectively a diverging computational solution, when modelled.

#### Liquidus temperature

The liquidus temperature should be as low as possible to minimize heat loss by radiation, reduce wear of the furnace refractory lining and to prevent matte superheat [Eric and Hejja 1995, Nell 2004].

#### Base metal solubility and chromium solubility

The slag should have a minimum solubility of nickel, copper and cobalt so that they will report to the matte layer for recovery. The solubility is dependent on the composition, increasing with increasing CaO and MgO concentrations, since these compounds act as substitution for base metal-oxide losses to the slag [Eric 2004]. High chromium solubility in the slag layer is most desirable, helping to minimize the accumulation of chromium spinel and residues to be further discussed.

### **2.4.5 Variability in concentrate feed**

Variability in the concentrate feed composition is not intended for modelling but is closely linked with the physical properties of the material layers and therefore warrant a brief discussion.

The trivalent oxides of Fe and Cr in the concentrate feed have the characteristics of high density, high viscosity and low solubility within silicate slags which is likely to result when smelting higher ratios of UG2 ore [Barnes and Newall 2006]. An increase in FeO concentration also results in a significant increase in the slag conductivity which in turn would require adjustment of the electrode position. Consequently the smelting capacity of the furnace will be reduced and the temperature difference between the slag and matte will become greater. Although they are only in minor difference in CaO concentration between the ore-types, this property has a similar effect on the conductivity as does FeO concentration. Silica, the element matrix of UG2 ore, has opposite effects compared to the

latter [Eksteen 2007]. These oxides also have high melting points and partial solubility in the matte layer [Barnes and Newall 2006].

#### **2.4.6 Chromite and magnetite deposits**

The modelling of the electric furnace will be restricted to a two phase system, i.e. the slag and matte phases - the details of which will be discussed under the modelling methodology. However, the actual furnace hosts additional phases but not as prominent as the slag and matte phases. These phases are in the form of chromite spinels and magnetite deposits that cause cumbersome operation for the electric furnace. Their effect and occurrence in the furnace is briefly discussed.

Fine chromite particles are suspended within the slag layer, as desired, however larger particles settle and become accumulated between the slag and matte layers, creating a problematic intermediate layer or spinel [Barnes and Newall 2006]. The consequent operating problems, as stipulated by Nell (2004), are

- the prevention of pure separation of slag and matte.
- the increase in slag viscosity, therefore preventing the settling of metal droplets.
- the increase in slag liquidus temperature, resulting in the superheating of the matte and possible corrosion of the furnace refractory lining.
- the reduction in furnace capacity and irregular tapping due to the freezing of spinel on the furnace sidewalls and hearth. The hearth profile is also altered.

Various suggestions have been made to reduce the effect of spinel accumulation. One of which is the increase in operating temperature by lowering the electrodes so that the tips are in the vicinity of the spinel layer, hoping to encourage the reduction of  $\text{Cr}_2\text{O}_3$  to  $\text{CrO}$  that will be soluble in the slag. For this reason furnaces treating high UG2 concentrations are operating at  $500^\circ\text{C}$  higher than in the case with chrome-free Merensky ore. This is however, a high-risk operation as previously stated, leading to possible matte overheating and turbulence [Eksteen 2007]. Nell (2004) reports the solubility of  $\text{Cr}_2\text{O}_3$  to be only 0.6% at a  $1500^\circ\text{C}$  operating temperature, making high temperature not worthy as a probable solution.

Similar to the chromite-problem, the incomplete reduction of magnetite ( $\text{Fe}_3\text{O}_4$ ) to  $\text{FeO}$ , results in magnetite accumulation within the matte and slag. Like the chromium spinels, magnetite also accumulates between the slag and matte layers and, being of high viscosity, also restricts the settling of metal droplets towards the matte layer [Gill 1980].



## 2.5 Previous modelling attempts

---

Numerous attempts to model the electric furnace have been made with the level of complexity increasing with the advance in computing power over the years. At present no model available in open literature records a full computational model where all of the furnace influences are addressed. The reviewed literature is focused mostly on modelling the effects in the immediate vicinity of the electrodes or within the slag bath in its entirety. Only few studies have included modelling a combination of the slag and matte layers but with the matte layer as a solid phase.

The available literature was reviewed to create a platform for the present study. The literature was assessed and discussed under the specific topics relevant to the current modelling, i.e. the model formulations and main findings that were grouped according to geometry effects and the distribution of electrical potential, flow and heat.

### 2.5.1 Model approaches and formulations

As stated, the modelling approaches differ in complexity and unique simplifications and boundary conditions were adopted. However a similar approach was observed that include the computational solution of the conservation equations and incorporation of the effects of buoyancy and Joule heating as source terms.

#### Modelling by Urquhart *et al.* (1976)]:

One of the first available modelling attempts by *Urquhart et al.* consisted of temperature, electrical and electrode position measurements coupled with computer based modelling. This modelling was performed through electrical potential measurements on the slag layer of a 19.5MVA six-in line electrical furnace and processed by a mini-computer as to calculate the electrical field, current and power distributions. The results were used to discuss the effect of electrode immersion.

#### Modelling by Jardy *et al.* (1986):

In the modelling by *Jardy et al.* (1986), a computer program was used to solve the model equations for a two-dimensional computational domain representing a single electrode circular electric furnace. The aim of this model was the calculation of the electrical resistance of the slag bath in an attempt to investigate the effect of geometric modifications of the furnace and electrode geometry.

Modelling done on the Falconbridge electric furnace by Sheng *et al.* (1998):

The study by Sheng *et al.* (1998) included an experimental investigation prior to the mathematical modelling to identify the electric potential distribution and the factors that influence the resistance within the furnace. The mathematical modelling included modelling a portion of the bath, which was operated under steady-state conditions and with a no-slip interface between the molten slag and matte (conduction assumed to be the only mode of heat transfer between matte and slag layer). The latter is justified by the counteracting effect of circulation induced by drag from the slag and opposite circulation induced by the temperature gradient.

The model formulation included accounts for the buoyancy effect of carbon monoxide formation at the electrode surface (assumed to originate from the electrode sides) and the potential drop induced by arcing (the main experimental finding). The carbon monoxide flow-rate was based on the electrode consumption rate with specific void fractions ( $\alpha$ ) applied to the first layers of nodes around the electrodes to account for bubble flow. Therefore, the source term associated with the vertical momentum equation comprised of the natural convection force and the buoyancy by CO bubbles.

Arcing from the electrode (simplified as a cylinder) was investigated by applying various boundary conditions to the electrode surface. These conditions included distinction between the potential applied to the electrodes and that experienced by the slag. By assigning higher volts to the electrode surface than that experienced by the slag, account was made for the potential drop induced by arcing.

The interface between the slag and charge were modelled as a velocity inlet boundary condition for fresh slag and matte to enter the domain, where the entry velocities were based on the smelting rate. It is reported that approximately 90% of the electrical energy supplied is consumed by the smelting reactions. It was found that conventional wall functions are not adequate to describe the heat transfer to the charge layer and the heat transfer was modelled empirically by calculating an effective heat transfer coefficient. Sheng *et al.* (1998) describe the smelting zone between the charge and slag layer as a "complex interplay" requiring a better understanding and further modelling detail.

Modelling by Xia and Ahokainen. (2004):

Xia and Ahokainen (2004) performed numerical modelling on a circular three-electrode smelting furnace by considering a third of the furnace slag-bath as the computational domain through the application of symmetry boundaries while also treating the slag-matte interface as motionless.

In this model, the equations of fluid motion and Maxwell's equations for the electromagnetic fundamentals are coupled through magnetohydrodynamic (MHD) and CFD modelling. Electrical modelling involves the solving of the electrical potential equation while the induced magnetic field is assumed to be negligible and no account is given of an externally applied magnetic field. The electrical modelling approach is therefore quite similar to the present model as will be discussed under the Computational Background further on.

For modelling of the upper free surface of the slag layer, convection and radiation heat losses were taken into account by modification of the slag emissivity to incorporate the effect of the charge layer on top. The convection heat transfer coefficient was estimated by correlations relating natural convection from a horizontal plate. These heat losses are added as a heat sink into the energy equation, assigned to the cells comprising the upper surface.

Modelling by Henning *et al.* (2004):

Modelling was done on an open arc single electrode DC electric furnace using Flo++<sup>®</sup>. However, in contrast to the system of interest, the study provides an informative alternative for approaching modelling. The computational domain consisted of a 5° "slice" of the furnace from the electrode towards the furnace shell, including the shell refractory. The various layers (freeboard, slag, matte and refractory) were demarcated using baffle cell groups, allowing individual modelling. Special properties are assigned to the baffle surface elements to ensure interaction between the layers. To account for heat losses to the surroundings, the input power is reduced by a certain percentage rather than incorporating a heat sink.

Modelling performed as consulting work on the Lonmin No.1 furnace (2004):

A study retrieved from the Lonmin furnace database included CFD modelling on the relevant furnace with the focus being on the modelling of flow within the slag bath (one sixth computational domain) and sidewall heat loads. The study accounts for the effects of gas formation at the electrode surface by introducing a bubble momentum-source term (represented by Stokes' law for viscous drag on a sphere) to the computational equations. The latter was assigned to a thin layer surrounding the immersed electrode surface with the intensity varied according to assumed conversion rates of electrode carbon to CO-gas.

Heat source terms were introduced to the same layer that were used for assigning bubble momentum, representing heat generated by electrode consumption, and a thicker layer directly under the electrode for representing the input of electric energy. Heat sinks were assigned to a thin layer on the upper surface of the slag layer. The layer was divided into

different zones and assigned specific energy losses presumed to represent the smelting zones occurring radically from the electrode.

Electromagnetic effects within the slag bath were taken into account by modelling a base situation and scaling the predicted forces according to the simulation requirements and incorporating as momentum source terms. The effects of adjacent electrodes on electrodynamic induced motion were neglected.

The study also includes the consideration of equilibrium and non-equilibrium sidewall conditions, implying operation with a stable, fully developed, freeze lining and without. This was made possible by assigning a limit on the slag viscosity, which was increased by three orders of magnitude after reaching the slag liquidus temperature. All the slag thermal-physical properties were assumed temperature independent, except for the viscosity and density.

#### Confidential consulting work (2006):

A comprehensive study was performed on a six-in-line AC rectangular electric furnace with the aim of investigating causes for corrosion damages to the wall cooling system. The study provides valuable information regarding the physical properties of the system and guidelines to the modelling approach. CFD simulations were performed using the commercial package, Fluent<sup>®</sup> and coupled with finite element analysis (FEA) using the ANSYS<sup>®</sup> package, specifically to model electric and magnetic behaviour. The area around a single electrode, simplified by symmetry, was chosen as the computational domain.

In order to simplify the system, steady state operation was assumed. Joule heating was applied by creating a user-defined function to couple the FEA with the CFD model. The effect of magneto-hydrodynamics was neglected when compared to the magnitude of the buoyant force in the slag.

A thermodynamic survey showed chemical reactions to consume approximately 1% of the total supplied energy and were therefore neglected. In comparison, the smelting process is reported to consume 70% to 80% of the total power input. To account for heat losses, a similar approach to that presented by Henning *et al.* (2004) was followed.

Three different approaches to the modelling of the matte layer were taken. The first approach included a similar approach to Sheng *et al.* (1998), i.e. modelling of the matte as a solid layer. The second approach modelled the slag and matte as two separate liquids but the solution is reported to become numerically unstable and cause convergence difficulties and was discarded. It is recommended that further investigation

into such modelling be done. The last approach modelled the matte as a solid layer but a high thermal conductivity was assigned to account for the effect of fluid circulation.

Little discussion is given regarding the results of the CFD model, except that the slag is well mixed due to buoyant circulation. An invitation for full scale modelling is offered to interpret the heat flux around the full furnace perimeter.

### **2.5.2 Geometric effects**

The model by Jardy *et al.* (1986), although for single electrode operation, showed the furnace geometry to have only a slight effect on the slag resistance. The cylindro-conic shape of the electrode was modelled as a cylinder of which the characteristic diameter, representing the average value of the immersed diameters, was adjusted to account for immersion of the actual shape. The results that were obtained proved the slag resistance to be dependant on the shape of the electrode, affecting electrical side conduction that accounts for 80% of the total conduction.

Jiao and Themelis (1991) showed the electrode-slag interface area as the most decisive factor in determining the geometric factor (a function that relates geometric effects like electrode diameter, electrode spacing, immersion and slag layer depth to the slag resistivity). The geometric factor, and therefore the slag resistance, was found to be inversely proportional to the electrode-slag interface area. Electrode diameter was determined as the next most important factor while the slag depth revealed only a small influence on the geometric factor, which supports the findings of Jardy *et al.* (1986).

### **2.5.3 Electrical current, power and potential behaviour**

In the study by Urquhart *et al.* (1976), the primary dissipation of electrical power was found to be concentrated in a sphere of radius equal to the electrode diameter, located at the electrode tip as presented in Figure 2.5.3.1 (a). 70 Percent of the current was determined to flow by way of the hearth and an increase in the electrical current had little impact on the electrical field distribution except in the spherical region close to the electrode tip.

It was concluded from the study by Sheng *et al.* (1998) that the heat release from the electrode depends greatly on the electric potential distribution. Evident from the figures above is the large heat generation at the electrode surface since the heat generation is proportional to the square of the electric potential gradient according to the mathematical formulation.

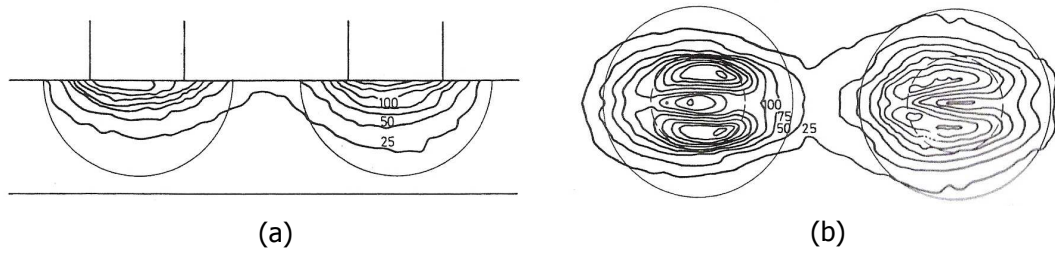


Figure 2.5.3.1 (a and b) Electrical power contours [W] at the electrode tips from the study by Urquhart et al. (1976).

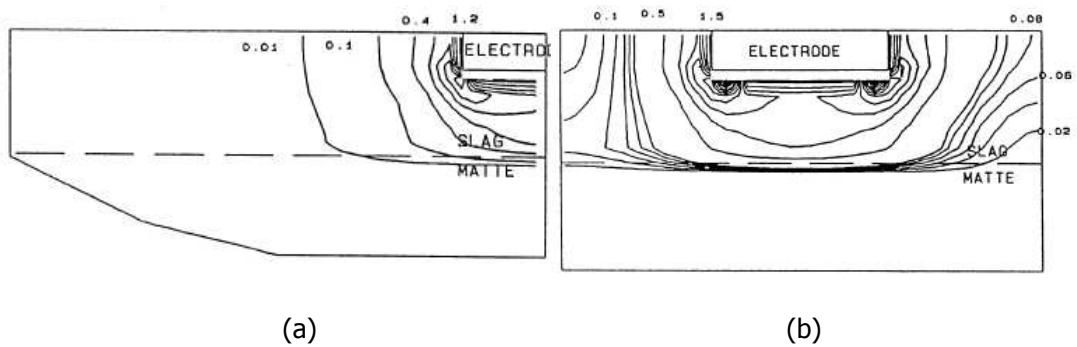


Figure 2.5.3.2 (a and b) The distribution of electric power [W/m<sup>3</sup>] when including a potential drop due to arcing from the modelling done by Sheng et al. (1998).

The electric potential distribution obtained from the modelling by Xia and Ahokainen (2004), Figure 2.5.3.3, show the primary potential drop occurring in the vicinity of the electrode. A direct relationship between electric potential and the temperature distribution was observed - an increase in potential from 120 to 200V resulted in a temperature increase from 1580 to 1800K. This observation brought about concern regarding the application of electric potential. Stated in this study is the concern regarding overheating, associated with excessive application of electric potential or power input, while the risk of sub-cooling is related to the opposite. It is therefore necessary to establish the required operational electric potential/power input range for the particular furnace.

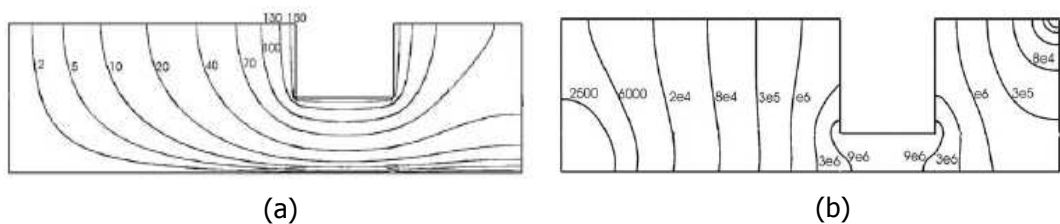


Figure 2.5.3.3 (a and b) Electric potential distribution (V) and (b) and heat ( $W/m^3$ ) distribution along the plane intersecting the longitudinal axis of an electrode from the study by Xia and Ahokainen (2004).

#### 2.5.4 Flow distribution

The majority of the models studied showed the effect of natural convection forces to be prominent compared to electromagnetic forces for inducing flow and causing homogenization of the slag phase. The study by Jardy *et al.* (1976) showed the flow profiles at the electrode surface to be downward. However, compared to the majority of similar studies, which report the liquid with lower density to rise in the region of maximum temperature at the electrode and descend along the cooler sidewalls [Sheng *et al.* 1998, Xia and Ahokainen 2004], this finding is questionable. As mentioned, the study by Sheng *et al.* (1998) specifically points to the occurrence of gas formation at the electrode surface that induces upward buoyant flow.

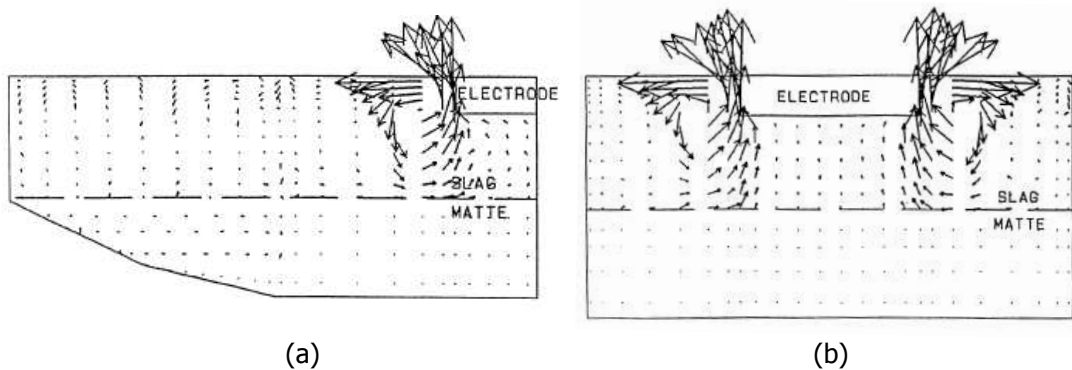


Figure 2.5.4.1 Velocity vectors (m/s) along the plane intersecting the (a) longitudinal and (b) lateral axis of an electrode taken from the study by Sheng *et al.* (1998).

Sheng *et al.* (1998) describes the flow pattern to consist of two circulation areas originating at the electrode surface due to buoyancy forces induced by CO formation and downward motion at the furnace walls due to natural convection. It is concluded from this study that the motion induced from the evolving gas bubbles has a greater effect on slag motion compared to the natural convection forces, which in turn is much greater than electromagnetic forces.

The study by Xia and Ahokainen (2004) shows the occurrence of a vortex within the centre region of the circular furnace. Shown in Figures 2.5.4.2 (a) and (b), the strongest turbulence is observed in the area nearest to the electrodes towards the centre axis. The

optimum flow pattern through the slag would consist of uniform downward flow in the majority of the cross-section and at lower regions in the bath to allow efficient settling of molten metal droplets towards the matte layer and to ensure a homogeneous bath [Xia and Ahokainen 2004].

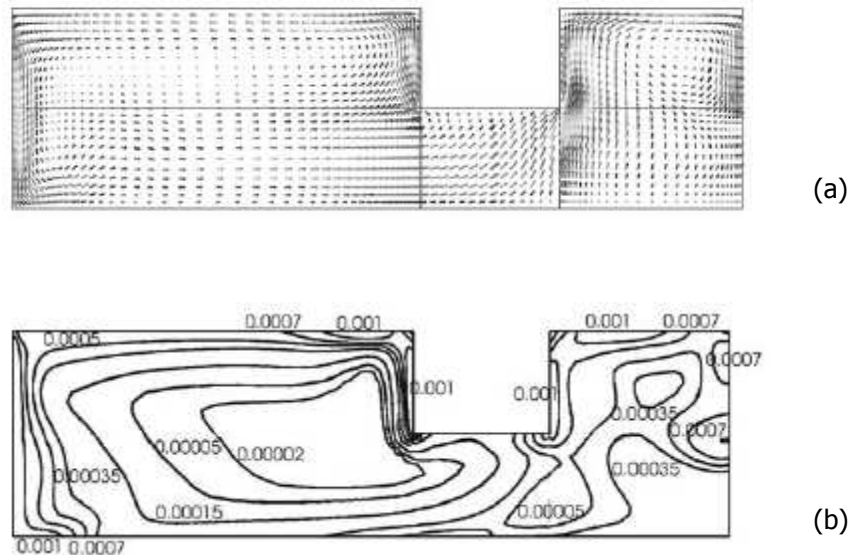


Figure 2.5.4.2 (a) Velocity vectors (m/s) along the plane intersecting the longitudinal axis of an electrode (b) Turbulent kinetic energy distribution ( $m^2/s^2$ ), obtained from the findings of Xia and Ahokainen (2004).

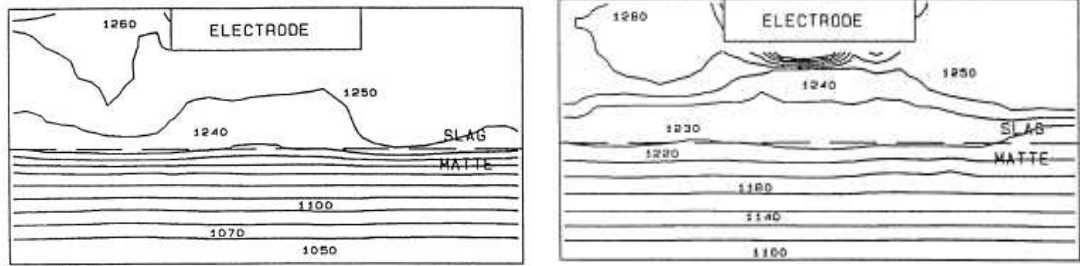
Strong dependencies of the average velocity were reported in the consulting study conducted on the Lonmin furnace No.1 (2004). An increase in the CO-bubble momentum from 25% to 50% resulted in a 46% increase and an increase from 25-75% electrode immersion caused a 60% increase in the average bath velocity.

## 2.5.5 Temperature distribution

The matte-layer was found to be thermally stratified, presumably a result of the coupled top heating and bottom cooling and poor reported momentum transfer from the slag to the matte-layer.

Xia *et al.* (2004) reported only slight differences (25-30K) between the bulk and the highest temperature at the electrode and a non-uniform heat distribution throughout the furnace with the highest generation rate near the electrodes. The results presented in a consulting study (2006), showed the velocity within the slag layer to be relatively small (6cm/s). However, due to the high thermal capacity, it is stated that small convective currents could cause large heat transfer.

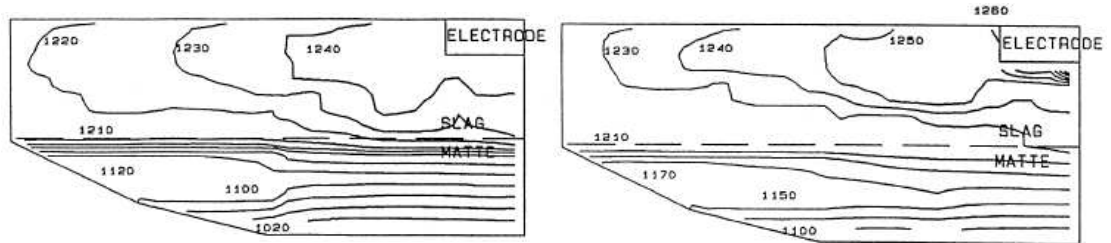




(a)

(b)

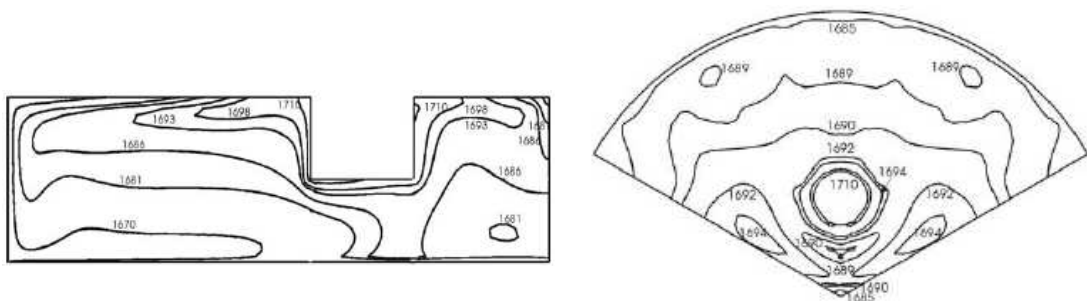
Figure 2.5.5.1 Distributions of temperature [K] taken along a vertical plane through the centre of the electrode (front view) for two cases of applied electrical potential investigated by Sheng et al. (1998).



(a)

(b)

Figure 2.5.5.2 Distributions of temperature [K] taken along a vertical plane through the centre of the electrode (side view) for two cases of applied electrical potential investigated by Sheng et al. (1998).



(a)

(b)

Figure 2.5.5.3 (a) Temperature (K) distribution along the plane intersecting the longitudinal axis of an electrode (b) Temperature (K) distribution along a horizontal section. Taken from the study by Xia et al. (2004).

Definitive relationships relating the sidewall heat flux were identified by the consulting study on the Lonmin No.1 furnace (2004). A significant increase in the sidewall heat flux and consequent temperature homogeneity is reported to result if bath stirring is increased. A 100°C increase in the slag bath temperature was found to be responsible for an increase in 47% of the sidewall heat flux. Overall, the temperature distribution obtained throughout the slag bath by this study was found to be fairly uniform as a result of the high degree of mixing gained.

---

# CHAPTER 3

## COMPUTATIONAL BACKGROUND

---

It is evident that the operation of the electric smelting furnace relies on the interplay between heat transfer, fluid flow and the conduction of electric current. The laws governing these processes have been expressed in a collection of differential equations but require additional relationships for describing the influences that add disturbance to these conservation balances. Examples of such influences relevant to the current system include multi-phase effects, Joule heating and possible turbulence for which additional relationships or empirical models have been developed to compliment the governing equations and provide a closed system of model equations.

The exact analytical solution for such a large set of coupled model equations is not viable and resource must be made to numerical solution techniques for approximating them. Computational Fluid Dynamic (CFD) modelling was developed for this purpose, concentrating the developed numerical methods into a single software package. With sound modelling techniques it would therefore be possible to obtain numerical solutions that resemble the analytical solutions closely and bare a high level of accuracy.

This chapter aims to introduce CFD as a modelling technique by providing an account of the relevant numerical models and the solution technique of which it is constituted. The fundamental governing equations that form the base for numerical modelling are provided. The extent of the electrical modelling requirement is discussed along with the relationships used to implement electric effects in the electric furnace model. The two approaches to multi-phase modelling is presented that include the Volume of Fluid (VOF) model for incorporating a multi-phase layer system and the Discrete Phase Model (DPM) for including the influences of dispersed gas bubbles forming due to the combustion of the immersed carbon electrodes. The computational solving technique as employed by the current version of FLUENT, Fluent 6.3.26, is also discussed.

### 3.1 The governing equations

---

The principles of mass, momentum and energy conservation can be represented by a set of partial differential equations. These equations, presented below in Cartesian coordinates, are valid for evaluating both laminar and turbulent flow in Newtonian fluids and have no known analytical solution [Thiart 2007].

#### Conservation of mass or the continuity equation:

$$\frac{\partial \rho}{\partial t} + \nabla \cdot (\rho \vec{V}) = 0 \quad (3.1)$$

#### Conservation of momentum (x-direction):

$$\frac{\partial}{\partial t}(\rho u) + \nabla \cdot (\rho \vec{V} u) = -\frac{\partial p}{\partial x} + \nabla \cdot (\mu \nabla u) + S^u \quad (3.2)$$

where

$$S^u = f_x + \frac{\partial}{\partial x} \left( \mu \left( \frac{\partial u}{\partial x} - \frac{2}{3} \nabla \cdot \vec{V} \right) \right) + \frac{\partial}{\partial y} \left( \mu \frac{\partial v}{\partial x} \right) + \frac{\partial}{\partial z} \left( \mu \frac{\partial w}{\partial x} \right) \quad (3.3)$$

Equations 3.1 to 3.3 are also known as the Navier-Stokes equations. For the above equations,  $p$  refers to the static pressure while  $f_x$ ,  $f_y$  and  $f_z$  represent the external or "body" forces on a unit volume [Thiart 2007].  $S^u$  represents a momentum source term.

#### Conservation of energy:

$$\frac{\partial}{\partial t}(\rho T) + \nabla \cdot (\rho \vec{V} T) = \nabla \cdot (k \nabla T) + S^h \quad (3.4)$$

For the above equations  $\vec{V}$  denotes the velocity field and  $S^h$  the source term representing the volumetric rate of heat generation respectively [Patankar 1980]. These governing equations can be grouped into a general form, representing the conservation of the dependant property  $\phi$ :

$$\frac{\partial}{\partial t}(\rho \phi) + \nabla \cdot (\rho \vec{V} \phi) = \nabla \cdot (\Gamma^\phi \nabla \phi) + S^\phi \quad (3.5)$$

The first term of the Equation 3.5 accounts for transient variations, the second term for convection, the third for diffusion and  $S^\phi$  allows additional source influences to be implemented.

## 3.2 Electrical modelling

---

A computational model of the electric furnace requires the incorporation of electrical effects to resemble the flow of current, calculate the potential distribution and include resistive heat in the energy balance. The extent of the electrical modelling requirements, especially electro-magnetic effects, needs to be determined in order to assess the impact of modelling constraints on the model outcome. An indication of the coupling between electrical and CFD modelling is therefore provided.

### 3.2.1 Electro-magnetic modelling requirement

It was mentioned that the process of electric smelting hosts a complex interplay between fluid flow, heat transfer and the movement of electrical charge. Also evident is the large difference in electrical conductivity between the slag and matte layer. As supported by the previous modelling studies, the majority of the current is expected to flow through the matte layer between the electrodes [Sheng *et al.* 1998, Urquhart 1976]. From electromagnetic fundamentals, Ampère's law prescribes an association between the current density and an induced magnetic field,  $\vec{b}$  [Davidson 2001]:

$$\nabla \times \vec{b} = \mu \vec{J} \quad (3.6)$$

It is also known that an electromagnetic body force, called the Lorentz force, is presumed to result from the interaction between the induced magnetic field and the imposed current that will act on the conductor [Davidson 2001]:

$$\vec{F} = \vec{J} \times \vec{b} \quad (3.7)$$

The extent of the influence exerted by the induced magnetic field, especially on the matte layer, was investigated since including it in the furnace model will create a considerable modelling requirement.

The matte layer contains a good percentage of ferrites that lend to it its electrical character. However, the extreme temperature at which the matte is maintained results in

the ferrites to possess a paramagnetic character rather than being ferromagnetic. The transition at which all ferromagnets become regular paramagnets occurs at a critical temperature, the Curie temperature, which for ferrites is within the range of 300 to  $\sim 10^3$  K [Aharoni 1996, Bertotti 1998]. At the Curie temperature, the material maintains its saturation magnetization and loses its spontaneous, long range magnetization [O'Handley 2001, Bertotti 1998]. At saturation, maximum alignment of the magnetic moments is at play and an increase in the external field will not increase the total magnetisation.

The matte layer, being regarded as paramagnetic, is therefore expected to exhibit weak magnetic responses, especially at such high temperatures, due to the weak linear effect in the alignment of the magnetic moments since the thermal energy is much larger relative to the magnetic energy [O'Handley 2001]. The magnetic susceptibility for paramagnetic materials, especially at high temperatures, is known to be close to 0, relating to a relative permeability of approximately 1 - only slightly greater than that of free space [Young 1992]. Furthermore, the very high frequency at which current is supplied is considered to bring forth a time period that is small enough to have negligible resulting forces acting on the charge carriers.

The influence of the induced magnetic field is therefore regarded as negligible when compared to other acting forces, such as buoyancy. However, to quantify and prove the relationship between the electromagnetic and buoyancy forces acting on the matte material, a comparative study provided by Davidson (2001) pp. 325-321 and p. 346-347 was conducted. This approach involved a comparison of the velocities brought about through buoyant and Lorentz-force driven flows respectively. The results from the calculations, provided in Appendix B, proved the flow within the molten bath to be mainly buoyancy driven.

#### **Magnetic Reynolds number:**

To further the survey of the magnetic influence, the Magnetic Reynolds number, given by Equation 3.8 below, was evaluated for the matte layer and found to be less than 1 (the actual value being 0.13 for a magnetic permeability,  $\mu_m$  resembling paramagnetic material and a characteristic length,  $l$ , equal to the radius of the furnace). Due to the very low electrical conductivity, the Magnetic Reynolds number for the slag layer is very small ( $Re_m \sim 10^{-5}$ ). The low  $Re_m$  numbers indicates that convection of the magnetic field and magnetic boundary layers within the high current density areas are not likely in the system [Shercliff 1965].

$$Re_m = \mu_m \sigma V \quad (3.8)$$

The justification for neglecting the effect of an induced magnetic field in the modelling of the electric furnace is therefore apparent. A similar assumption was made by the majority of previous modelling studies that included a matte layer [Choudhary and Szekely 1981 , Jardy *et al.* 1976 and Sheng *et al.* 1998].

### 3.2.2 Implementing electrical modelling

Two methods are offered by the Fluent Magneto-hydrodynamic (MHD) package for calculating the current density, i.e. the electric potential and magnetic induction method. Since no external magnetic field is at play on the system and the power input to the furnace is defined in terms of the current, the electric potential method was chosen to include electrical modelling in the CFD simulation.

The electric potential method assumes the induced magnetic field,  $b$ , to be negligible which, according to the survey above is considered to be a valid assumption. Although no magnetic field is present in the furnace system, Maxwell's electromagnetic equations are solved and coupled with the CFD conservation equations. These equations, Equation 3.9 – 3.14, are used to derive the electric potential equation, Equation 3.16, which is solved by the electric potential method. In the absence of an external magnetic field,  $B$ , the electric potential equation reduces to Ohm's law, Equation 3.13 [Fluent MHD manual, Davison 2001].

Ampère's law and charge conservation:

$$\nabla \times \vec{B} = \mu \vec{J}, \quad \nabla \cdot \vec{J} = 0 \quad (3.9, 10)$$

Faraday's law and the solenoidal constraint on the magnetic field,  $\vec{B}$ :

$$\nabla \times \vec{E} = -\frac{\partial \vec{B}}{\partial t}, \quad \nabla \cdot \vec{B} = 0 \quad (3.11, 12)$$

Ohm's law and the Lorentz force:

$$\vec{J} = \sigma(\vec{E} + \vec{V} \times \vec{B}), \quad \vec{F} = \vec{J} \times \vec{B} \quad (3.13, 14)$$

The electric field is expressed as the gradient of the electric potential ( $\phi$ ):

$$\vec{E} = -\nabla\phi \quad (3.15)$$

The electric potential equation, below, is obtained by manipulating Equations 3.10, 3.13 and 3.15:

$$\nabla^2\phi = \nabla \cdot (\vec{V} \times \vec{B}) \quad (3.16)$$

Heat generation through resistive heating, Joule heating, is coupled with the energy equation through the source term [Fluent MHD manual]:

$$q = \frac{j^2}{\sigma} \quad (3.17)$$

An adequate modelling environment is therefore available for including the electrical character of the smelting furnace and to provide interactive coupling with the standard CFD equations through the use of source terms.

### 3.3 Multi-phase modelling

---

The electric smelting process is a complex multi-phase system. For present modelling purposes, multi-phase modelling is required for including the interaction between the two molten layers, i.e. the slag layer on top of the matte layer. A further gas phase is also required for simulating the continuous CO-gas bubble formation at the immersed electrode tips. To meet these requirements, the Volume of Fluid (VOF) model is selected under FLUENT's diverse range of multi-phase models for modelling the two liquid layers while the discrete phase model (DPM) is applied for the latter.

These two multi-phase models differ with respect to the reference frame used for handling the different phases. The VOF model employs an Eulerian approach that focuses on specific locations in space through which the fluid flows. In contrast, the DPM model applies a Lagrange approach where attention is focused on individual particles and how they move through space and time [C.T.Crowe 2006].



### 3.3.1 The volume of fluid (VOF) multi-phase model [Fluent manual]

The VOF model is used for describing a system containing more than one continuum phase. It is therefore more comprehensive to describe the approach taken by the VOF model as Eulerian-Eulerian. Each fluid phase is accounted for through the application of a volume fraction,  $\alpha$ , per computational cell and a volume-average system is used for calculating properties and field variables. The use of volume-averaged properties allows the solution of a single momentum and energy equation. The velocity field is therefore shared among the phases while the variables for energy ( $E$ ) and temperature are mass-averaged by the VOF model. For Equation 3.18,  $E_q$  is based on the specific heat of the particular phase:

$$E = \frac{\sum_{q=1}^n \alpha_q \rho_q E_q}{\sum_{q=1}^n \alpha_q \rho_q} \quad (3.18)$$

Therefore, the variables and properties in a particular cell are entirely associated to one phase ( $\alpha = 1$ ) or to a mixture ( $0 < \alpha < 1$ ). As an example, the density for a two phase system is treated as follows:

$$\rho = \alpha_2 \rho_2 + (1 - \alpha_2) \rho_1 \quad (3.19)$$

#### **Treatment at the interface:**

In the current system, the slag is regarded as the primary phase and the matte secondary. In order to track the interface between the phases, the continuity equation for the volume fraction of the secondary phase will be solved while the primary phase volume fraction is calculated from the constraint:

$$\sum_q \alpha_q = 1 \quad (3.20)$$

The volume fraction continuity equation for the secondary phase, phase  $q$ , will be of the following form:

$$\frac{1}{\rho_q} \left[ \frac{\partial}{\partial t} (\alpha_q \rho_q) + \nabla \cdot (\alpha_q \rho_q \vec{V}_q) \right] = S_{\alpha_q} + \sum_{p=1}^n \left( \dot{m}_{pq} - \dot{m}_{qp} \right) \quad (3.21)$$

Where,  $\dot{m}_{qp}$  represents the mass transfer between phase  $q$  and phase  $p$  and  $\dot{m}_{pq}$  the inverse in the above equation.

In order to establish an interface, the cells at the transition area need to be interpolated between the respective phases. The Comprehensive Interface Capturing Scheme for Arbitrary Meshes (CICSAM) was chosen from the various interpolation schemes offered by the Fluent solver as will be discussed in Chapter 4.

### 3.3.2 The discrete phase model (DPM)

As stated, the DPM model employs a Lagrangian reference frame with respect to the treatment of the “discrete phase” or particles while the continuum is represented by the Eulerian frame of reference. The Lagrangian approach can be applied through the resolved-surface or point-force treatment [C.T.Crowe 2006].

The resolved-surface method includes the particle volume-interface when calculating the continuous-fluid solution. The actual particle shape can therefore be taken into account, however at the computational expense of solving at a high resolution around the interface, which for most purposes is practically unfit.

The point-force method neglects the particle volume and assumes a pointwise representation and is therefore more feasible. A large number of particles are treated as computational “parcels” that represent a group of particles interacting with the fluid and having the same characteristics. The position of the parcels is henceforth determined by Newton’s equation of motion [Patankar 1980]. The parcel size is determined as to be less than the local grid resolution on the continuous phase [C.T.Crowe 2006].

For the current system, two-way coupling between the particles and the fluid is essential. The particle equations, represented by ordinary differential equations through the Lagrangian approach, must therefore be solved in conjunction with that of the continuous-phase, represented by partial differential equations. This is achieved by adding the fluid-particle term as external forces to the equation of fluid motion [C.T.Crowe 2006].

The force balance applied by the DPM on a particle [Fluent multi-phase manual]:

$$\frac{du_p}{dt} = F_D(u - u_p) + \frac{g_x(\rho_p - \rho)}{\rho_p} + F_x \quad (3.22)$$

where  $F_x$  accounts for additional acceleration and  $F_D(u - u_p)$  the drag force per unit of particle mass.  $F_D$  is determined by the following relation:

$$F_D = \frac{18\mu}{\rho_p d_p^2} \frac{C_D \text{Re}}{24} \quad (3.23)$$

For these equations,  $u$  represents the fluid phase velocity,  $u_p$  the particle velocity,  $\mu$  the molecular viscosity of the fluid,  $\rho$  the fluid density,  $\rho_p$  the density of the particle and  $d_p$  the particle diameter. The relative Reynolds number is required for Equation 3.23 and is obtained by the following relation [Fluent multi-phase manual]:

$$\text{Re} \equiv \frac{\rho d_p |u_p - u|}{\mu} \quad (3.24)$$

Several empirical relationships are available for estimating the drag coefficient,  $C_D$ . However, for current modelling purposes, the spherical drag-law is used over a range of Re:

$$C_D = a_1 + \frac{a_2}{\text{Re}} + \frac{a_3}{\text{Re}^2} \quad (3.25)$$

where  $a_1$ ,  $a_2$  and  $a_3$  are constants for representing the smooth spherical particles [Fluent multi-phase manual].

## 3.4 Computational solution

---

The FLUENT solver applies the finite-volume approach to discretize the computational domain into a finite set of control volumes or cells for which the governing equations are individually solved. Mentioned previously, exact analytical solution to the model equations is not possible. The technique used by Computational Fluid Dynamics (CFD) is therefore to convert the governing differential equations presented in Section 3.1 into algebraic form in order to make the computational solving feasible.

The conversion to algebraic equations is done by describing the system dependant variables in terms of an advection scheme which involves describing a property at a specific point by the properties from adjacent points. The default First-Order Upwind Scheme is used in the present study which is the simplest advection scheme available in terms of computational effort and is

based on the reasoning that a dependant variable will be influenced more by “upstream” values compared to those “downstream” [Thiart 2007].

The governing equations allow the solving of the dependant variables; however a computational challenge is obtaining the unknown static pressure field that forms an important source term in the momentum equations. No obvious answer exists for the latter but a computational technique has been developed which involves the extraction of the pressure from the continuity equation. The reasoning is that a *correct* static pressure field will result in a velocity field that again will satisfy the continuity equation [Patankar 1980]. For this reason pressure-velocity coupling algorithms have been developed.

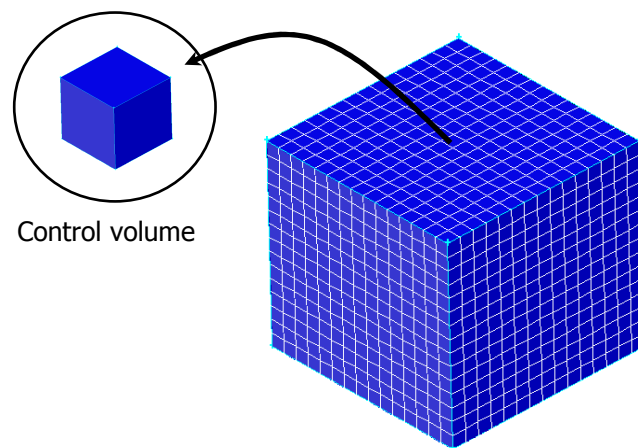


*Figure 3.5.1 The computational domain is discretized into a finite set of control volumes.*

The FLUENT pressure-based solver allows a choice between a segregated and a coupled algorithm. The segregated solver solves the governing equations one to another in sequence, through an iterative approach while the coupled solver solves the momentum and pressure correction equations in a coupled manner. A trade-off exists between these solvers since the coupled solver is more efficient where computational speed is concerned but requires more memory (1.5 to 2 times) compared to the segregated solver [Fluent manual]. For the current study the segregated solver is preferred due to the sequential incorporation of model influences like electrical potential and since it complements the numerical structure of the discrete phase model where the governing equations of the particles are solved only in a segregated manner.

The FLUENT solver provides a selection of several segregated algorithms but the choice falls on the Pressure-Implicit with Splitting of Operators (PISO) algorithm for the modelling of the electric furnace. This algorithm provides an increased efficiency for pressure-velocity convergence since it allows the momentum balance to be satisfied faster by new velocities while correcting irregularities in mass flux and pressure at the faces of highly skewed mesh elements.

The PISO algorithm is recommended [Fluent manual] as it is specifically suited for modelling transient flow problems using a large time-step, which is true for the proposed model.

The governing equations however must be discretized in both space and time, since it is made evident that the modelling of the electric furnace will require transient solving. The discretization for the time-dependant equations with respect to space is the same as those under steady state and is achieved through the application of an advection scheme as previously discussed. Discretization in time requires a different approach towards integration. Two integration schemes are provided by the FLUENT solver, the implicit and explicit time integration schemes.

In the current version of FLUENT the pressure-based solver, however, only permits the use of the implicit time scheme (Equation 3.26) where a variable is evaluated at the future time level compared to the explicit scheme (Equation 3.27) which describes a variable based on the current time level. For the equations below,  $F$  represents any spatial discretization function,  $\phi$  a scalar quantity and  $n$  the time level [Fluent manual, Thiait 2007]:

$$F(\phi^{n+1}) = \frac{\phi^{n+1} - \phi^n}{\Delta t}, \quad F(\phi^n) = \frac{\phi^{n+1} - \phi^n}{\Delta t} \quad (3.26, 27)$$

The selection of the modelling techniques is supported by proper numerical control which is provided by under-relaxation factors that regulate the degree of change a variable is to undergo during iteration. By adjusting the under-relaxation factors, convergence of the model residuals can be encouraged. Convergence of the model residuals is obtained through close monitoring of the scaled residuals that need be reduced to a value below the convergence criteria, which is selected based on the degree of accuracy required. The details regarding the solution controls and model settings are provided in Section 4.5.

---

# CHAPTER 4

## METHODOLOGY

---

Modelling of the complex system of electric smelting as accurately as possible requires careful design of the computational domain and effective use of the numerical models provided by the CFD package. For this reason a systematic approach was followed in the model development. In this chapter, the reasoning behind the model development is discussed while the details regarding the creation of the solution domain and the model specifications are provided. This chapter also identifies the major model assumptions which are thoroughly considered and argued. An account is given of the computer system used to process the computational load and the method of monitoring the simulation progress.

### 4.1 Model development

---

The important choices that were made in the model development are discussed along with the steps that were taken to create a complete and representative CFD model for the electric furnace.

#### 4.1.1 Deciding on a model geometry

The review of previous modelling attempts on the circular furnace revealed a general simplification in the modelling that involves dividing the computational domain symmetrically. These attempts however do not include a time-variant power input and is likely to lead to asymmetrical behaviour, especially in electrical field and current density due to the varying current paths between the electrodes. An investigation into the dynamics and influences on the slag and matte layers will therefore require the modelling of the full furnace geometry and the inclusion of the electrodes for enabling the three-phase energy input.

This modelling requirement places a heavy weight on the computational capacity of the model. It was therefore considered a sound approximation to only model the bottom part of the furnace up to the concentrate layer, neglecting the furnace freeboard and roof. Compensation for this assumption was made by assigning a representative boundary condition at the top of the concentrate layer.

#### **4.1.2 Deciding on the extent of modelling**

The solving of the model equations showed different time-scales of convergence. For example, the distribution of electrical current throughout the computational domain was found to be an instantaneous phenomenon, occurring within a few iterations, while the development of a fully converged temperature and velocity field (converged in this instance refers to no observed changes with time) takes a considerable number of time-steps: the velocity field however to a lesser degree than the temperature gradients.

To meet the project objectives and time constraint, a solution of completely converged dependant variables was therefore pursued for one electrode immersion (a typical electrode immersion of 35 % into the slag layer) only, while the investigation into the effect of different electrode immersions was left to the influences on current density, electric potential and Joule heat. Information regarding the velocity and temperature distributions (assumed not to have an influence on the electrical related dependant variables that are investigated) for further electrode immersions therefore falls beyond the scope of this study.

#### **4.1.3 Steps towards creating the complete furnace model**

The establishment of a comprehensive and stable model base case (35 % electrode immersion) requires numerous initial trials and conservative initial simulations for investigating the effects of different model set-ups, model parameters and solver settings. A step-wise approach with an increasing level of complexity was therefore followed to develop the desired CFD furnace model. This involved concentrating on the following events in sequence:

- A fair amount of time was allocated to construct a furnace geometry that could be meshed with the available meshing tools in the pre-processing package. The resulting grid had to consist of a conformal mesh containing good quality cells. This involved numerous meshing attempts and revision of the furnace geometry. The successful computational domain was evaluated during the initial simulations where

refinement of the grid was performed in areas with high variable gradients in order to establish a grid independent solution.

- The stability of the energy balance was quickly observed to be of primary importance in setting up the model. As will be discussed later, the effect of smelting and heating of the furnace material is incorporated through energy sinks, the effect of which, along with thermal boundary conditions, was investigated on a steady state model.
- The application of electrical current in conjunction with the energy balance was investigated by first modelling a steady state model and assigning a fixed current input to boundaries representing the electrode-slag interface. Progress to transient electrical input was made by creating a current input through volume sources representing the electrodes by means of user defined functions (UDF's).
- The modelling of a fluid matte layer requires application of the Volume of Fluid (VOF) multiphase model for tracking the interface between the matte and slag (both fluids). The use of the VOF model compels the simulation of transient conditions and adds to the instability of the numerical system. The matte was therefore first modelled as a solid layer before attempt was made to model it as fluid continuum.
- Mixing within the molten bath was first left to the effects of natural convection, made possible through temperature dependant densities. The additional momentum induced through bubble formation at the electrode surface was further investigated by enabling the Discrete Phase Model (DPM). The substantial velocity increase within the slag layer reduced model stability which required investigation into the settings of the DPM coupled to the current model.
- The effect of including turbulence modelling was investigated once the flow under laminar conditions had been fully developed.
- A third phase consisting of a thin, highly viscous slag layer between the slag and matte layers was introduced once the two phase system had been fully investigated. This was to permit the investigation of a "false bottom" or "mushy layer" commonly found in the actual furnace due to the build-up of chromite and magnetite deposits. It is believed that the modelling of a normal slag layer, even with a temperature dependant density and viscosity, would over-predict flow within



the bottom slag region since it is reported to be fairly stagnant in lower part due to the presence of highly viscous material.

- The influence of electrode immersion on the electrical potential, current density and Joule heat distribution was investigated by creating two additional furnace geometries. Two extremes beyond the previous 35 % electrode immersion model were created which included a 15 % and 55 % electrode immersion into the slag layer. This required revision of the base case model geometry, remeshing of the geometry volumes and reassigning boundary conditions and zone types.

Overall, creating a CFD model involves three successive stages of development: During the pre-processing stage the model geometry and computational grid are created. The pre-processing stage is followed by the solving of the CFD problem which entails the selection of computational settings and the solving of the appropriate governing equations. The effect of different solver settings on the stability of the model was investigated throughout, as will be discussed further on. The final post-processing stage involves the presentation and interpretation of the results while improvements to the current model are considered.

## **4.2 Creating the solution domain**

---

The pre-processing of the furnace model was performed in the commercial pre-processing package accompanying FLUENT, namely Gambit 2.3.16 (2006). This entailed the construction of the furnace geometry, assigning boundary- and zone types and fitting the geometry with an appropriate grid.

### **4.2.1 Geometry**

The geometry for the bottom part of the furnace was created based on the actual furnace dimensions. The actual geometry was simplified to create a model geometry that could be fitted with an effective volume mesh by the available meshing tools in Gambit. This entailed uniting a few of the refractory linings found in the hearth of the actual design. The geometry also had to be subdivided considerably in order to obtain a good quality hexahedral mesh as will be discussed in Section 4.2.3.

The volumes representing the electrodes were initially created as cylindrical volumes but were chamfered along the bottom edges to represent the phenomenon of "pencil" that is commonly found during actual operation. The base case model included a 35%

electrode immersion (35 % of the slag layer depth) and material layer depths of (measured along the central vertical axis of the furnace): concentrate layer 200 mm, slag layer 1200 mm and matte layer 800 mm. The final base case model geometry is presented in Figure 4.2.1 below. A thin 75 mm layer at the bottom of the slag layer is converted to a highly viscous intermediate layer in later simulations to investigate the presence of the third phase, stated previously.

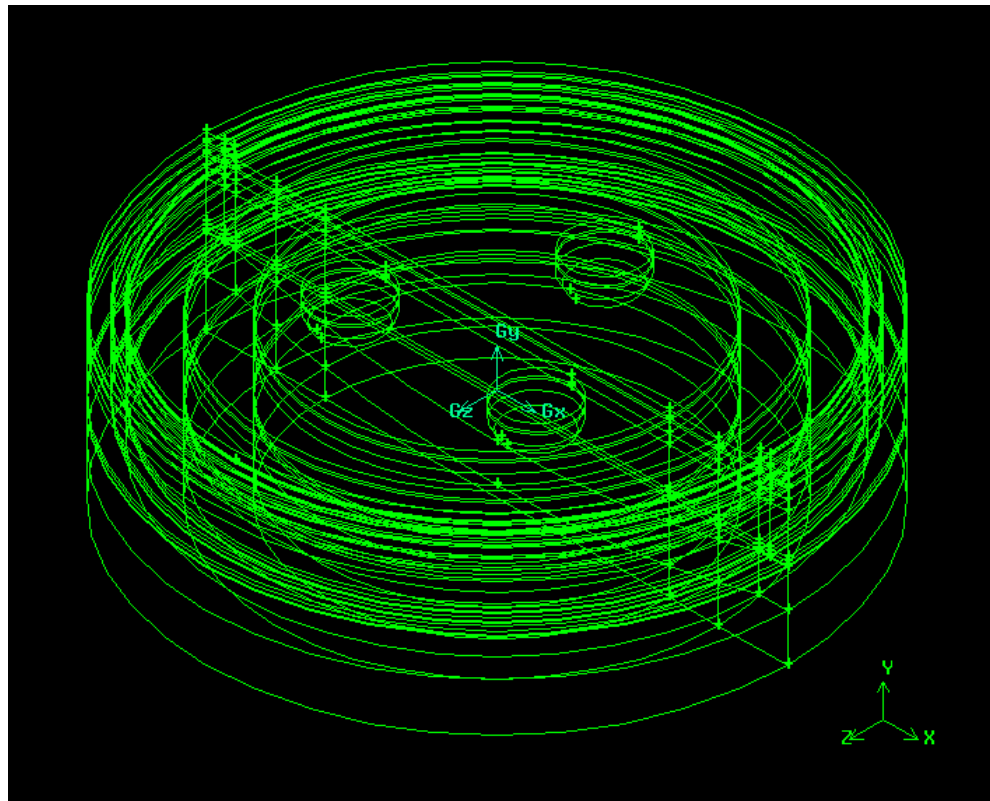
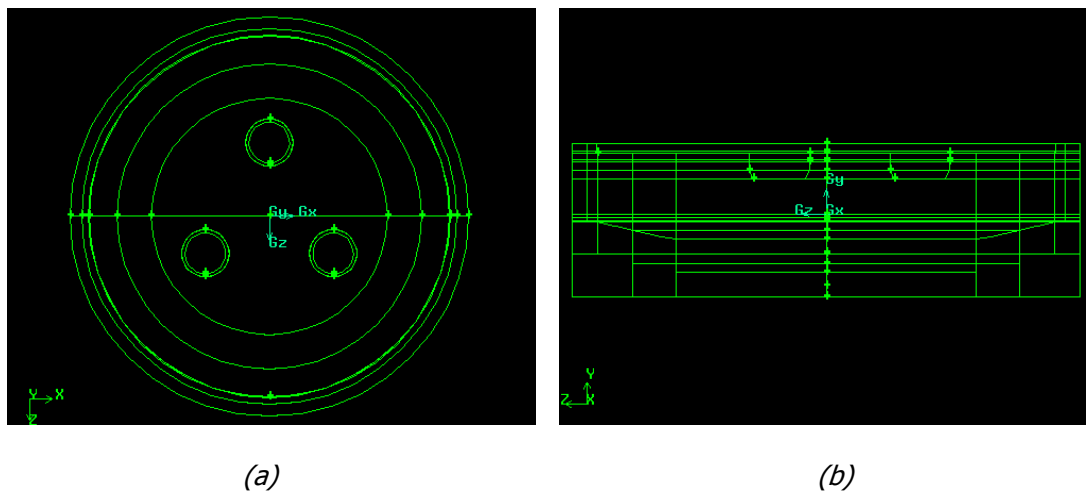
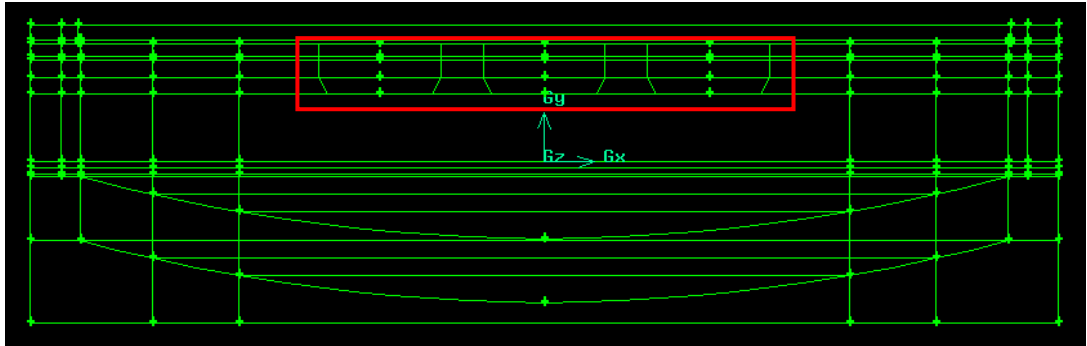


Figure 4.2.1 An isometric view of the furnace geometry created in Gambit.

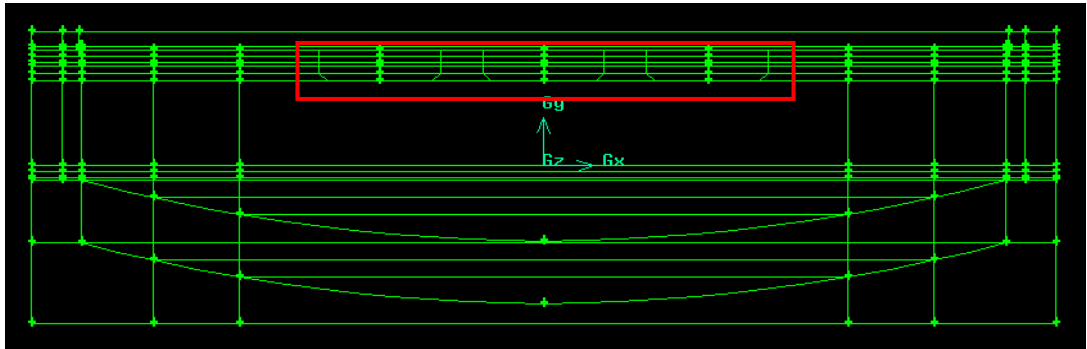


Figures 4.2.2 a and b. The furnace geometry (35 % electrode immersion) portrayed at different orthographic projections.

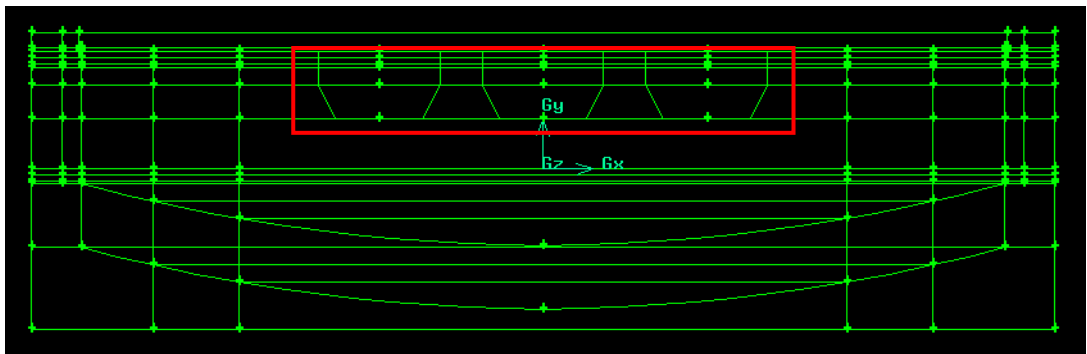
As stated, creating the models for the deeper and shallower electrode immersions required a revision of the base case geometry which had to be remeshed entirely. The same material layer depths were used for these models.



(a)



(b)



(c)

Figures 4.2.3 a, b and c. Front view of the furnace geometry created for (a) 35 %, (b) 15 % and (c) 55 % electrode immersion into the lag layer. The immersed electrodes are framed in red.

#### 4.2.2 Assigning zones and boundary conditions

The different material zones, depicted in Figure 4.2.4 above, were assigned to the volumes after the geometry had been successfully created. Apart from the slag layer, which was immediately assigned the character of a fluid continuum, the matte layer was first modelled as a solid upon which it was also converted to a fluid continuum in later model attempts. Provision was further made for the solid layers of the concentrate, furnace sidewall and hearth as well as the copper cooler on the outer perimeter of the furnace sidewall. The volumes representing the electrodes were also assigned as solid continuums.

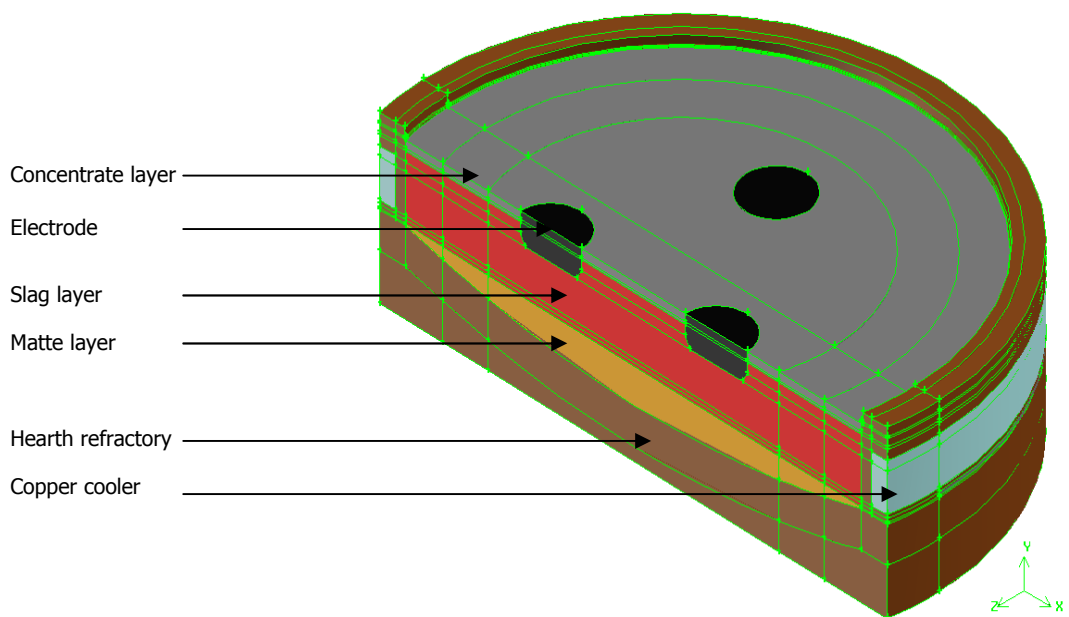


*Figure 4.2.4 The different continuum types are assigned to the geometry (35 % electrode immersion) in the pre-processing package.*

Several boundaries were assigned to the geometry to facilitate specification further on in the solver set-up. Wall boundaries were assigned to the following entities:

- The top electrode surfaces to allow electrical current to enter and leave the model.
- The submerged surfaces of the electrodes to allow easy identification for bubble release when the DPM model was activated.
- The surface between the slag and concentrate layer to allow specification of a boundary where the injected bubbles could escape the system.

- The top surface of the concentrate layer to allow specification of the conditions to compensate for the assumption of neglecting the top part of the furnace in the model.
- The sidewall and furnace bottom such that the conditions for convective cooling could be assigned.
- The outer wall of the copper cooler to allow specification of a fixed temperature.

#### 4.2.3 Creating the grid

As stated previously, the furnace geometry was subdivided into several sections as required by the Cooper meshing method in order to obtain a good quality hexahedral mesh. The hexahedral grid is preferred due to its higher convergence efficiency compared to a tetrahedral grid and since it is a prerequisite of the surface tracking method incorporated by the VOF multi-phase model [COST, Fluent manual]. Hexahedral grids also require approximately half the storage space and CPU time compared to tetrahedral grids having the same distribution of vertices. This is due to the increased number of edges in the case of a tetrahedral mesh [Biswas 2006].

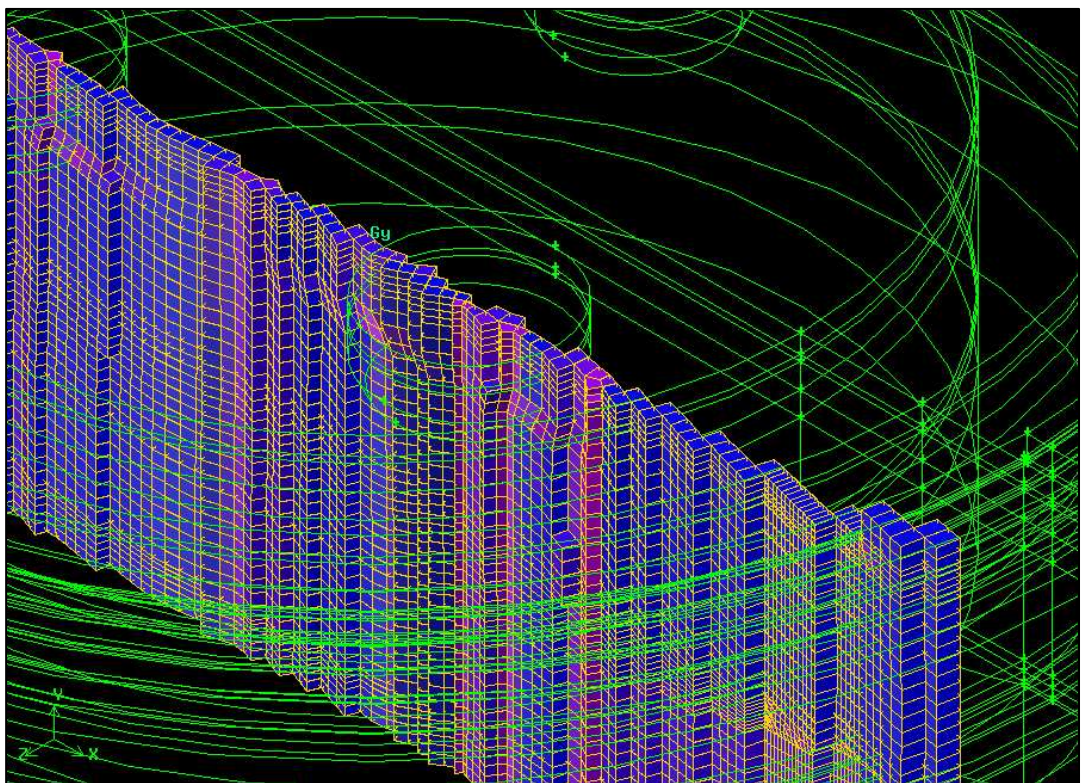
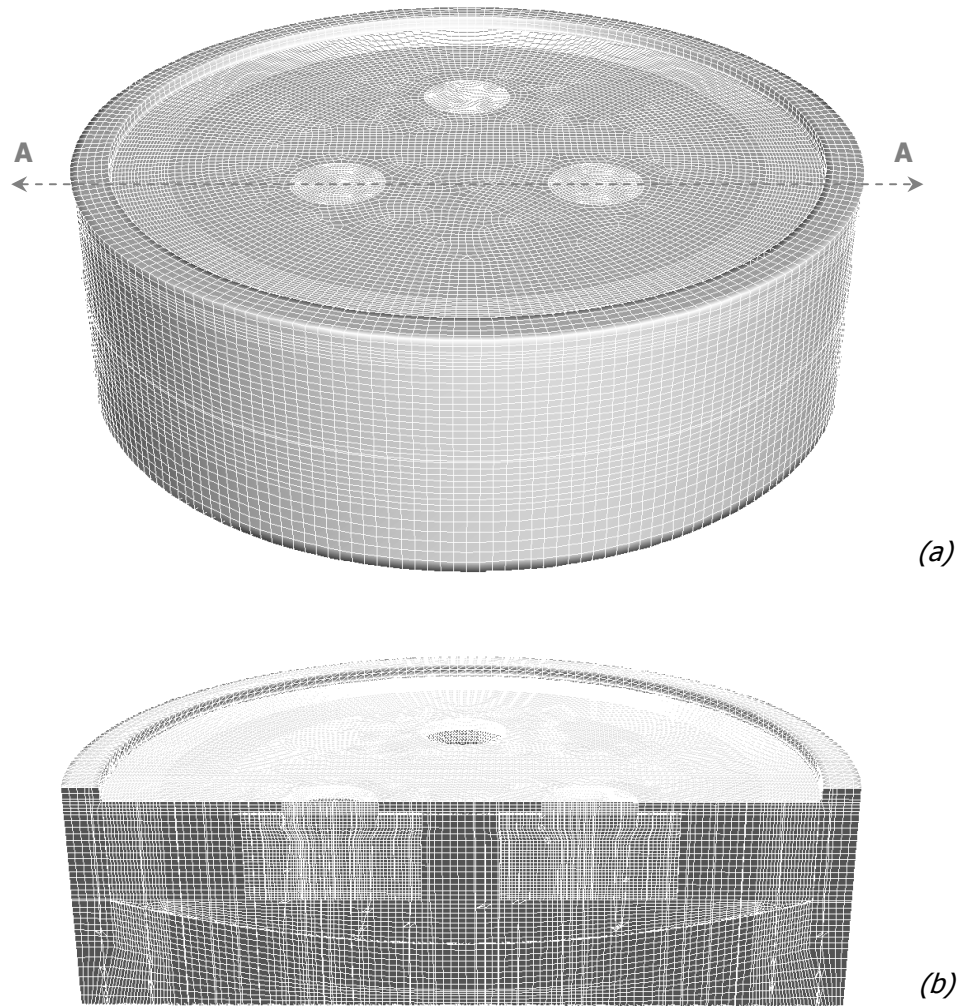


Figure 4.2.6 The meshed structure created on the furnace geometry, displayed on a vertical plane within the front of the furnace.



*Figure 4.2.6 a and b. (a) The meshed domain for the 35 % electrode immersion furnace model. (b) The meshed domain, partitioned by a cross-section AA, revealing the refined mesh around the electrodes.*

A necessity for any CFD study is the establishment of grid independence. Care was taken to ensure that enough elements were created for capturing the character of the system. The grid refinement was based on a qualitative analysis which involved establishing a mesh resolution that would be adequate for capturing the high gradients in the model variables. The grid created in Gambit was therefore further refined in the vicinity of the electrodes due to the large variable gradients, especially current density, observed in these regions.

A fixed zone for grid refinement was required due to the periodic nature of current flow to and from the electrodes and therefore continuously varying gradients of current density and electric potential. Gradient fitted refinement was therefore not possible. The grid refinement was performed within Fluent 6.3.16 through the application of the hanging

node adapting method. Second order refinement within a cylindrical area, having a 1.3 m radius and the centre of the electrodes as centre-line, was found to be adequate for capturing the electric gradients.

Further refinement was performed in the complete and final model that included the highly viscous intermediate layer between the slag and matte so as to ensure that enough cells were present for capturing the two fluid interfaces between the three phases. This resulted in a final furnace model with approximately 850 000 computational cells - an extensive computational assembly. The characteristics of the computational grids that resulted for the various furnace models are described by the following table:

*Table 4.2.3 Specifications of the computational grid for the different furnace models.*

<b>Furnace model (electrode immersion)</b>	<b>15 %</b>	<b>35 %</b>	<b>55 %</b>
<b>Total elements (all hexahedral)</b>			
Before adapting (mesh created in Gambit)	423260	448840	423260
After adapting Fluent (two phase model)	614094	643090	615711
After adapting in Fluent (three phase model)	-	847756	-
<b>Quality measurements (of the worst element)</b>			
EquiSize Skew	0.53487	0.4564	0.5180
EquiAngle Skew	0.53487	0.4565	0.5180
Aspect Ratio	7.2911	6.8489	7.2910
Cell expansion ratio between the range 0.8-1.2	83.79%	84.39%	83.46%

These computational grids are considered to be of a satisfactory quality since the skewness of the worst element falls within the range characterized as being of a good quality 0.25-0.5. The aspect ratio, the value for a perfect equilateral element being 1, for the worst element is quite large but the majority of the grid still falls within an acceptable range. The majority of the grid (84.39 %) also falls below the expansion ratio of 1.3, therefore keeping the truncated error small [COST]. The final grid is presented in Figure 4.2.5 with Figure 4.2.6 (b) showing the adapted region surrounding the electrodes.

## 4.3 Model specifications

---

The model set-up was performed once the satisfactory grid was loaded into the Fluent 6.3.16 (2006) solver and had been adapted. The systematic procedure for setting up the model included compiling the user defined functions (UDF's), enabling of the MHD module, setting the material properties, specification of the model parameters, boundary-and operating conditions, the setting-up of the solver and enabling monitors for tracing the model behaviour. An account of how each of these stages was defined and managed is provided in detail below:

### 4.3.1 Physical properties

The comparison and selection of the physical material properties is provided in Appendix A. To reduce computational effort, piece-wise temperature dependency was assumed for the slag and matte density, while average values were determined for the remaining thermo-physical properties over the expected temperature range:

$$\bar{\Phi} = \frac{\int_{T_{min}}^{T_{max}} \Phi(T) dt}{T_{min} - T_{max}} \quad (4.1)$$

Where  $\bar{\Phi}$  denotes the averaged thermo-physical property and  $T_{min}$  and  $T_{max}$  the minimum and maximum temperatures expected within a material layer. For the slag layer a temperature range from 1600 K to 2000 K was selected and for the matte layer 1500 K to 1900 K. Table 4.3.1 below provides the values assigned to the material properties (references according to the reference list provided in Appendix A):

Initial simulations showed the heat generation within the slag layer to be very sensitive to the value of the electrical conductivity (discussed in Section 5.3.1), therefore making the use of a constant value a necessity. The electrodes were assigned similar properties to that of the slag layer since an investigation revealed the electrical current to be distributed faster into the model. The heat generated within the electrodes due to resistive heat therefore had to be removed by means of energy sinks, an example of which is provided in Appendix C.

Further miscellaneous materials that were also specified includes carbon-dioxide for approximating the carbon-monoxide gas-bubbles being released from the electrode surface and copper for representing the copper cooler. The default values as specified by



Fluent 6.3.16 for these physical properties were applied except the electrical conductivity of copper was considerably reduced due to instability in the flow of electrical current observed during the initial stages of the simulation.

*Table 4.3.1 The physical properties of the material layers present in the furnace model.*

Material layer	Value	Units	Reference
<b>Slag (fluid)</b>			
Density	2775.74 to 2474.06 (1400 K to 2600 K)	kg/m <sup>3</sup>	Jones [6]
Viscosity	0.123	kg/m.s	Jones [6]
Thermal conductivity	2.3	W/m.K	Chekhovskoi [1]
Heat capacity	1373	J/kg.K	Jones [6]
Electrical conductivity	22	mho/m	Hadley [3]
<b>Matte (solid and fluid)</b>			
Density	4428.99 to 3871.60 (1400 K to 2600 K)	kg/m <sup>3</sup>	Sundström [8]
Viscosity	0.0032	kg/m.s	Hadley [3]
Thermal conductivity	17	W/m.K	Sheng [7]
Heat capacity	890	J/kg.K	Hadley [3]
Electrical conductivity	93000	mho/m	Sheng [7]
<b>Concentrate (solid)</b>			
Density	1400	kg/m <sup>3</sup>	Hadley [3]
Thermal conductivity	1.2	W/m.K	Hadley [3]
Heat capacity	1100	J/kg.K	Hadley [3]
Electrical conductivity	1.2	mho/m	Hadley [3]
Magnetic permeability	$1.257 \times 10^{-6}$	h/m	-
<b>Furnace hearth and wall (solid)</b>			
Density	2083	kg/m <sup>3</sup>	Refractory sheets
Thermal conductivity	4	W/m.K	Refractory sheets
Heat capacity	960	J/kg.K	Refractory sheets
Electrical conductivity	1	mho/m	Refractory sheets
Magnetic permeability	$1.257 \times 10^{-6}$	h/m	-

The properties for the intermediate slag layer above the matte layer were assumed to be similar to the slag, however, the viscosity was increased by an order of magnitude and the thermal conductivity was halved to represent the occurrence of the chromite and magnetite “mushy layer”. This assumption was based on accounts describing the nature of this intermediate layer [Utigard, 1994; Nell 2004; Eksteen 2007].

### 4.3.2 Boundary conditions

The boundaries created during the pre-processing stage are specified within the FLUENT solver. These specifications were determined to approximate the actual operation of the furnace as closely as possible. All solid walls in contact with fluid were specified as default no-slip stationary walls. The user-defined boundary conditions are summarized by the following table:

*Table 4.3.2 Summary of the boundary conditions applied to the furnace model.*

Boundary name	Description	Specifications
Concentrate_top	Top layer of concentrate	Heat transfer coefficient: 25 W/m <sup>2</sup> K Free stream temperature: 833 K
Hearth_side	Sidewall and bottom for the hearth	Heat transfer coefficient: 100 W/m <sup>2</sup> K Free stream temperature: 300 K 0 V (ground potential)
Copper_cooler	Sidewall of the copper cooler	Surface temperature: 320 K 0 V (ground potential)
Electrode1-3	Top surface of electrodes	Conducting wall with zero current density: 0 A/m <sup>2</sup>
E1-3	Surface of electrodes in contact with slag	Coupled, injection boundary
Slag_to_concentrate	Layer between slag and concentrate for specifying the escape of bubbles	Coupled, Escape boundary (DPM)

### 4.3.3 Operating conditions

The furnace was set to operate under atmospheric pressure and an operating density of 2474 kg/m<sup>3</sup>, the lowest fluid density expected within the system, which is advised for improving convergence [Fluent manual]. The system is set to operate under gravitational acceleration of -9.81 m/s<sup>2</sup>, therefore enabling natural convection to take place.

### 4.3.4 Energy sinks

It was mentioned that the operation of the actual furnace involves the tapping of the slag and matte layers. The modelling of such a system with moving multi-phase layers is considered to be too complex since it would require extensive tracking of the interface between the layers and inflow boundaries for both the slag and matte for maintaining inventory and involve meshing challenges. It was therefore decided to model stationary material layers but to compensate for the heating-up of material as it descends from the cooler concentrate layer to the warmer slag layer. This was achieved by incorporating

user defined functions (UDF's) into the solving algorithm of the model. The UDF's (presented in Appendix C) were programmed in C++ language to represent the heating-up of material in the slag as well as the concentrate layer while also including the heat of smelting in the concentrate layer.

The energy associated with the heating-up of material was determined through the change in enthalpy:

$$\Delta H = m \cdot c_p \cdot (T_{cell} - T_{ref}) \text{ [W]} \quad (5.1)$$

The mass-flow rate used for this calculation corresponds to the flow of material descending from the concentrate layer towards the slag and was taken as 8.23 kg/s, the feeding rate of the furnace. The material entering the slag-zone was assumed to be at an average temperature of 1523 K, which was taken as the reference temperature for estimating the change in enthalpy.

The heat of melting was determined by using the thermodynamic software Factsage 5.5 (2007) to calculate the enthalpy change occurring in a typical concentrate sample when heated from 800 °C to 1800 °C. This was performed for the three ore types commonly smelted by the electric furnace, i.e. Eastern and Western Platinum UG2 and Merensky ore. The simulation results for these ores are provided in Figure 4.3.1 and Figure 4.3.2. A common area of rapid enthalpy change is identified between 1200 and 1450 °C, indicated by the dashed lines.

From the above graphs it can be seen that the enthalpy transition occurs at a much lower enthalpy for the Merensky ore compared to the UG2 ore types which is presumed the result of the heat capacities of the different mineral compositions. However, the magnitude of change in enthalpy was calculated to be approximately the same with 85000 J/100g for Eastern Platinum, 92500 J/100g for Western Platinum and 90000 J/100g for the Merensky ore type. These heats of melting was averaged and multiplied with the feed-rate to the furnace to obtain a value that could be used to represent the smelting energy for the furnace model. An average power of 4.28 MW was determined.

To allocate the calculated smelting energy, distinctive smelting zones were identified within the concentrate layer and were assigned a portion of the smelting energy in proportion to the likelihood of smelting occurring within the particular zone. Eric and Hejja (1995) identified the active smelting areas within the furnace based on the liquidus temperature range for slag. These zones are depicted in Figure 4.3.3 below, obtained

from this study. A similar method was adopted in the previous CFD study on the furnace slag layer [Jones, M.T. 2004].

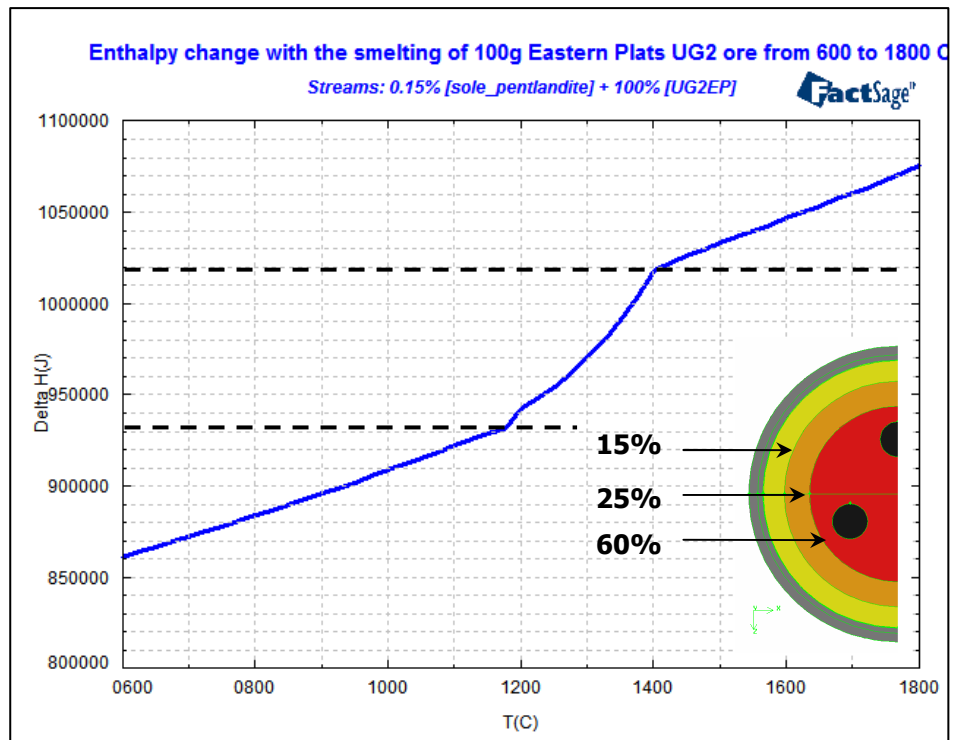


Figure 4.3.1 The enthalpy change observed in the concentrate during smelting as simulated by Factsage for Eastern Platinum ore type. Inserted - the allocation of smelting energy as percentages.

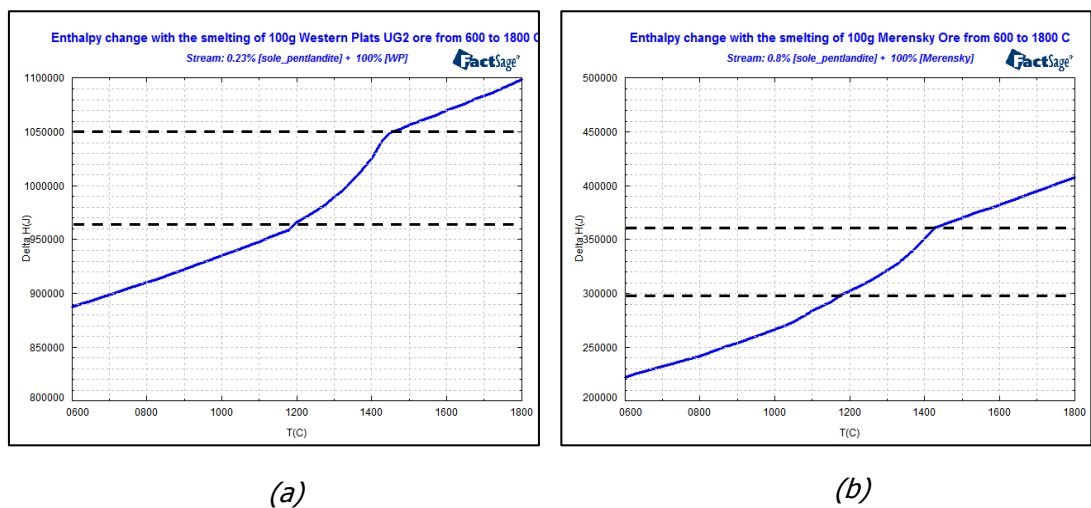
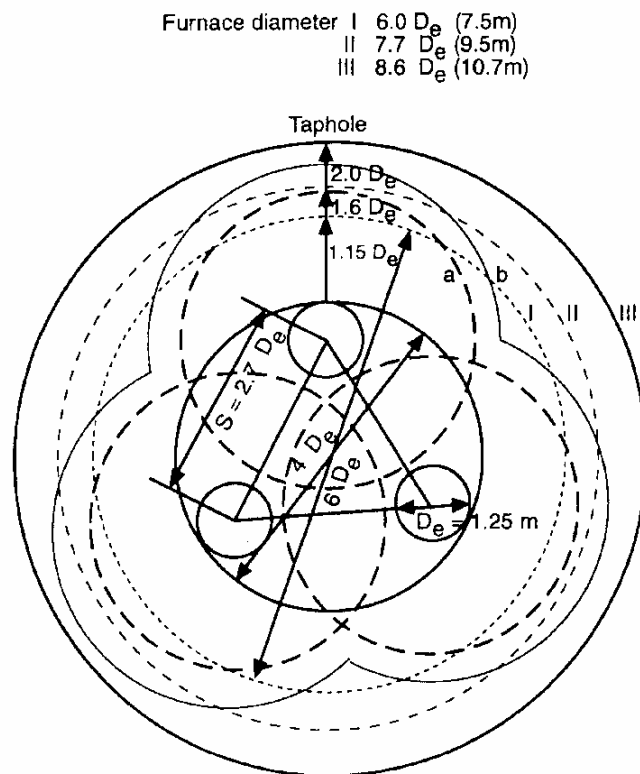


Figure 4.3.2 (a) and (b). The enthalpy change observed in the concentrate during smelting as simulated by Factsage for (a) Western Platinum and (a) Merensky ore type.

A specific 50 mm smelting zone was assumed on the boundary between the concentrate and slag layers and further radially subdivided into three zones, based on the recommended radial distances from the study by Eric and Hejja (1995). The boundary for the first active area was calculated at 3.5m from the furnace centreline. The boundary for the second active area was estimated at 4.5m to the centre of the furnace.



*Figure 4.3.3 The estimated active areas around the electrodes arranged in a delta configuration. Taken from the study by Eric and Hejja (1995)*

Numerous simulations were performed during the initial part of the model development to determine the most appropriate ratio of energy allocation to the smelting zones in order to obtain a realistic temperature gradient and to prevent an uneven energy distribution within the concentrate layer. The assumption was therefore made to allocate 30% of the total smelting energy to the thin 50mm layer and the remaining 70% to the rest of the concentrate volume (the region above the 50 mm layer towards the concentrate surface).

Energy allocation to the three radial volumes of the 50 mm smelting layer was assumed to be in a 65/25/15% ratio (as depicted in the insert of Figure 4.3.1). In this way an energy sink is allocated to the whole of the concentrate volume with the highest concentration of energy withdrawal at the concentrate-slag interface, however decreasing radially to imitate the occurrence of a radially variant smelting rate.

### 4.3.5 Power inputs

To facilitate the supply of a three-phase AC current to the furnace model, user defined functions (example presented in Appendix C) were written in C++ language to assign a sinusoidal current input to volume sources representing the three electrodes. To allow current in- and outflow, zero current density boundaries were set to the top of the electrode volumes, i.e. the cut-off surface from the upper-electrode. These UDF's were coupled to the time simulated by the furnace model.

The electrodes are usually connected to operate under a delta resistance configuration as illustrated by the insert of Figure 4.3.4. To enable a three-phase electrical current, it was assumed that the resistive load between electrodes are balanced such that input current would be equal in magnitude but lagging with  $120^\circ$ , as depicted in Figure 4.3.4.

The most important assumptions made during the modelling of the smelting furnace are considered to be the assumption of the current frequency. Due to the considerably smaller time-step and therefore increased simulation time required to model the actual 50Hz current supply an assumption had to be made to relieve the computational intensity. A frequency of 0.0167 Hz, relating to a minute period (shown in Figure 4.3.4), was found to be the most feasible operating conditions for meeting the modelling outcomes. The extent of this important assumption is discussed in Section 4.4.

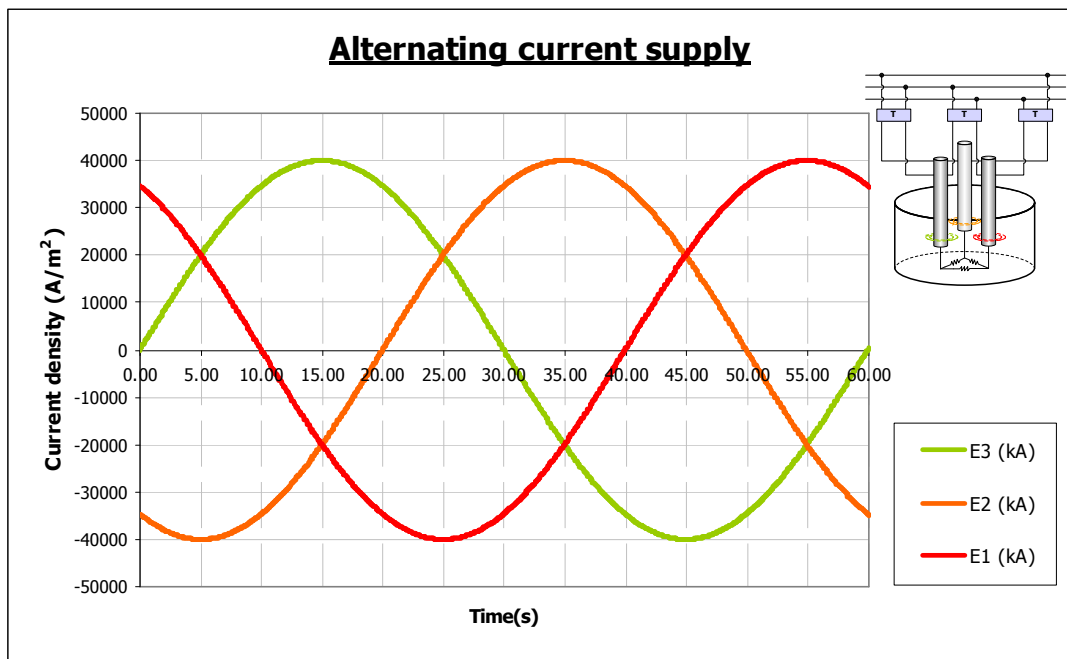


Figure 4.3.4 Graphical representation of the current supplied to each electrode. Insert: Schematic of the delta resistance arrangement as observed during smelting, adapted from [Dosa et al. 1996].

#### 4.3.6 Multiphase settings

It was decided to model the two-fluid system of the slag and matte and keep track of their interface by using the Volume of Fluid (VOF) multiphase model. The Discrete Phase model was selected for enabling the release and tracking of gas bubbles from the immersed electrode surface. The specifications for these multi-phase models are provided:

##### Volume of Fluid (VOF) multiphase model:

The volume of fluid model was enabled once the grid had successfully been interpreted and the UDF's compiled. The system was defined to contain two phases of which the slag layer was declared as the primary and the matte layer as the secondary phase. The Courant Number, a dimensionless number that compares the calculation time-step to the characteristic time for a fluid element to enter or leave a computational cell [Fluent manual], was set from the default of 0.25 to 1 as to allow solution stability during the initial iterations. An interfacial tension of 0.4 N/m, as determined in Appendix A, was specified to be present between the phases.

The development of a highly viscous sub-layer at the slag-matte interface due to the settling of chromite and magnetite deposits is taken into account in the final, complete model by introducing an additional phase to the current model as previously mentioned. This phase was positioned between the slag and matte phases and assigned to the volume created during the geometry assembly.

The CICSAM scheme was considered to be the most appropriate explicit interpolating scheme for calculating the interface between phases. Compared to the other available schemes, e.g. donor-acceptor and geo-reconstruct, the CICSAM scheme is less computationally expensive and provided more stability and a more uniform CPU load for the parallel simulation. The CICSAM scheme is specifically suitable for a system where a high viscosity ratio is present between phases, which are true for the current model where the difference between the slag and matte viscosity is of approximately second order [Fluent manual].

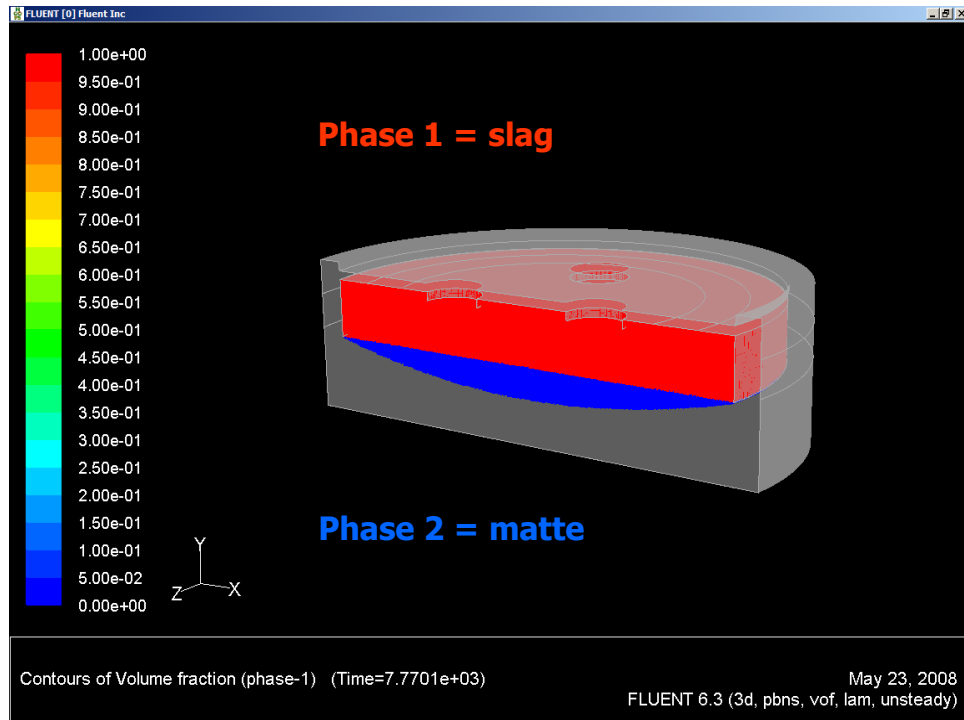
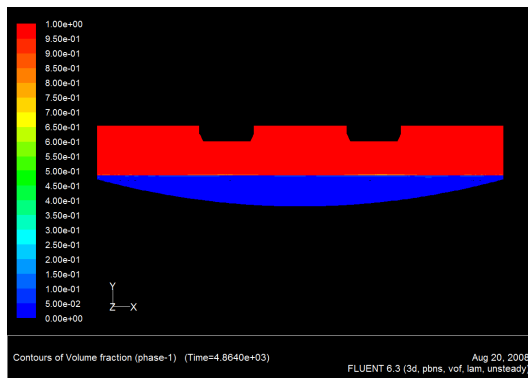
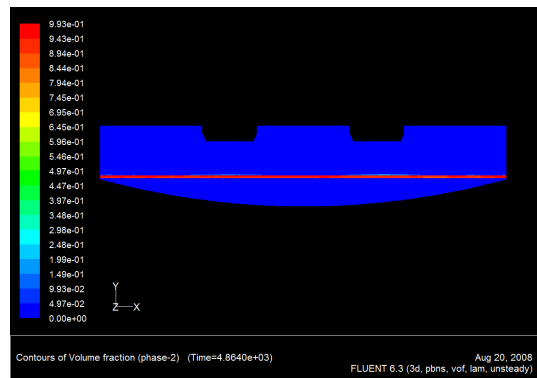


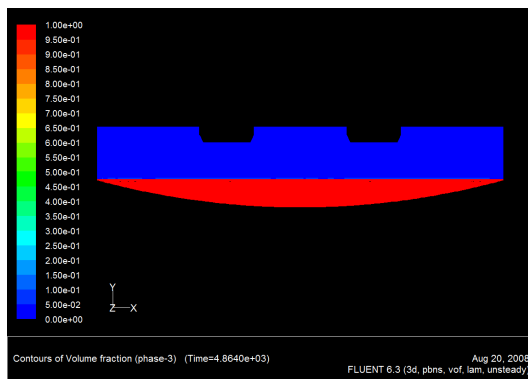
Figure 4.3.5 Depicting the particles (represented as point forces) released from the surface of electrode nr.3.



(a)



(b)



(c)

Figures 4.3.6 a, b and c. (a) Phase 1 allocated to the slag, (b) phase 2 allocated to the highly viscous intermediate slag layer and (c) phase 3 allocated to the matte layer.



Discrete Phase multiphase Model (DPM):

Three particle injections were enabled from the specified electrode surfaces immersed in the slag layer. The injection rate was calculated from the actual rate of electrode paste consumption, obtained from the smelting furnace operating data. The specifications of these injections are provided in the following table:

*Table 4.3.3 Summary of the specifications used for defining the particle injections.*

Description	Specification
Bubble composition	Inert CO <sub>2</sub> gas
Bubble diameter	1 cm (uniform spherical)
Initial velocity	0 m/s
Initial temperature	1850 K
Injection rate (per electrode)	0.0068 kg/s
Injection direction	Normal to the electrode surface

The discrete phase solver was set to allow coupling between the discrete and the continuous phases with the particle tracking being unsteady and DPM sources being updated with the fluid flow time-step. The DPM iteration was performed after 10 continuous phase iterations and the spherical drag law was enabled for including the frictional effects of the particles on the system and vice versa. The tracking parameters were left to their default values.

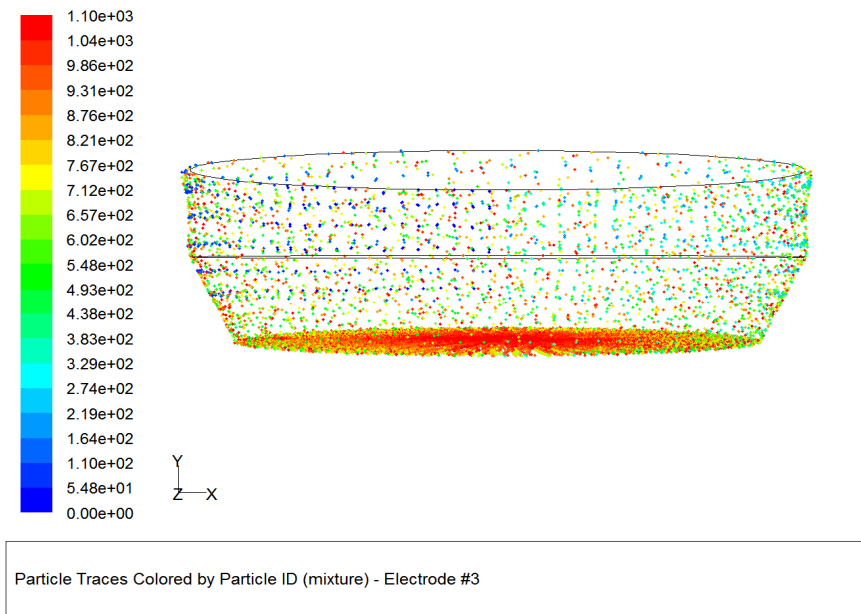


*Figure 4.3.7 Depicting the particles released from the surface of electrode nr.3.*

### 4.3.7 Magneto-hydrodynamic settings

The magneto-hydrodynamic (MHD) supplement for the Fluent solver was enabled after the UDF's had been compiled. As stated, the electrical potential method was chosen for modelling the current density throughout the domain and to allow the electrical current input to be specified through volume sources. Within the MHD set-up, the effect of the Joule heating was enabled and the upper boundaries of the electrodes were changed to conducting walls with a specified current density of 0 A/m<sup>2</sup> and the outer walls of the furnace hearth and copper cooler at ground potential (0 V).

### 4.3.8 Solver settings

The relatively small flow and thermal changes observed per time-step allowed the setting of high under-relaxation factors. The details regarding the solution controls for the furnace model are provided in Table 4.3.4 below. The PISO algorithm was selected to perform the pressure velocity coupling due to its robustness and suitability for transient flows, as discussed in Section 3.4.

The solution was initialized at 1800K and the default values for the other variables were used. The temperatures for the matte and hearth were however patched to 1700 K and 900 K respectively to promote the development of the temperature profiles. The volume fraction for the matte layer was patched to be fully occupied by the secondary phase.

*Table 4.3.4 Summary of the FLUENT solution controls for the furnace model.*

Under-Relaxation		Discretization		Convergence Criteria	
Pressure	0.3	Pressure	PRESTO!	Continuity	0.001
Density	1	P-V-C	PISO	X-velocity	0.001
Body Forces	1	Momentum	1 <sup>st</sup> O-U	Y-velocity	0.001
Momentum	0.7	Volume Fraction	CICSAM	Z-velocity	0.001
Energy	1	Energy	1 <sup>st</sup> O-U	Energy	1e-06
Electric Potential	1	Electric Potential	1 <sup>st</sup> O-U	Electric Potential	1e-09
D-P-S	0.5				

A conservatively small time-step size, 0.0625 s, was chosen for the initial 10 iterations to prevent instability resulting from initial high residuals. Once a stable simulation was obtained, the time-step size was increased to 0.25 s, which is considered to be a small enough time advancement for capturing the character of a smooth sinusoidal current input as specified by the current input UDF's. Ten iterations per time-step were found to

be adequate for allowing the current to diffuse through the model domain and to solve the model equations until the residuals were sufficiently reduced below the set convergence criteria.

## 4.4 Model assumptions

---

Due to the complexity of the electric furnace model, important assumptions and simplifications were required to make modelling feasible. These assumptions are discussed in this section through the identification of their effect on the model prediction and by validating their application. The assumption of the absence of an induced magnetic field relating to Ampère's law has been discussed in Chapter 3.

### 4.4.1 Reducing the current frequency

The actual 50Hz (0.02s period) current frequency is approximated by a reduced frequency of 0.0167Hz (1 minute period) to avoid a very small time-step in the transient simulation and to enhance the establishment of a steady-state solution.

**Effect:** The longer power cycle could lead to coupled variations in the model variables with time.

**Justification:** Trends of temperature as well as the velocity in the slag layer showed small peaks in the maximum values, as depicted in Figure 4.4.1, while no variation in the average values were observed. These peaks are less than 1% of the maximum and therefore the influence of a reduced current frequency is considered negligible. Similar trends in the matte process variables were obtained. The large volumes of the slag and matte are considered to damp the frequency response, therefore allowing minimal changes in the process character.

No influence of frequency on magnetohydrodynamic mixing is expected since the current computational model is incapable of including the induced magnetic fields. A study by Cloudhary *et al.* (1981) investigated the effect of assuming a constant electrical conductivity in the mathematical modelling of the electroslag refining furnace. It was concluded from the study that frequency effects brought about by the AC character does not affect current transfer and the electromagnetic force field in the slag. This is affirmed by the small magnetic Reynolds number determined previously.

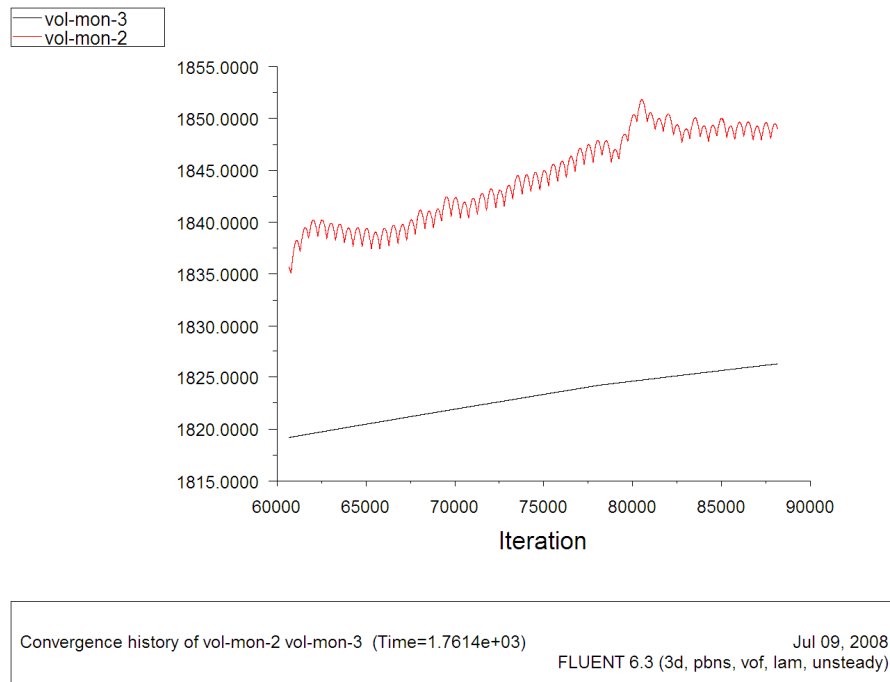


*Figure 4.4.1 Depicting variation in the maximum and average temperature of the slag due when applying a 0.0167Hz current frequency.*

#### **4.4.2 Neglecting slag and matte tapping**

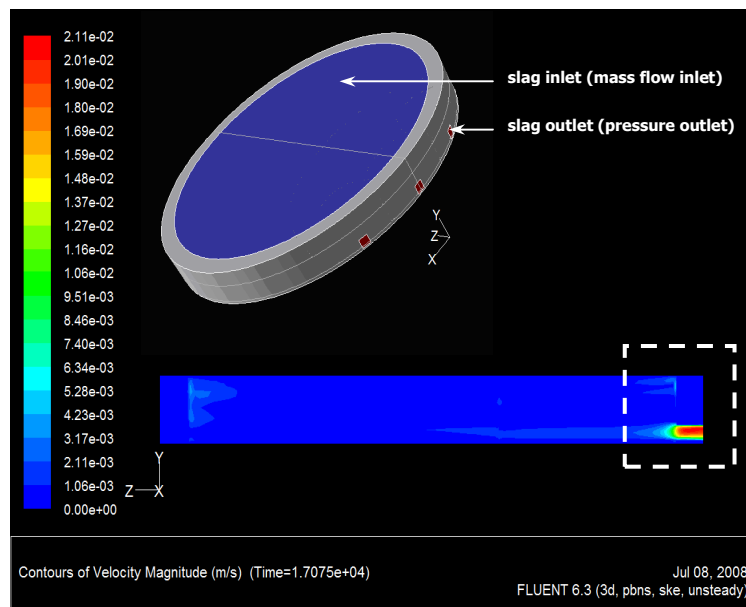
It was stated that the slag layer is almost continuously and the matte layer less regularly tapped from the furnace. The modelling of a dynamic multi-phase system is considered too complex and for this reason the tapping of the material layers was neglected in the current model.

**Effect:** Excluding the effects of tapping will result in an under-prediction of the energy output from the model while the flow of material through the top-hole could result in a different flow pattern and temperature profile within the material layers and furnace hearth in the immediate vicinity of the tap-holes.

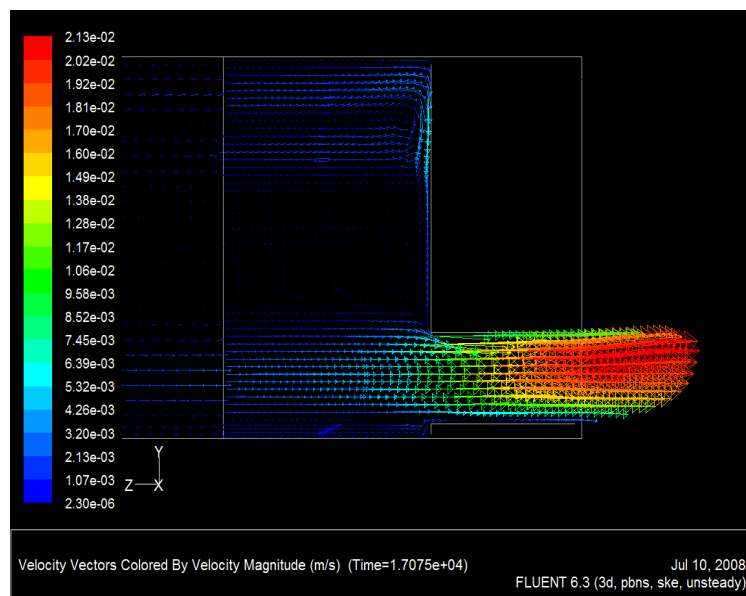
**Justification:** The additional heat loss associated with the tapped material is not compensated in the current model but a slight overestimation of the accumulated energy within the system is shown by the energy balance presented in Chapter 5, therefore allowing a contingency for heat-losses not taken into account.

To investigate the effect of tapping on the velocity profiles within the model, a small transient CFD model, Figure 4.4.2, was created for the slag layer that included a mass-flow inlet boundary for representing the inflow of fresh material at the top and outflow

boundaries at the outlets of three tap-holes created in the furnace sidewall as found at the front of the actual furnace. A model was only created for the slag layer since its tapping occurs almost continuously compared to the less frequent tapping times of the matte layer. This model did not include thermal effects but merely investigated the flow profile brought about by descending and exiting slag. Shown below are the velocity contour and vector profiles obtained for the slag model.



(a)



(b)

Figure 4.4.2 CFD model of the slag layer allowing in and outflow to investigate the effect of tapping (a) contour profiles and (b) vector profiles.

The effect of tapping is seen to be present only in the immediate vicinity of the tap-hole and does not affect bulk slag flow. The velocity magnitude of descending material in the bulk of the slag is shown to be very small. Compared to the velocity profiles and velocity magnitude brought about by natural convection as presented in Chapter 5, the effect of descending material on the slag velocity is therefore considered negligible.

#### **4.4.3 Constant matte and slag conductivity**

A constant slag and matte electrical conductivity was assumed in order to prevent model instability. A temperature dependant electrical conductivity would cause simulation instability since a temperature increase will result in the lowering of the electrical conductivity and therefore allow more power to be generated in the molten bath and hence completing the cycle by again increasing the temperature, as reported by Sheng *et al.* (1998). Retaining a constant resistive heat in the melt will also be difficult to obtain when using a variable electrical conductivity.

**Effect:** A temperature dependant slag and matte electrical conductivity may modify the electromagnetic force field and heat generation patterns in the electric furnace [Cloudhary 1981].

**Justification:** The study by Cloudhary *et al.* (1981), referred in Assumption 4.4.1, concluded that more pronounced Joule heating was found near the electrodes therefore giving higher local temperatures when including a temperature dependant electrical conductivity. However the difference between the maximum temperatures found for the case with and without a temperature dependant electrical conductivity amounted to 25K, which for the current model is considered negligible. The application of an average electrical conductivity is therefore considered acceptable for modelling of the full scale electric furnace.

#### **4.4.4 Neglecting furnace freeboard and roof**

The furnace freeboard and roof were not considered in the computational domain in order to reduce the computational burden of the model.

**Effect:** Convection heat losses from developing and exiting off-gas will result in an additional heat loss by the furnace and in turn, irradiation from the furnace roof back to the bath will retain an amount of heat in the system.

**Justification:** According to the project objectives, more value is placed on the information obtained from modelling the furnace bath than from knowing the dynamics at play in the furnace freeboard. However the effect on the energy balance is compensated for by applying a convection coefficient at the top of the concentrate layer for representing the typical “black top” temperature mentioned previously.

#### **4.4.5 Assigning smelting zones**

Distinctive smelting zones are assumed within the concentrate layer for allocating the heat associated with the melting of concentrate.

**Effect:** Distinctive smelting zones could under- or over-predict the occurrence of melting and may result in an inaccurate temperature distribution within the concentrate layer.

**Justification:** Point-allocation of the melting energy in areas where the melting temperature has been reached will result in a sudden high local withdrawal of energy that will lead to an unstable and inordinate temperature distribution. For this reason the melting energy is allocated to whole volumes at a time with the highest energy withdrawal where smelting is expected to be the most intense. Smelting zones are considered appropriate for deriving an approximate idea of the smelting behaviour in the concentrate layer.

#### **4.4.6 Neglecting radiation effects**

To prevent the use of a radiation model and so reduce computational expense, radiation from the top of the concentrate layer was neglected.

**Effect:** The heat loss from the furnace will be under-predicted.

**Justification:** As stated in Assumption 4.4.4, compensation for the heat loss by radiation from the concentrate top is made by the adapted convection heat transfer coefficient.

#### **4.4.7 Neglecting turbulence effects**

The effects of turbulence were completely neglected in the final furnace model.

**Effect:** The velocity brought about by the bubble formation at the immersed electrode tips could result in swirling motion at the top of the slag layer which would not be captured by the laminar flow model.

**Justification:** The effect of including a turbulence model was investigated and a severe over-prediction of flow within the slag and matte layers was obtained. This resulted in inappropriate temperature distribution within these layers as will be discussed later. Further discussion on the inclusion of the turbulence model is provided in Chapter 5. The majority of the flow within the slag and matte is however considered to be laminar. This assumption is validated through evaluation of the criteria for the transition between the laminar to turbulent free convection boundary layer, known as the Rayleigh number (Ra):

$$Ra = Gr \cdot Pr \quad (5.1)$$

Ra was found to be between  $1.63 \times 10^6$  and  $1.98 \times 10^7$  for the expected temperature range of 1327 and 1727°C in the slag layer. The Rayleigh number is therefore lower than the transition criteria,  $1 \times 10^9$ , for turbulent flow [Incropera and De Wit 2002]. The details of this calculation are shown in Appendix B. Predominant laminar flow was also estimated for slag flow in a rectangular electric smelting furnace by Hejja and Eric (1996).

The future version of FLUENT, Fluent 12, is reported to contain models capable of modelling the transition between laminar and turbulent regions. This version was not available when the current modelling was commenced.

#### 4.4.8 Point-force representation of particles

Simplifications are made in the numerical compilation of the multi-phase models used by the furnace model. Of the most important are the assumption of negligible particle volume through the point-force Lagrangian approach and linear reconstruction of the interface between liquids.

**Effect:** Particles having no volume could under-predict the viscous stress on the system [Patankar 1960].

**Justification:** For the current system, the volume occupied by the particles is small when compared to the slag surrounding them. The volume of the particles is therefore not considered to have an impact on the effective viscosity of the slag in the region where the particles are released. Also, the interface between the slag and matte is expected to remain flat and fairly stagnant, making a linear reconstruction scheme feasible.



#### 4.4.9 Additional neglected heat-losses

A collection of heat-losses were not compensated for in the current furnace model. These include neglecting of the heat associated with arcing from the electrodes and chemical reactions.

**Effect:** These neglected heat-losses will result in an under-prediction of the heat-output from the furnace model.

**Justification:** The phenomenon of arcing at the electrode tips is thus far not completely understood and approximation thereof will still require an intensified modelling approach which is not currently feasible. However, the heat associated with chemical reactions in the molten bath has however been reported to be less than 1% of the total heat supplied to the furnace. This was determined by a thermodynamical survey based on typical platinum concentrates as processed by the electric smelting furnace [Confidential study 2006].

#### 4.4.10 Approximation to the furnace refractory

The exact construction of the hearth and sidewall has not been modelled due to difficulty in creating and especially meshing the actual furnace geometry. An approximation to the actual refractory is made by the two volumes comprising the furnace hearth as previously stated.

**Effect:** The hearth and bottom sidewall composition used for the current furnace model will result in a possible over-prediction of the actual hearth and sidewall outer temperatures due to the absence of important thermal insulating refractory layers.

**Justification:** A compensation for the adjusted refractory is made by altering the thermal conductivity of the two layer refractory created for the current model along with the convection heat transfer coefficient from the surface to maintain the heat-loss from outer walls according to the furnace energy balance.

### 4.5 Processing system specifications

---

The Metis partition method was applied to equally partition the computational grid in the most efficient way to minimize the number of partition interfaces and number of partition neighbours [Fluent manual]. The algorithm used by the Metis method combines edges and vertices to form

a coarser computational grid that is partitioned before being converted back to the original grid. The resulting partition is illustrated in Figure 4.5.1.

The large computational extent of the furnace model required the need for parallel processing. An eight node system (4 PC's having dual core processors) was applied to process the simulations. Load distribution was performed prior to the model set-up due to the processors differing in computational speed. Three nodes were equipped with 3.3 GHz processing power while the host computer contained 1.8 GHz processors. For this reason, twice the computational cells were allocated to the faster computers.

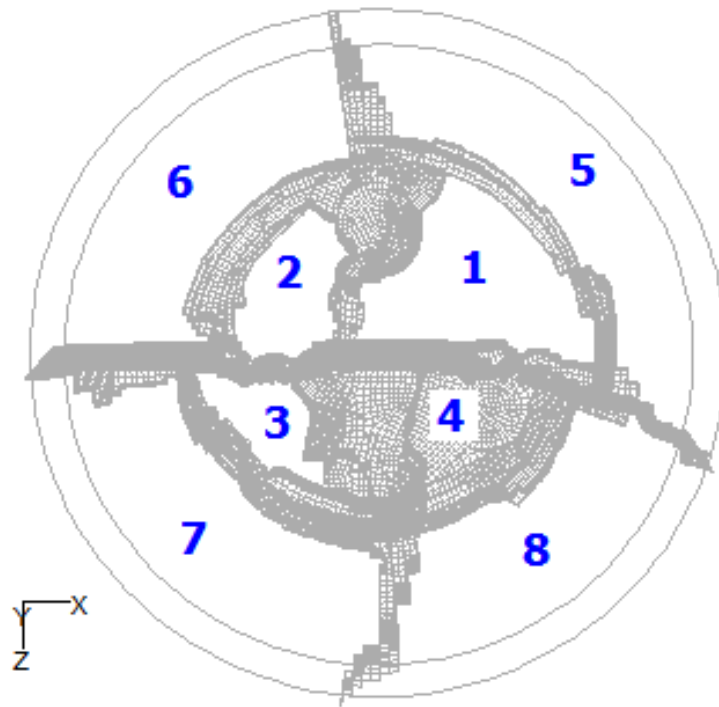


*Figure 4.5.1 Depicting the partitioned computational domain as partitioned through the Metis method.*

## 4.6 Monitoring solution convergence

Since this is a transient simulation model, a point of simulation termination is required. As stated previously, the model variables showed different time-scales of convergence after which no further change was observed as time progressed. This time-scale is approximately instantaneous for the electrical related variables (current density, electric potential and therefore Joule heat) while being considerably long for velocity and temperature. It was decided to monitor the average temperature distribution within the slag layer as an indication of model convergence since approximately all model influences originate within the slag layer. A converged velocity distribution, being influenced only by buoyancy since the effect of bubble momentum remains constant for each time-step, is presumed to follow the converged temperature solution.

Figure 4.6.1 shows the monitor that was kept on the average temperature within the slag for the model without CO-bubble formation at the electrode and it can be deduced that no significant change is expected beyond this point of approximately 7700 seconds. The change in the average temperature gradient (at iteration 312500) was brought about by an increase in the slag electrical conductivity after it was found that the resistive power input to the model was slightly over estimated.

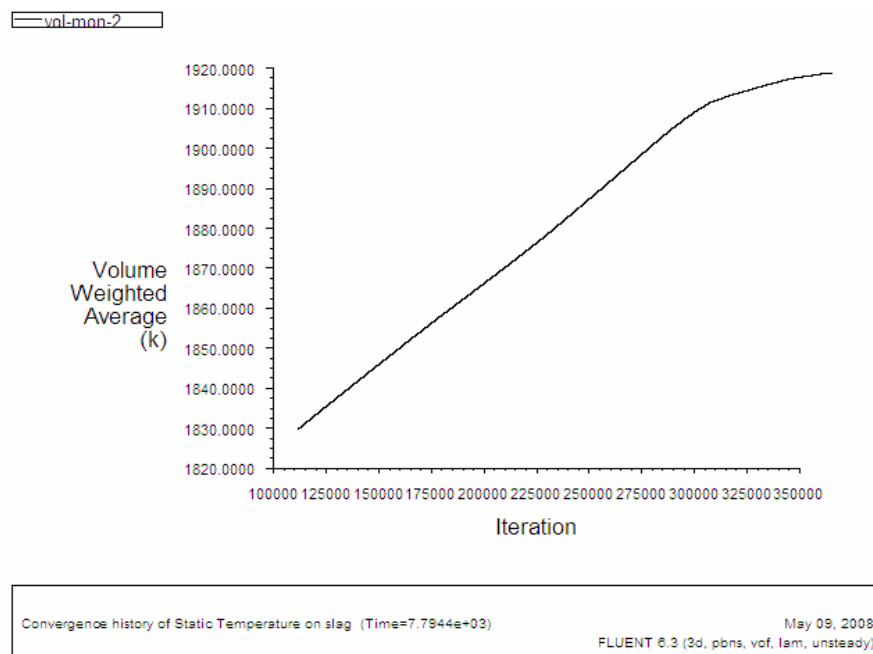
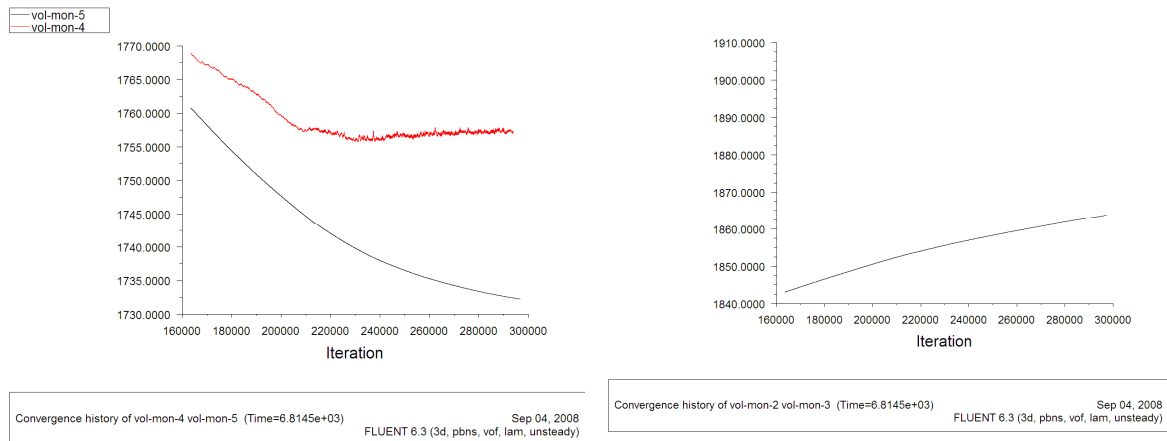


Figure 4.6.1 The monitor on the average temperature within the slag layer as an indication of model convergence for the model without CO-bubble release from the surface.

Figures 4.6.2 present the temperature monitors on the matte and slag for the model where CO-bubbles were released from the electrode surface, showing the trends in the average temperature (black lines) to have tapered-off sufficiently such that no further changes above 5% is expected. The time 6814 seconds required approximately 12 weeks of real simulation time.



*Figure 4.6.2 The monitor on (a) the average and maximum temperature within the matte layer and (b) the average temperature within the slag for the model with CO-bubble release from the surface of the electrodes.*

---

# CHAPTER 5

## RESULTS AND DISCUSSION

---

The modelling of the electric furnace led to a series of investigations of which the results are presented in this chapter. A converged solution was obtained for two models that incorporated a 35% electrode immersion. The first complete model only considered the effect of natural buoyancy to induce flow within the slag. A later model included CO-gas bubbles released from the immersed electrode surfaces and also a third phase of high viscosity between the slag and matte layers as previously discussed. The relatively smaller convergence time-scale required for current density and the subsequent electric potential and Joule-heat distributions allowed the investigation into the related effects of electrode immersion.

The converged solution of the various models was post-processed to allow simple interpretation of the results. The results are presented by means of contour and vector plots of the model variables for providing a qualitative analysis while computed integrals and variable trends allowed a more comprehensive visualization of the furnace model. As stated, validation for the furnace model is limited. However to provide means of evaluating the model's capability, the results are compared to previous studies (that include measurements) and the actual furnace temperature and power operating range.

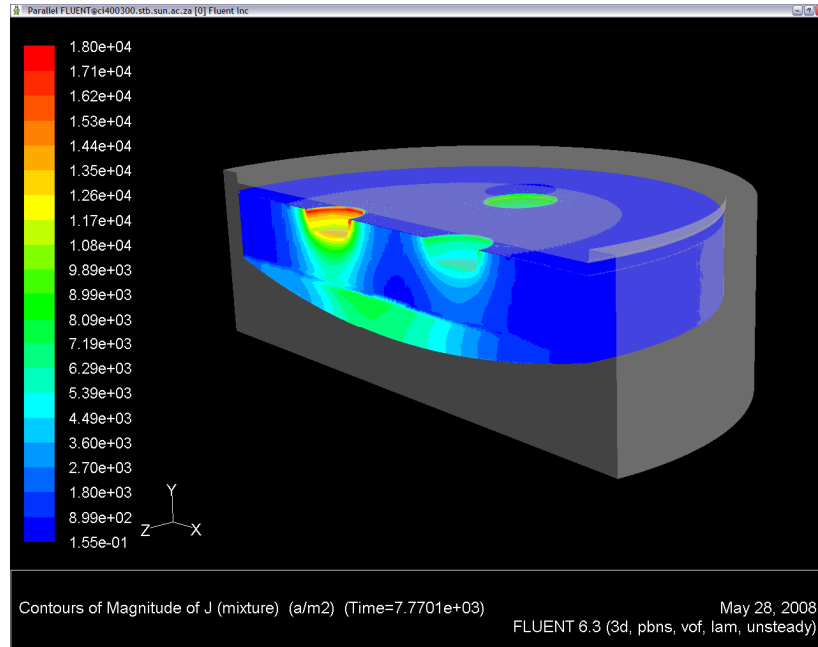
### 5.1 Current density distribution

---

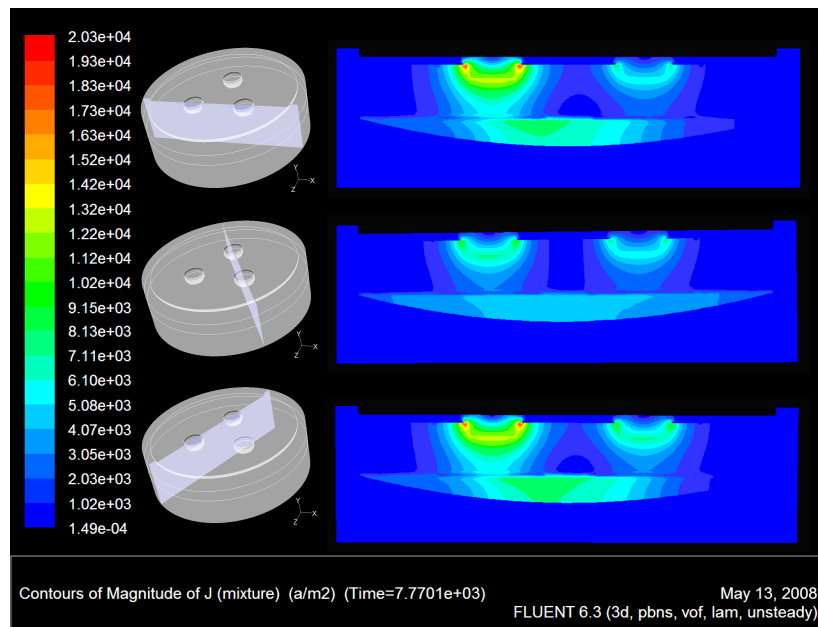
#### 5.1.1 Current flow path

The current path predicted by the furnace model compares very well with the accounts mentioned in literature. The current is seen (Figure 5.1.1 below) to flow vertically through the slag layer into the matte layer where flow is predominantly horizontal. The current

therefore finds the path of least resistance from the supplying electrode towards the more conductive matte layer where the current flows through the matte and up through the slag again towards the receiving electrode.

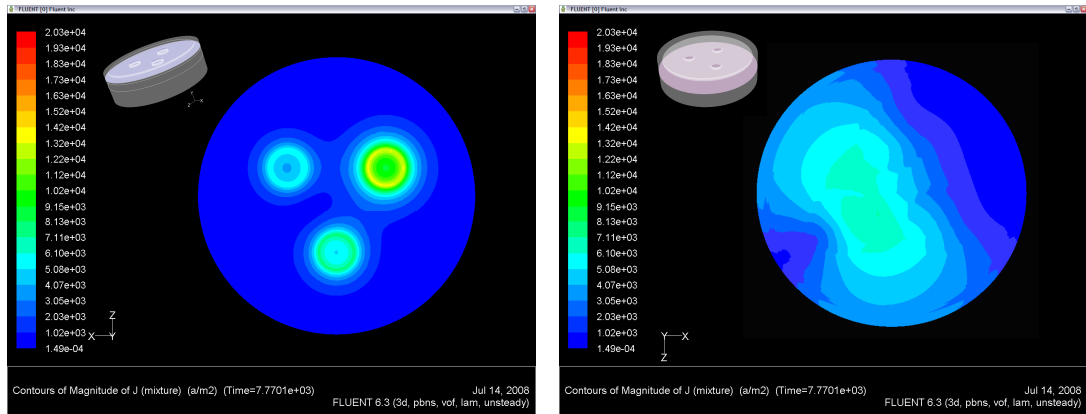


(a)



(b)

Figure 5.1.1 Current density ( $A/m^2$ ) profiles obtained for the base case furnace model. (a) Three dimensional contour of the current density (b) Two dimensional profiles along different vertical cross-sections passing through the electrodes.



(a)

(b)

Figure 5.1.2 (a) Current density profiles on a horizontal section within the slag layer through the electrodes. (b) Current density profiles on a horizontal section within the upper matte layer.

A percentage of 75.96 % of the current observed at the electrodes to that observed just above the matte layer for the electrode immersion of 35 %. This was calculated by intergrading the current density on horizontal surfaces at the center of the electrodes and at the slag-matte interface. This percentage is in good agreement with the results by Urquhart *et al.* (1976) and Barth (1960), who reported that two thirds to three quarters of the total current flow to flow via the matte between the electrodes.

### 5.1.2 The mode of current flow

A rapid radial decrease in the current density within the immediate vicinity of the electrodes is observed. Eric and Hejja (1995) suggested with uncertainty the current path at the electrode tips to take the form of either a rotational paraboloid or hyperboloid. The current density vector plot provided in Figure 5.1.4 below however does allow clear characterization of the mode of current flow around the electrode tips.

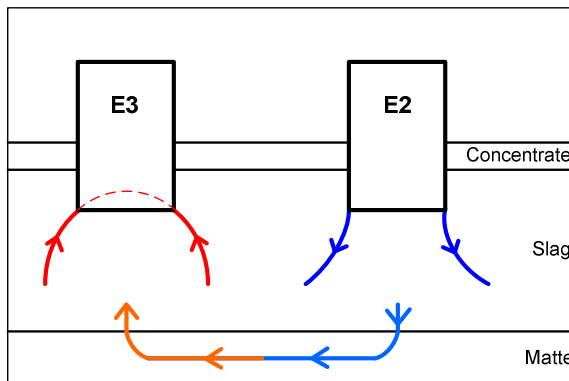
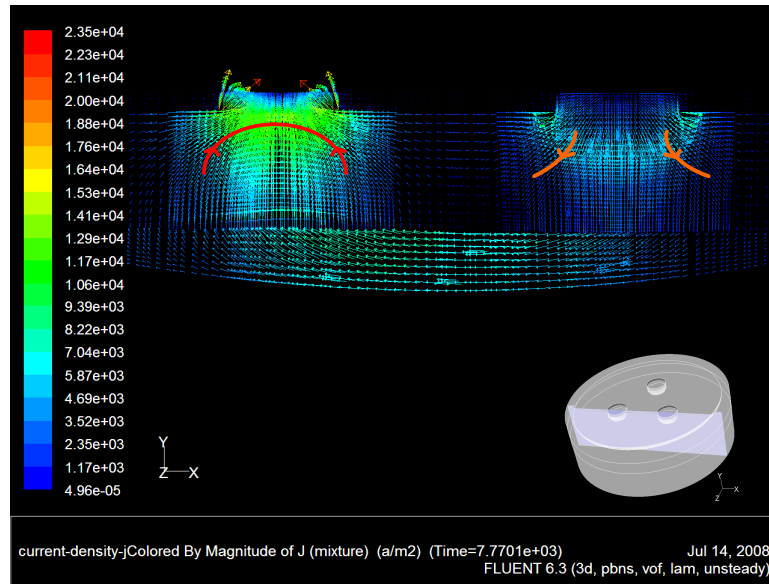


Figure 5.1.3 Schematic representation of the mode of current flow as observed from the vector plot in Figure 5.1.4, showing hyperbolic current flow at the input and parabolic current flow at the output electrode.

The current is seen to flow hyperbolically from the supplying electrode into the matte layer while the current flow towards the receiving electrode is parabolic, therefore suggesting both forms of current flow to be present in the furnace system depending on the moment in time along the AC current supply cycle.



*Figure 5.1.4 The vector distribution of current density along a vertical cross-section passing through the front two electrodes. At this point in time the electrode on the left is receiving current while the right-hand electrode is at a low stage of current input. The back electrode, not displayed, will be at a higher current input stage according to the sinusoidal current function.*

### 5.1.3 The effect of electrode immersions on current flow

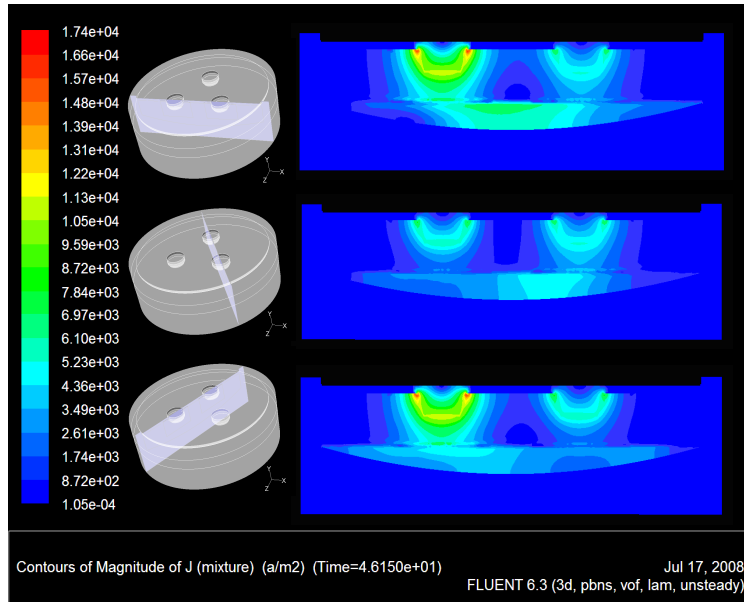
It is seen that the deeper electrode immersion, i.e. 55 %, concentrates the current-flow closer to the matte layer. Very little current flow is observed for the 15 % electrode immersion model where approximately half of the current is seen to pass between the electrodes. This was again determined by comparing the integrated current density along horizontal surfaces at the electrode centers and at the slag-matte interface.

This can be seen by comparing Figures 5.1.7 and 5.1.8 where a higher concentration of current flow is observed between the electrodes for the 15 % electrode immersion model. This is the result of higher path resistance brought about by the shallower electrode immersion. A comparison of the percentage of current-flow observed at the electrodes to the current-flow observed at the slag-matte interface for the different immersion models is presented in Table 5.1.1 below.

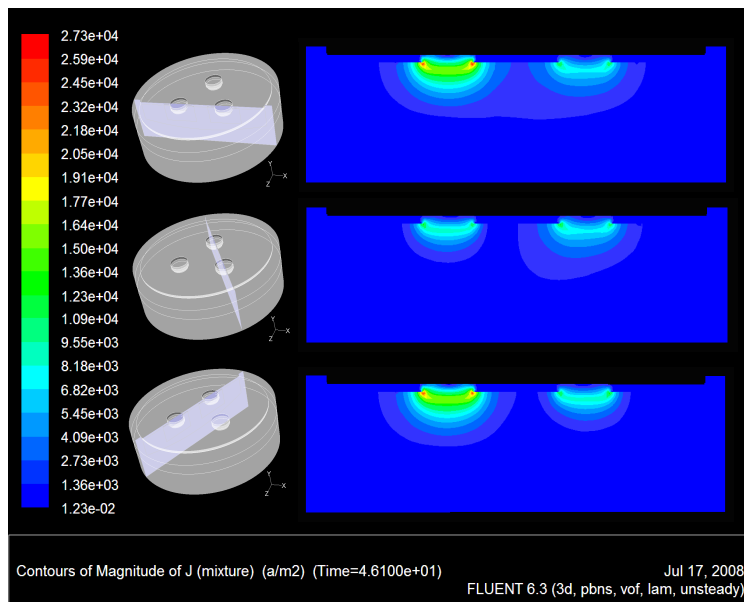


Table 5.1.1 Comparing of flow of current for different electrode immersions.

Electrode immersion	55 %	35 %	15 %
Integrated current at the electrodes centers to that at the slag-matte interface	81.11	75.96	45.70

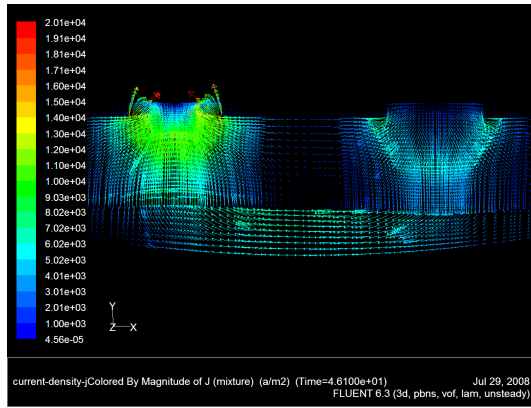


(a)

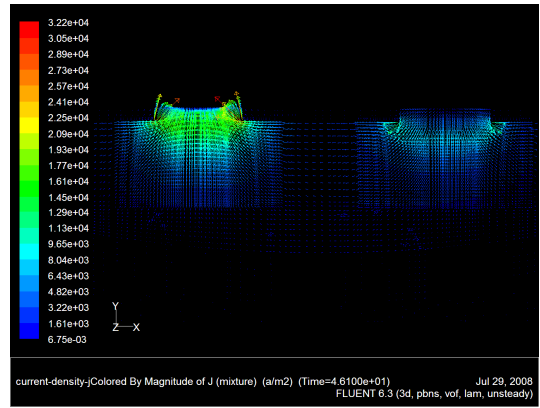


(b)

Figure 5.1.5 Two dimensional profiles of current density along different vertical cross-sections passing through the electrodes. (a) 55 % electrode immersion. (b) 15% electrode immersion.



(a)



(b)

Figure 5.1.6 The vector distribution of current density along a vertical cross-section passing through the front two electrodes (a) 55 % electrode immersion. (b) 15 % electrode immersion.

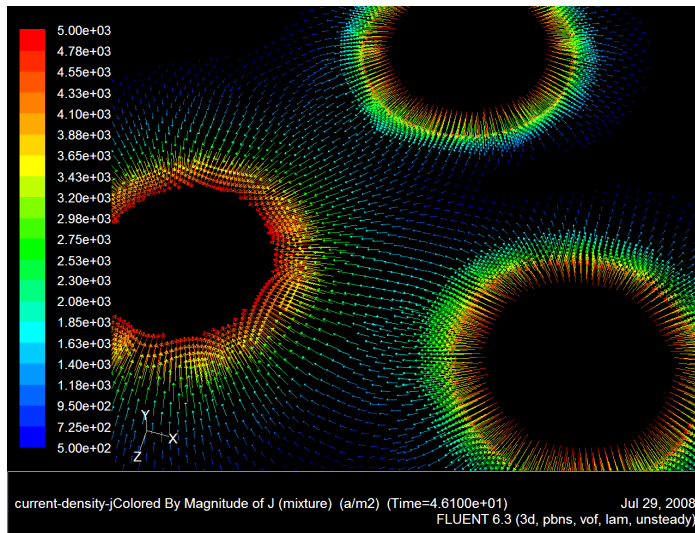


Figure 5.1.7 The vector distribution of current density along a horizontal cross-section passing through the centre of the electrodes for the 55% electrode immersion furnace model.

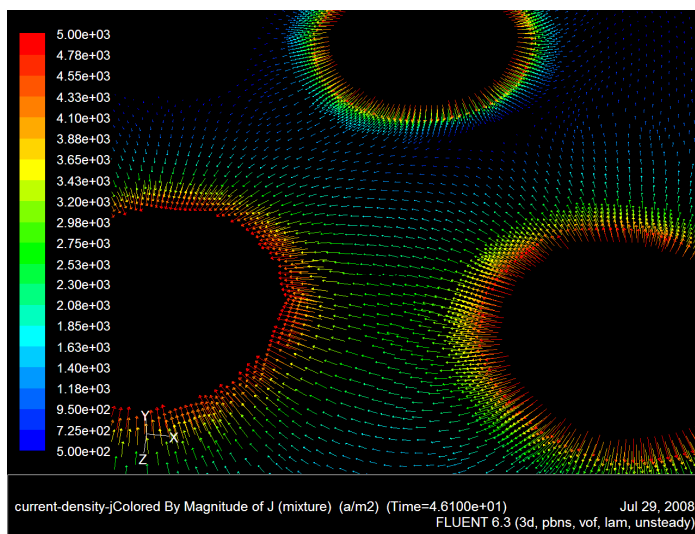


Figure 5.1.8 The vector distribution of current density along a horizontal cross-section passing through the centre of the electrodes for the 15% electrode immersion furnace model.

#### 5.1.4 The effect of electrode immersion on the required slag electrical conductivity

It is shown in Figure 5.1.9 below that the electrical conductivity of the slag required for maintaining a constant heat release within the bath increases with a decrease in electrode immersion. This is due to the fact that the slag electrical resistance increases with lower electrode immersion, as discussed in Chapter 2, which requires a higher slag electrical conductivity to be specified in the CFD model-setup for maintaining the resistance level within the slag, according to the energy balance. On the actual furnace this process will be in reverse order. A change in concentrate composition would bring about a variation in the slag electrical conductivity which in turn would result in the electrode depth being varied by the furnace control system to maintain the slag resistance. These findings are in agreement with those presented by Sheng et al. (1998).

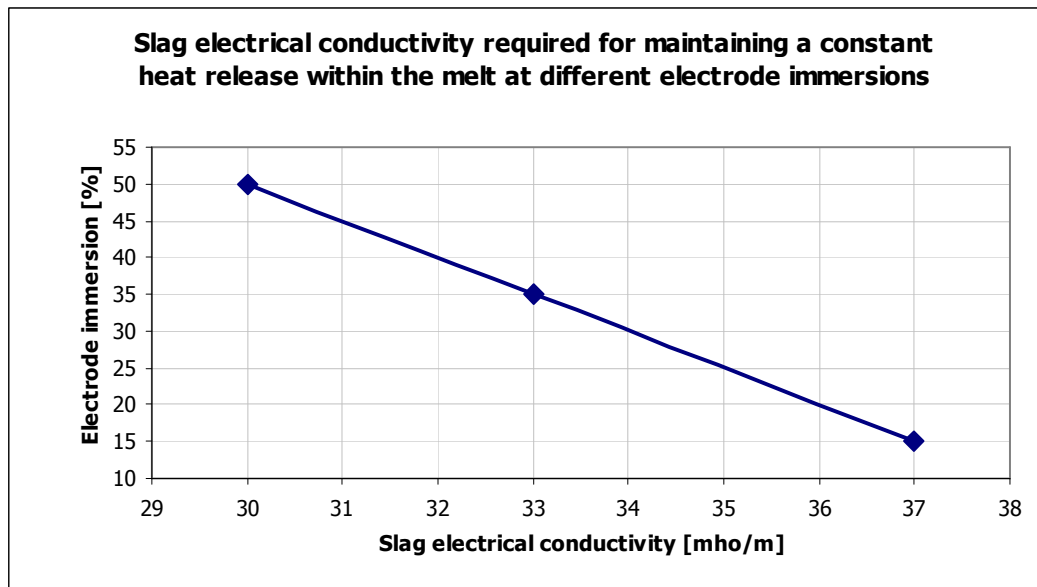
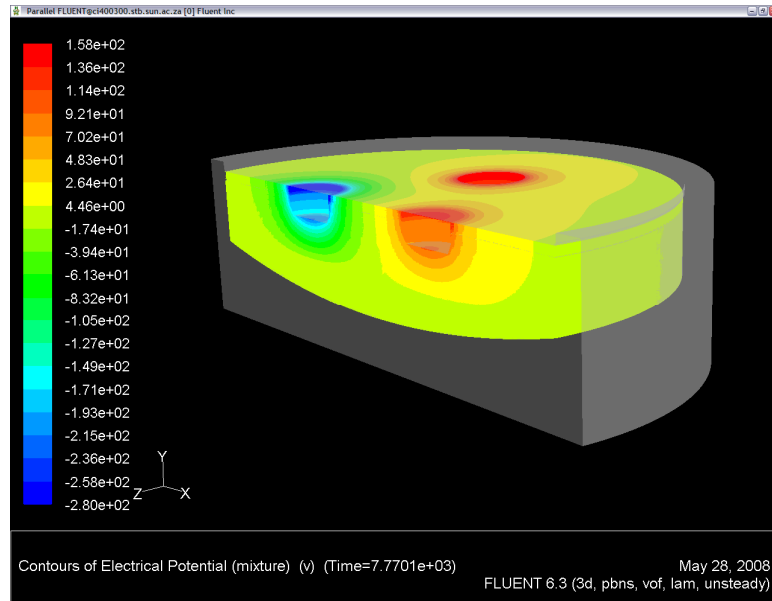


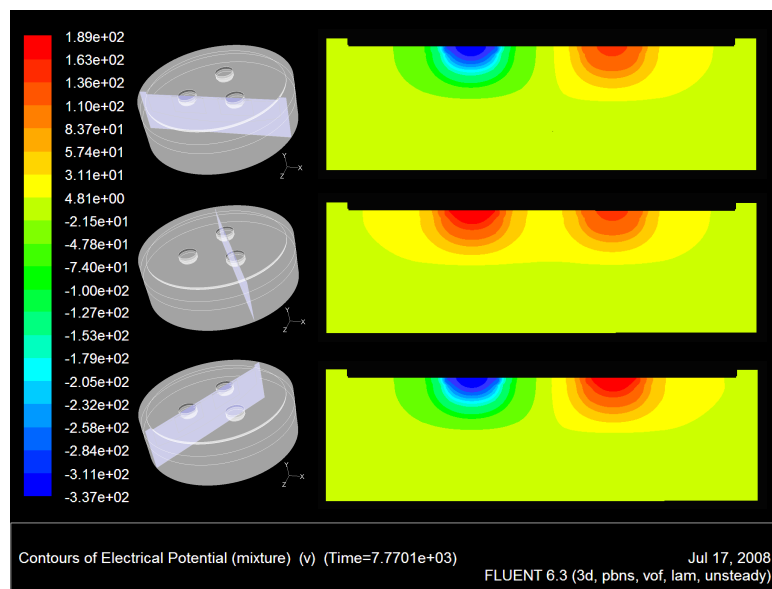
Figure 5.1.9 A comparison of the Required electrical conductivity to maintain the predetermined 11MW resistive heat within the slag layer for the different electrode immersions.

## 5.2 Electric potential distribution

The electric potential distribution obtained for the furnace model is provided in Figure 5.2.1 below. The electric potential trends are seen to follow the current density distributions presented previously. The three-phase current input is portrayed by the electric potential contours, showing the two electrodes on the right to be at a current input stage and the electrode furthest to the left to be receiving current.



(a)



(b)

Figure 5.2.1 Electric potential (V) profiles obtained for the 35 % electrode immersion model. (a) Three dimensional contour of electrical potential. (b) Two dimensional profile along different vertical cross-sections passing through the electrodes.

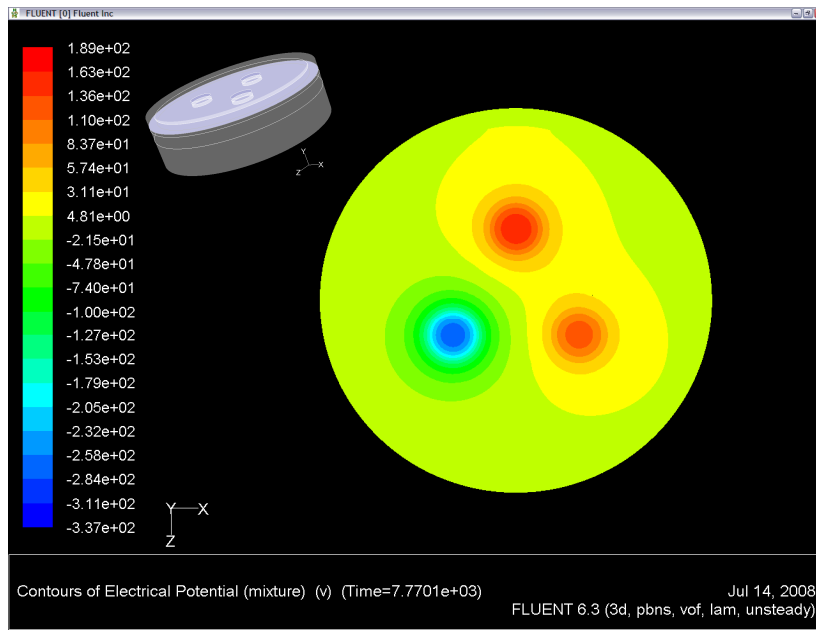


Figure 5.2.2 Electric potential (V) profiles obtained for the 35% electrode immersion model along a horizontal cross-section through the upper part of the slag layer.

A sharp radial decrease, as seen in Figure 5.2.3, in the electric potential is observed that is distributed almost spherically around the electrodes. The voltage range obtained at the electrode tips are close to the actual operating voltage, 280-320 V, observed on the furnace and correspond well to the expected voltage associated with the 11 MW resistive heating within the slag bath ( $P = IV$ ).

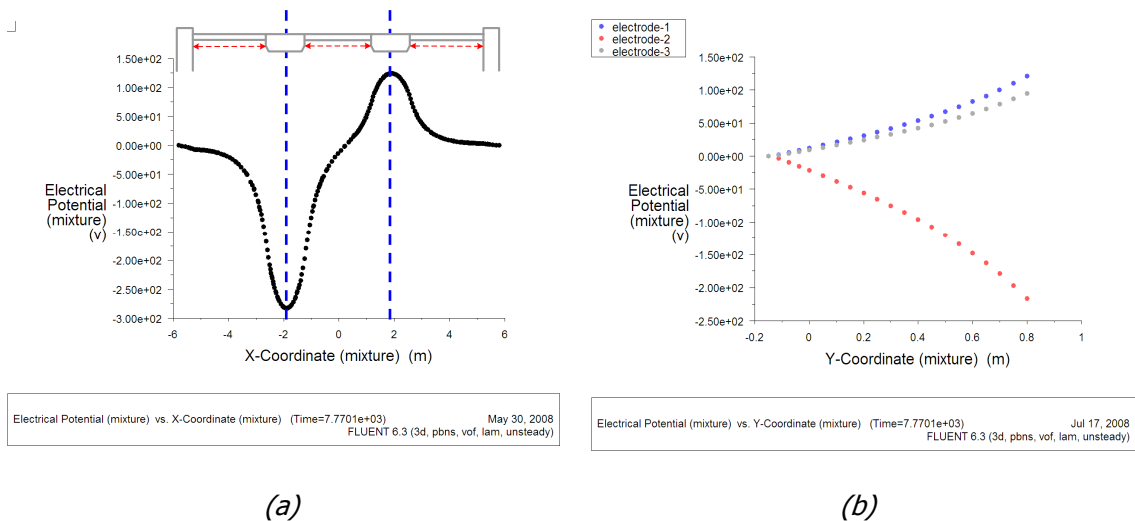


Figure 5.2.3 Electric potential (V) trends for the 35 % electrode immersion model (a) Electric potential distribution measured along a horizontal line through the front two electrodes of the

furnace. (b) Electric potential trend measured from the slag-matte interface towards the tip of the electrodes.

No electric potential gradients are observed to be present in the matte layer throughout the three-phase current cycle but are mostly concentrated in the slag and concentrate layers. An induced EMF, which could lead to a possible change in the magnetic flux according to Faraday's law, Equation 3.11, and hence induce Lorentz forces, is therefore considered unlikely in the matte layer. The assumption of neglecting an induced magnetic field is hereby justified.

### 5.3 Energy balance and power distribution

Attention was paid throughout the simulation process to the heat generated in the slag through resistive heat in order to obtain a balanced energy load on the furnace model. The transient nature of the furnace model revealed an accumulation of energy within the model system after the overall energy outputs have been deducted from the 22 MW electrical power input. The accumulated energy is identified as the required resistive heat that needs to be maintained within the molten bath to keep the furnace at a steady temperature. The energy-balance presented here is for the complete model, i.e. the 35 % electrode immersion with CO-gas forming at the immersed electrode tips.

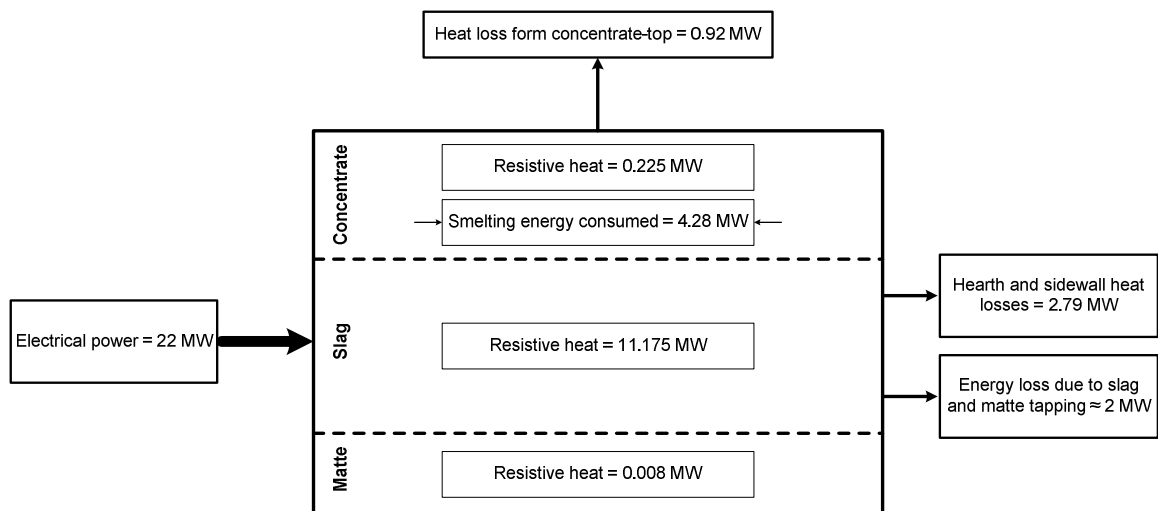


Figure 5.3.1 Energy "black-box" for the 35 % electrode immersion model.

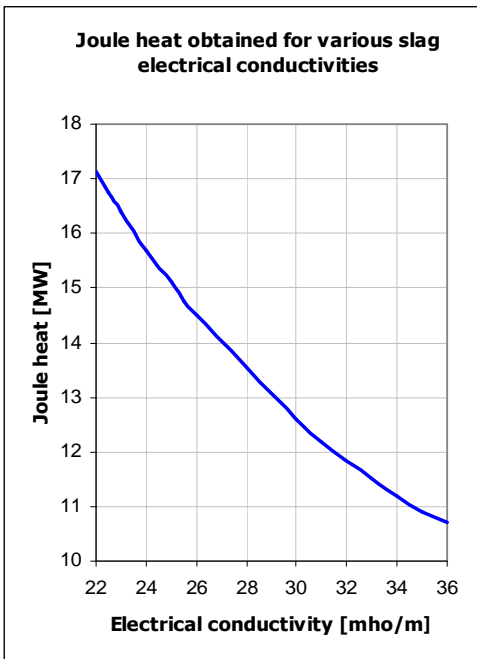
#### **Energy balance:**

$$\text{Heat retained within the furnace} = \text{Energy inputs} - \text{Energy outputs} - \text{Energy consumption}$$

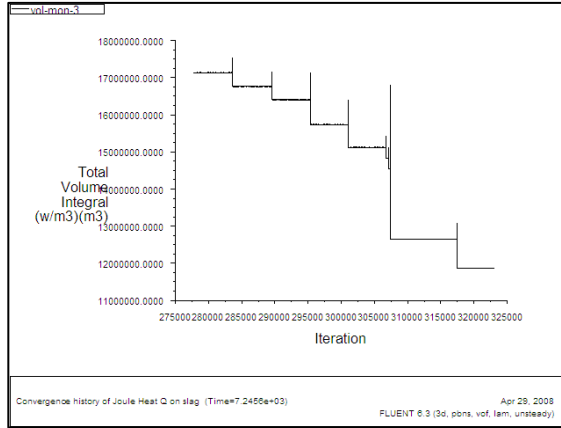
Resistive heat	=	Electrical energy input – Hearth and sidewall losses – Heat loss form concentrate-top – Energy consumption due to smelting – Energy loss due to slag and matte tapping
10.972 + 0.077 + 0.008	=	22.000 – 2.566 – 0.732 – 4.280 – 2.000 [MW]
11.195	=	12.422 [MW]

The heat associated with smelting, which includes resistive heat, the heat-up of material and the heat associated with melting concentrate, is calculated at 17.67 MW. It is also noted that 98% of the total heat generated within the bath is attributed to the slag layer. This compares well with the consulting CFD study (2006) performed on the slag layer with similar energy inputs. The input energy is expected to be further reduced by the heat losses that were not taken into account in the furnace model. As stated in Section 4.4, the heat associated with radiation losses, tapping of the slag and matte layers, chemical reactions and especially arcing at the electrode tips will reduce the furnace energy output.

**5.3.1 Effect of slag electrical conductivity on heat generation**



(a)



(b)

Figure 5.3.2 (a) The heat dissipated as Joule heat as a function of slag electrical conductivity (35% electrode immersion). (b) Changes in Joule heat brought about by changes in electrical conductivity during the simulation.

As mentioned previously under the definition physical properties of the model, Section 4.3.1, the electrical conductivity of the slag layer, being the major source of resistive heat within the furnace, is altered during the model simulation as to obtain the resistive or Joule heat according to the energy balance. The final electrical conductivity, 34 mho/m,

fell well within the range of electrical conductivities computed for the temperature range 2000 – 1700 K (see Appendix A), the typical temperature within the slag. The trend of Joule heat evaluated at different electrical conductivities, provided in Figure 5.3.2, is seen to be nonlinear and follows the trend expected from the inverse proportionality between electrical conductivity and Joule heat, Equation 3.17 ( $q \propto 1/\sigma$ ).

### 5.3.2 Heat distribution within the melt

The Joule heat distribution is seen to follow a similar distribution in the vicinity of the electrodes compared to the current density ( $q \propto J^2$ ), however it shows a sharper radial decrease as seen in Figure 5.3.4. Similar observations were made by Sheng *et al.* (1998) and Xia and Ahokainen (2004). The minority of the electrical power is therefore released in the immediate vicinity of the electrodes. Almost no heat is generated in the bulk of the slag layer which underlines the importance of maintaining a well mixed slag layer for distributing heat within the melt. As seen in the energy balance, very little heat is generated through Joule heat in the matte layer due to its high electrical conductivity.

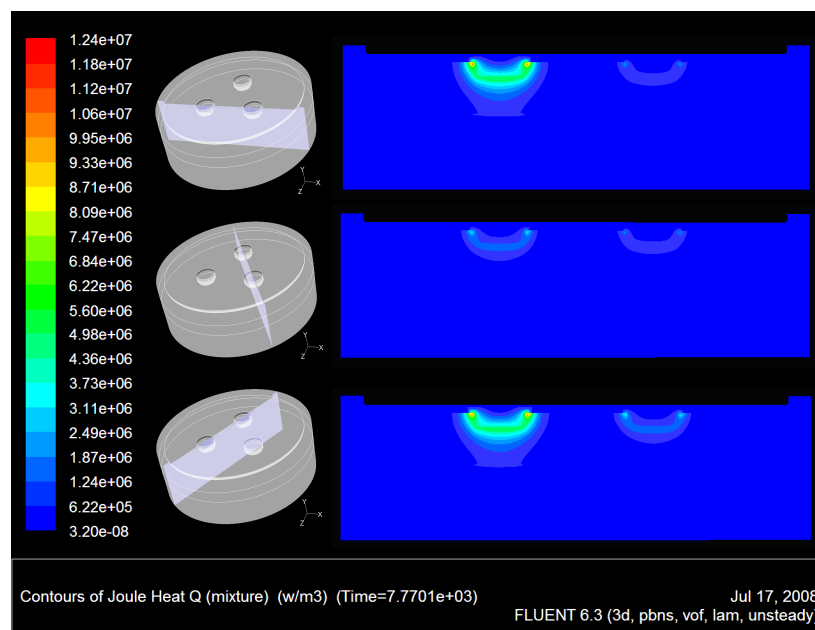


Figure 5.3.3 Joule heat [W] distribution along different vertical cross-sections passing through the electrodes for the 35 % electrode immersion model.



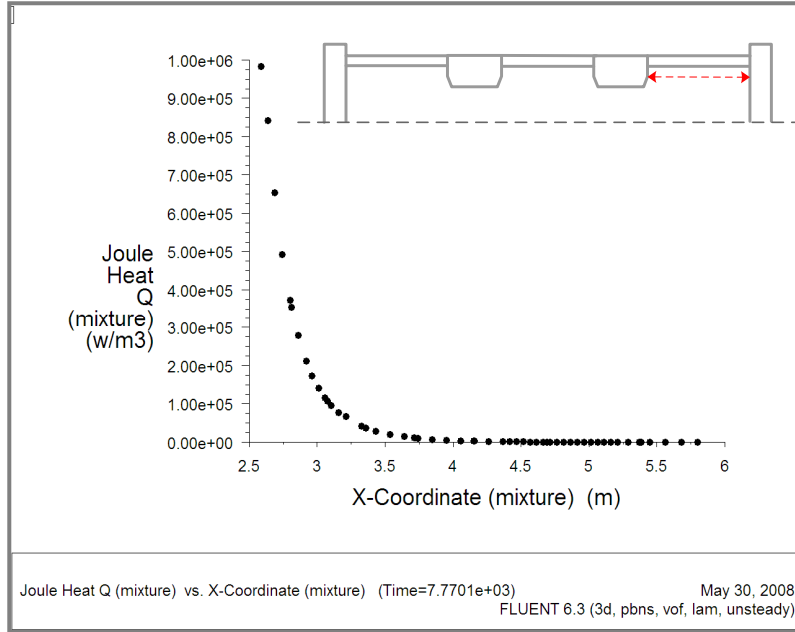
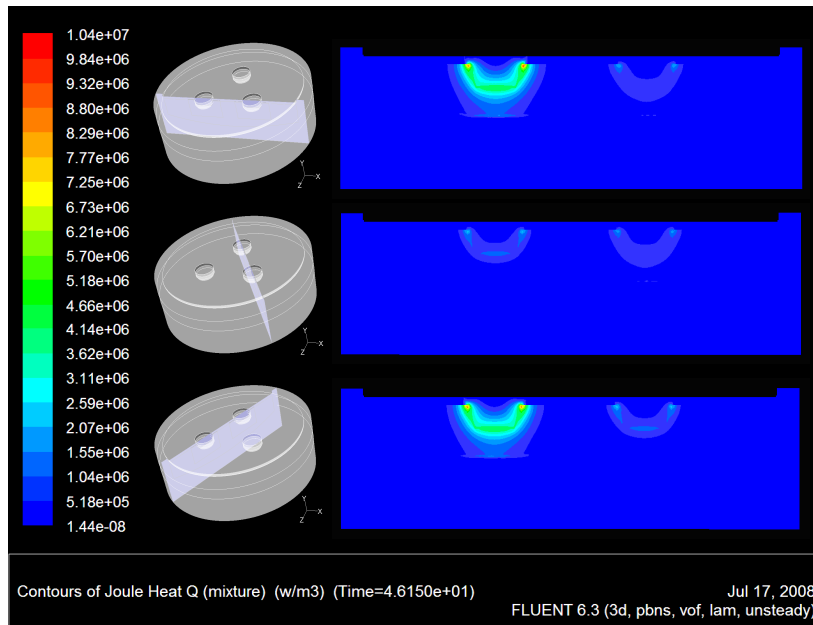


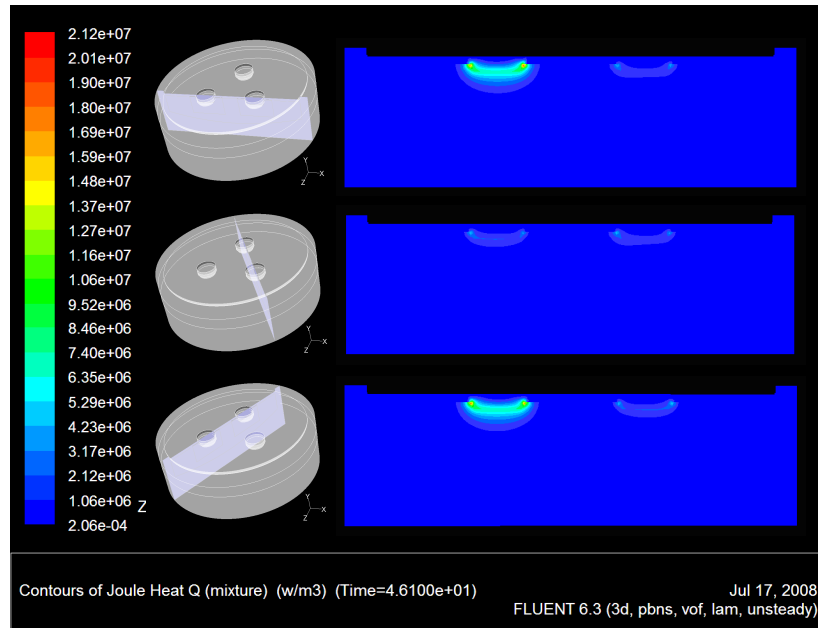
Figure 5.3.4 Joule heat distribution measured along a horizontal line from the electrode surface towards the furnace sidewall.

### 5.3.3 Effect of electrode immersion on the heat distribution

The Joule heat distributions for the other two electrode depths are provided in Figure 5.3.5.



(a)



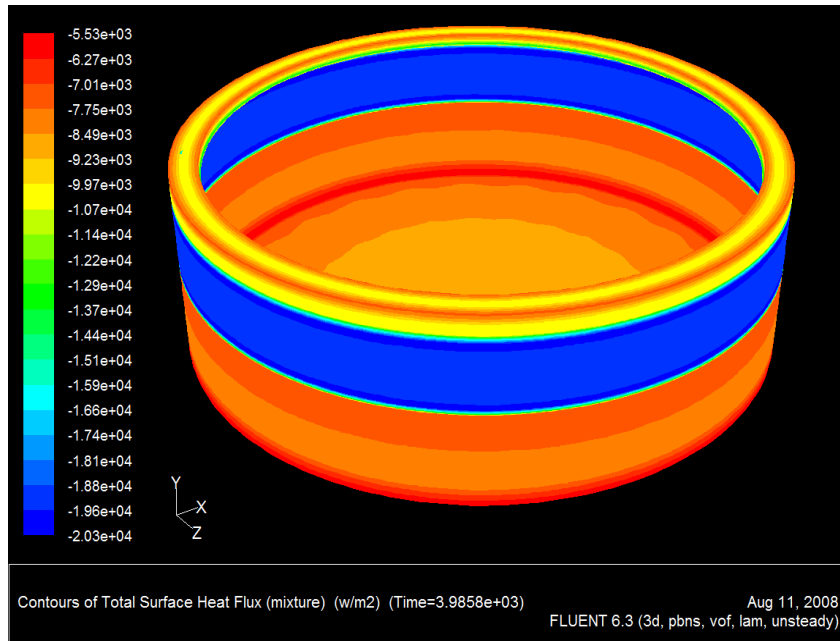
(b)

Figure 5.3.5 Two dimensional profiles of Joule Heat [W] distribution along different vertical cross-sections passing through the electrodes. (a) 55 % electrode immersion. (b) 15 % electrode immersion.

It is evident that a deeper electrode immersion will concentrate the heat generation closer to the matte running the risk of overheating the matte layer. The slight electrode immersion results in the heat generation being concentrated near the slag-concentrate interface. A large slag volume is therefore left to be heated by means of convection. The potential for sub-cooling the slag layer is therefore much higher at lower electrode immersions which is not considered good for the reduction process and metal droplet settling due to the higher resulting slag viscosity [Xia and Ahokainen 2004].

### 5.3.4 Surface heat flux

A reasonably uniform surface heat flux from the outer furnace walls was obtained. Shown in Figure 5.3.6 below, the highest energy is removed from the copper coolers when compared to the flux from the hearth and bottom sidewall, indicating its importance in the overall furnace design.



*Figure 5.3.6 Surface heat flux [ $W/m^2$ ] from the outer walls of the furnace model, taken from the results of the final, complete model.*

## 5.4 Temperature distribution

The temperature distributions obtained for the complete model (35 % electrode immersion with CO-bubble formation) are discussed in this section. As stated, a converged solution was obtained after the temperature distribution had reached a stable stated in time.

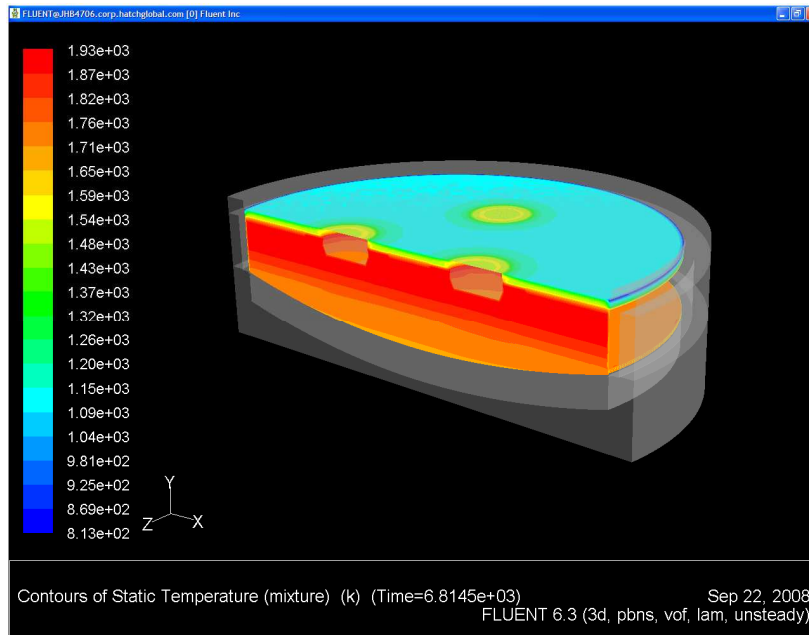


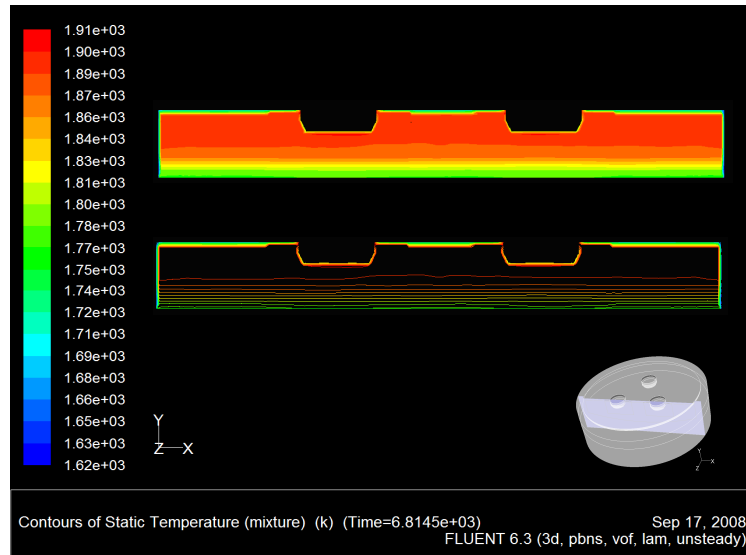
*Figure 5.4.1 Tree dimensional temperature (K) profile obtained for the 35 % electrode immersion model.*

### 5.4.1 Characteristics of temperature distribution within the slag layer

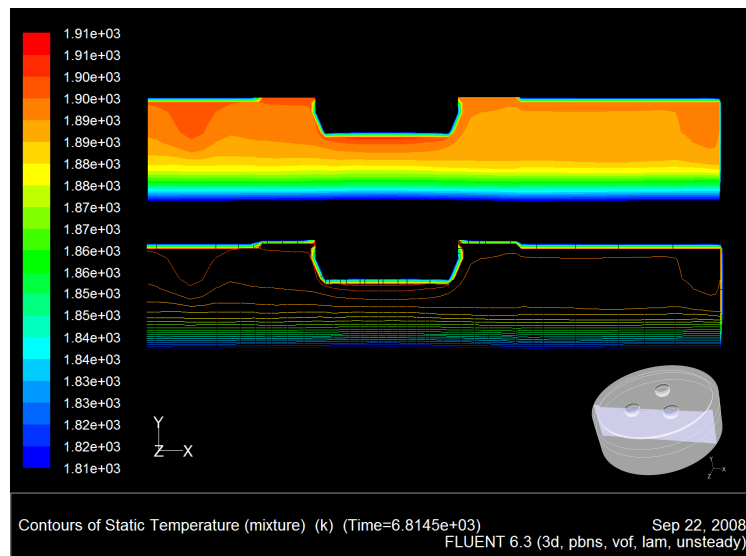
The bulk of the slag layer is seen to be thermally homogeneous, however showing a stratified temperature distribution toward the lower intermediate layer, i.e. at the matte interface. A high temperature area is observed between the electrodes which is presumed to be the result of the heated slag at the electrode interface being swept sideways, meeting the other stream from the adjacent electrodes halfway. This is depicted by Figure 5.4.2 where a high resolution of the temperature distribution within the slag is provided. A high temperature zone is also visible underneath the electrode where the majority of the resistive heat is generated.

These temperature trends correlate well with the observations made by Xia and Ahokainen (2004) whose temperature profiles also indicate a high temperature area towards the inner side of the electrodes. Distinctive radial temperature contours from the

electrode towards the furnace sidewall were not observed as with the study by Sheng *et al.* (1998). The high degree of mixing brought about by the CO-gas bubble momentum and natural buoyancy is presumed to be the cause of the thermal homogeneity observed in the current model results. The high temperature zone underneath the electrode is however also depicted in the findings of Sheng *et al.* (1998).



(a)



(b)

Figure 5.4.2 Two dimensional profiles of temperature [K] within the slag layer along a vertical cross-sections passing through the front two electrodes within a (a) global and (b) high resolution temperature range.

#### 5.4.2 The temperature within the intermediate and matte layers

The stratified nature of the bottom slag and matte layers predicted by the current model agrees well with the results presented by Sheng *et al.* (1998). As stated by Sheng *et al.*,

the stratified nature of the matte is the result of the heating being confined to the top of the molten bath and the poor momentum transfer through the slag/matte interface. This finding is further supported by the slag density analysis performed by Utigard (1994), who found a cold dense slag layer to be present above the slag-matte interface for shallow electrode immersions that permits limited fluid flow and delays thermodynamic equilibrium between the two layers. This area is therefore prone to give rise to accretions in the form of chromite and magnetite deposits, discussed in Chapter 2.

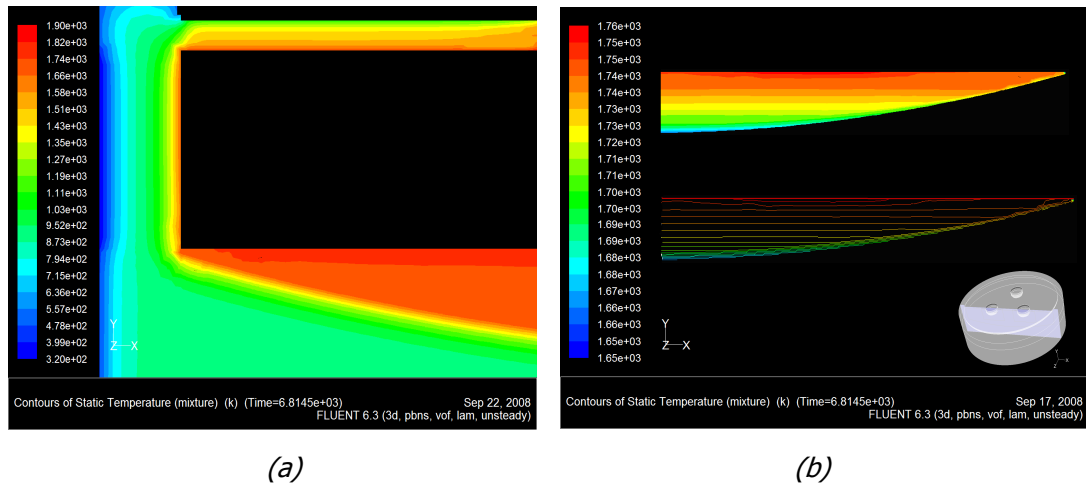
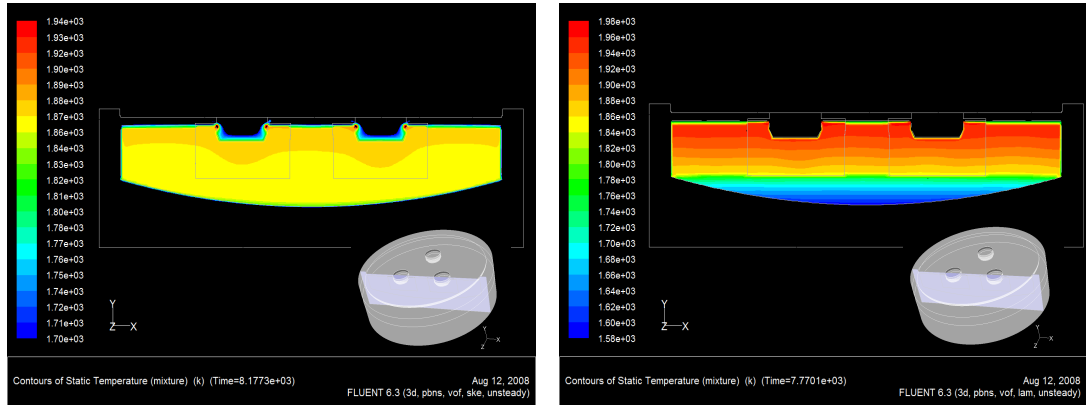


Figure 5.4.3 Two dimensional profiles of temperature along vertical cross-sections passing through the (a) furnace side-wall and (b) right half of the matte layer.

### 5.4.3 Model predictions compared to actual operation

The average temperatures predicted by the furnace model for the slag, matte and concentrate fall well within the actual tapping temperature range of the smelting furnace. This operating temperature range is between 1833 K and 1913 K for the slag and between 1723 K and 1823 K for the matte layer. The model without CO-gas forming at the electrodes predicted a considerably higher slag temperature but lower matte temperature. The lower degree of mixing within the slag when no CO-gas bubbles are released is considered the cause of the high slag temperature and lower convection rate between the material layers and therefore lower matte temperature.

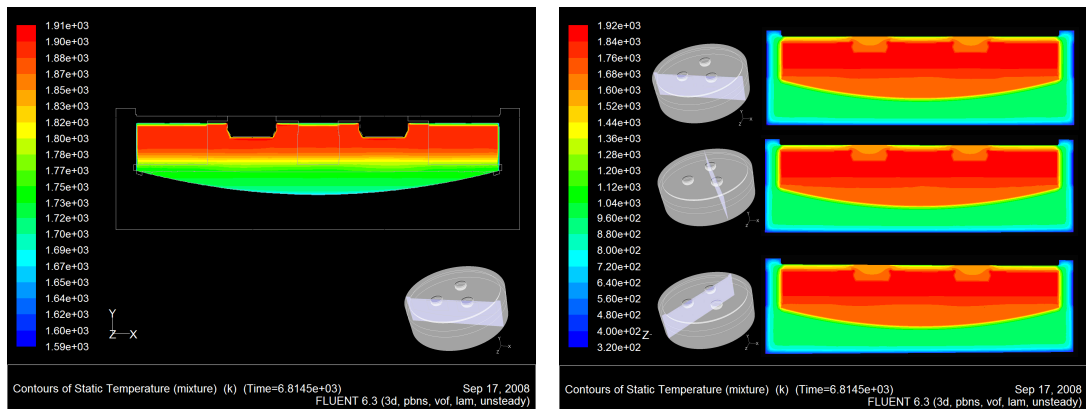
As stated, the modelling of turbulence was neglected after it was found that the flow within the bath was considerably over predicted, revealing a slag and matte at a uniform temperature that is not true for the smelting furnace. The temperature-profile for the matte and slag obtained when the standard k- $\epsilon$  turbulence model was activated is shown in Figure 5.2.3 (a). The thermally uniform slag and matte can be seen.



(a)

(b)

Figure 5.4.4 Temperature [K] contours along a vertical cross-section passing through the front two electrodes obtained for the 35 % electrode immersion model where (a) The standard  $k-\epsilon$  turbulence model was activated and for the case where (b) no CO-gas bubbles were released from the immersed electrode surfaces.



(a)

(b)

Figure 5.4.5 Temperature [K] contours along a vertical cross-section passing through the front two electrodes obtained for the 35 % electrode immersion model (a) for the complete model where laminar flow is at play and CO-gas bubbles are included; (b) The complete temperature contours, showing similar temperatures observed in all directions and around the electrodes.

*Table 5.4.1 Summary of the average and maximum temperatures determined for the different material layers as predicted by the various furnace models.*

<b>Model</b>	<b>Material layer</b>	<b>Average Temperature [K]</b>	<b>Maximum Temperature [K]</b>
Complete model with laminar flow, CO-bubble formation and third intermediate phase	slag	1863.46	1907.26
	matte	1732.42	1757.33
	concentrate	1425.28	1692.71
Model with laminar flow and no CO-bubble formation	slag	1917.14	1991.25
	matte	1691.97	1866.28
	concentrate	1416.57	1975.53
Model with turbulent flow and no CO-bubble formation	slag	1867.60	1899.71
	matte	1860.88	1865.21
	concentrate	1410.01	1927.75

#### **5.4.4 Model comparison with previous studies**

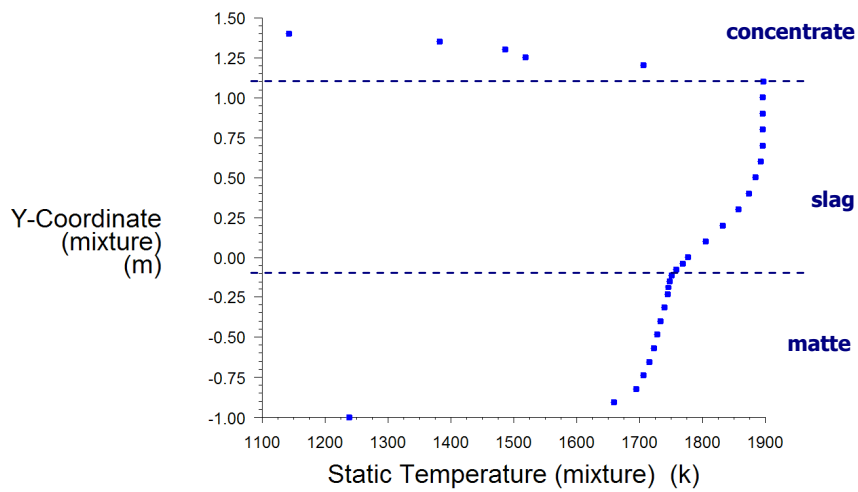
Validation of the characterization of the internal temperature of the furnace is difficult to establish due to the extreme temperatures of operation. However, to provide some credit to the model results, a few published temperature measurements are compared to the complete and final furnace model.

A temperature trend along the centre-line of the furnace model, Figure 5.4.6, shows a steep temperature gradient within the slag and matte layers while a rapid decrease in temperature is observed when moving upwards towards the concentrate top. This temperature distribution is in close comparison to the distribution obtained in the study by Sheng et al. (1998), Figure 5.4.7, where a comparison to actual operating data has been made for validation. A difference in temperatures are observed between the graphs due to different operating set points and the fact that the current modelling was done on a circular furnace while the study by Sheng was focused on a six-in line rectangular furnace. The overall temperature trend through the material layers however does associate well.

The trend in the vertical temperature profile through the slag layer also compares well to the measurements made in the study by Eric and Hejja (1995), Figure 5.4.8 (a). The predicted temperature trend however seems to be steeper. Distorted temperature measurements are obtained from the study by Xia and Ahokainen (2004), which are reported to be doubtful. However the temperature trends obtained from the



computational model by Xia and Ahokainen (2004), *Figure 5.4.8 (b)*, does follow a trend through the slag layer similar to that obtained from the present study.



Y-Coordinate (mixture) vs. Static Temperature (mixture) (Time=6.8145e+03) Sep 17, 2008  
FLUENT 6.3 (3d, pbns, vof, lam, unsteady)

*Figure 5.4.6 Temperature trend along various points on a vertical line through the centre of the furnace ( $x=0, z=0$ ) as predicted by the complete and final furnace model*

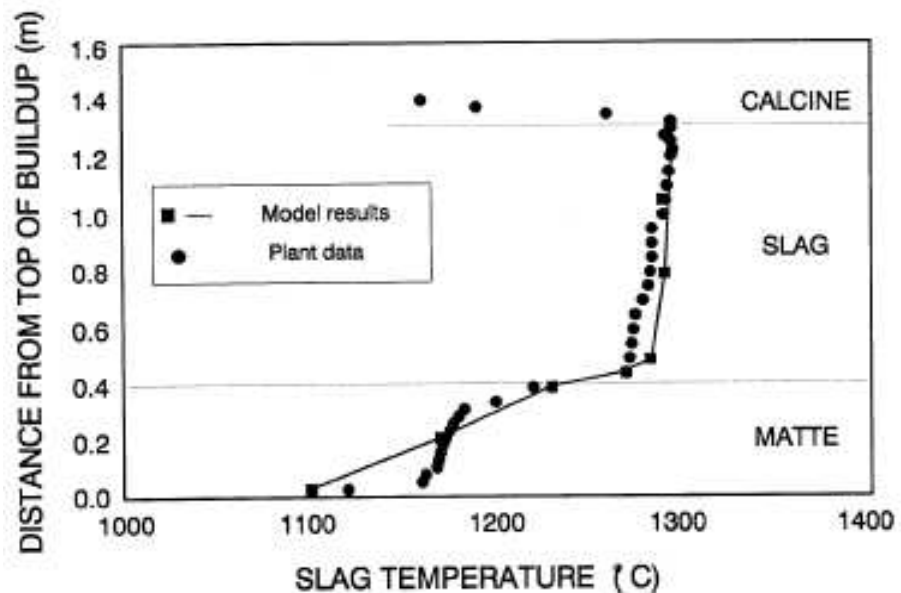


*Figure 5.4.7 The vertical temperature trend through the bath of a 6-in-line electric smelting furnace, showing measured and predicted temperatures (obtained from the study by Sheng et al. (1998)).*

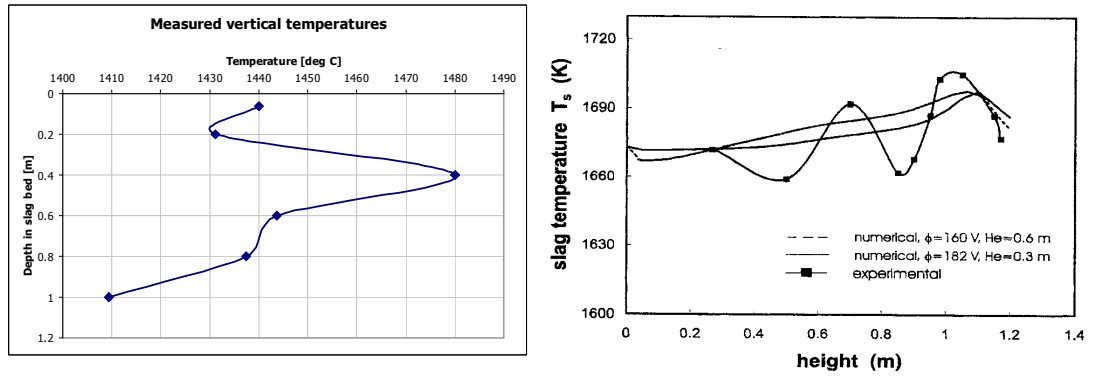


Figure 5.4.8 Temperature trends measured vertically through the slag layer. Obtained from the studies by (a) Eric and Hejja (1995 and (b) Xia and Ahokainen (2004b).

## 5.5 Velocity distribution

It is noticed in the discussion of the predicted temperature profiles that the mixing and concentration of high velocity areas within the bath play an important part in determining the temperature distribution. Through inspection of the velocity profiles, the trends in the temperature distribution are substantiated while the effect of flow phenomena, particularly the induced flow resulting from CO-bubble formation, is portrayed. In the following discussion, the flow observed within the slag and matte layers are described while the differences in mixing between the case with and without gas induced flow are highlighted.

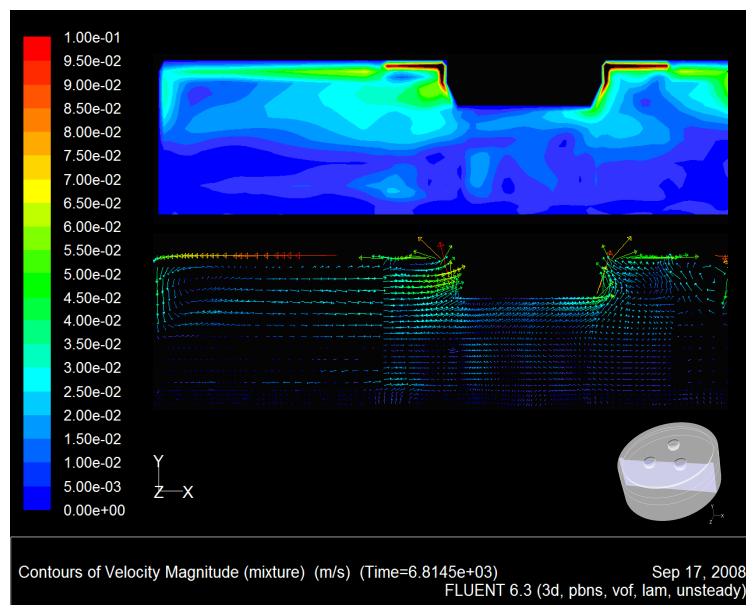
As far as is known, this is the first account given of the flow within the matte layer with a dynamic interface present between the two fluid layers, made possible through multi-phase modelling. Previous studies with flow in the matte layer incorporated a stationary, non-slip interface allowing heat transfer by means of conduction only [Sheng *et al* 1998, Jardy *et al.* 1986].

### 5.5.1 Flow within the slag layer

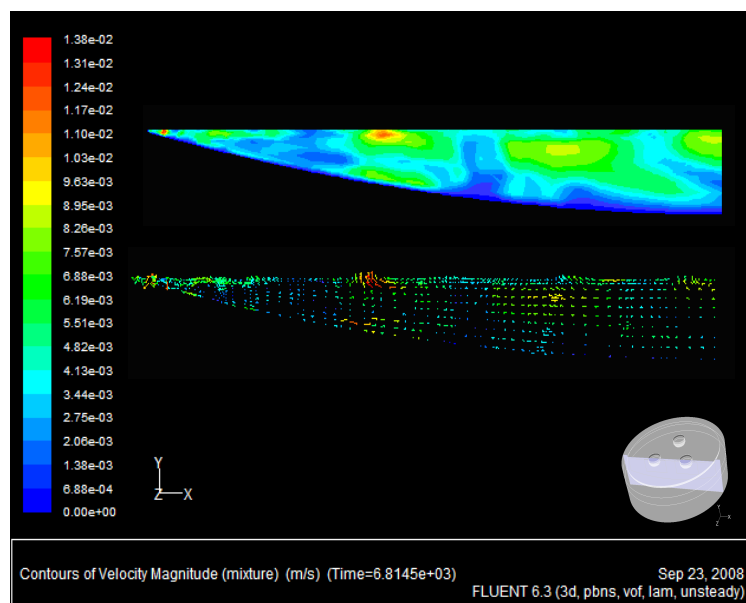
The flow profiles that were obtained for the complete model where CO-bubbles were released from the immersed electrode surfaces are provided in Figure 5.5.1 below. The slag layer is seen to be well mixed and the flow three-dimensional with very high velocities observed at the immersed electrode sides and at the slag-concentrate interface. These high velocities are considered the result of the CO-gas bubbles, represented by the discrete phase point-forces, exchanging momentum with the immediate slag where it is released from the electrode surface. The slag is dragged upward towards the slag-

concentrate interface where the bubbles are allowed to escape, therefore forcing the entrained slag side-wards when colliding with the solid concentrate.

The slag on the outer side of the electrodes is seen to make its way to the furnace sidewall where it cools and evidently settles downward, moving in a circular motion back to the bottom of the electrode. The slag dragging along the inner side of the electrode is seen to meet the stream from the adjacent electrode halfway where the streams collide and is forced downward. A horizontal cross-section through the electrodes presented in Figure 5.5.4 allows this to be visualized. The highest velocities are therefore observed to be midway between the electrodes. Very little flow activity is observed within the bottom half of the slag layer. Flow within the region with a defined high viscosity is seen to be particularly low, as is expected.



(a)



(b)

*Figure 5.5.1 Two dimensional contour and vector profiles of velocity [m/s] within (a) the slag and – clipped to a maximum of 0.1m/s to allow higher resolution of surrounding velocities and (b) matte layers along a vertical cross-sections passing through the front two electrodes. Obtained from the complete model with CO-bubble release from the immersed electrode surfaces.*

### **5.5.2 Flow within the matte layer**

The flow within the matte layer appears to be outwards in the upper part and inward along the hearth. The flow is seen in the vector plot of Figure 5.5.1 (b) to be multi-dimensional with the highest flow concentrated towards the sharp edges of the matte volume. The velocities within the matte are observed to be much lower compared to velocities experienced within the slag layer. The low velocities at the bottom-hearth are particularly concerning with regard to the high potential of deposit build-up that, on the long term, could reduce the capacity of the furnace.

### **5.5.3 The slag-matte interface**

The modelling of a highly viscous intermediate layer between the slag and matte revealed a fairly stationary interface and stagnant flow within the layer itself. Sheng *et al.* (1998) provides two accounts to affirm the presence of an immobile interface and low motion within the bottom slag. Movement of the interface is expected if the shear stress above the interface can overcome the interfacial tension holding the interface firm. The restraining force, or interfacial tension, for the model was specified as 0.4 N (determined in Appendix A.4). The low velocity and therefore weak shear stress present in the intermediate layer is therefore considered the cause of the motionless interface.

The highly viscous intermediate layer therefore provides a good representation of the actual system where a “sticky” chromite and magnetite layer is expected to rest on the matte layer. This is the second account given by Sheng *et al.* (1998) for why a stationary interface is expected. The bottom, colder slag is also mentioned to act as dead volume for low electrode immersion in the study by Urquhart *et al.* (1994). The implication of omitting the highly viscous intermediate layer is identified in the discussion below.

### **5.5.4 Flow within the bath in the absence of CO-bubble induced motion and a high viscosity intermediate layer**

The differences between the flow regimes brought about by CO-bubble induced motion and through natural buoyancy only were found to be significant. Figures 5.5.2 and 5.5.3

below provide the flow contour and vector plots obtained for the simulation where the discrete particle injections from the electrode surfaces were neglected. Considerably less flow activity and lower velocities are present around the electrodes when compared to the situation with gas injection. An overall trend can however be identified for flow in the upper part of the slag layer, where slag is heated underneath the electrodes resulting in an decrease in density and consequent upward flow due to buoyancy. The heated slag makes its way to the furnace sidewall where it again cools, increases in density and settles. More swirling motion in the bottom slag is observed for the buoyancy induced flow.

Flow within the matte layer is also found to differ from the final model. The effect of the absence of a highly viscous intermediate layer is portrayed by the velocity profiles within the matte. The highest flow within the matte of the model without an intermediate layer is observed at the slag-matte interface and it is believed that the slag layer exerts drag force on the underlying matte. The low matte viscosity (two orders of magnitude lower than that of the slag layer) is presumed the cause of the matte's susceptibility to be dragged by the movement of the bottom slag. This high velocity at the slag-matte interface does not correlate with the accounts of a stationary interface discussed above. The incorporation of a highly viscous intermediate in the final model attempt is hereby substantiated.

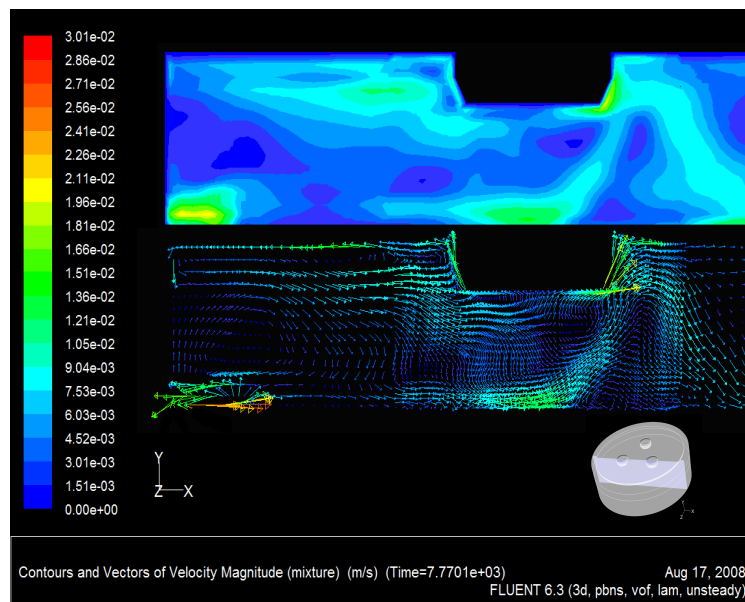


*Figure 5.5.2 The contour and vector distribution of velocity magnitude [m/s] within the slag layer along a vertical cross-section passing through the centre of the front left electrode, obtained from the model without CO-bubble injection and intermediate slag layer.*

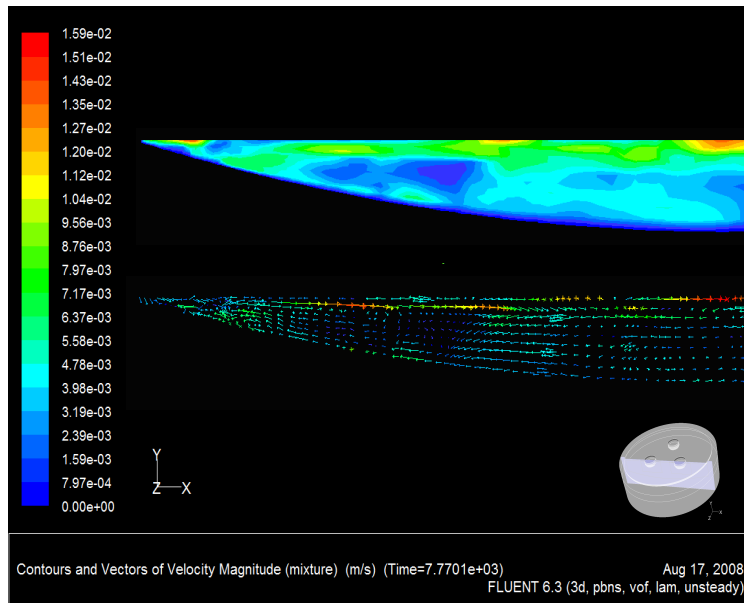


Figure 5.5.3 The contour and vector distribution of velocity magnitude [m/s] within the matte layer along a vertical cross-section, obtained from the model without CO-bubble injection and intermediate slag layer.

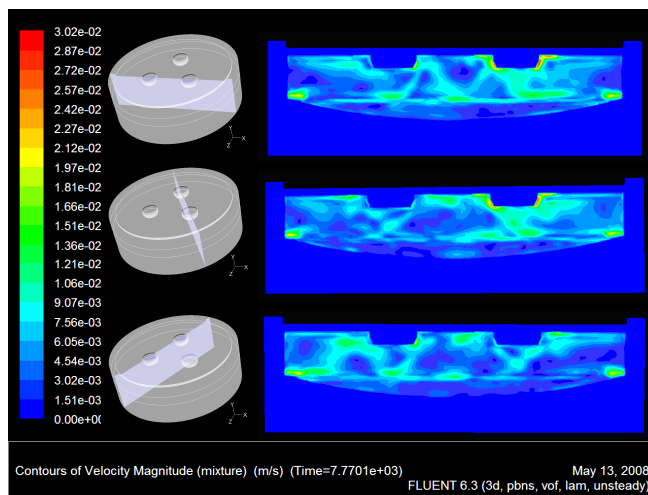


Figure 5.5.4 The contour profiles of velocity magnitude [m/s] within the furnace bath of the model without CO-bubble injection and intermediate slag layer along a vertical cross-section passing through the centre of the electrodes.

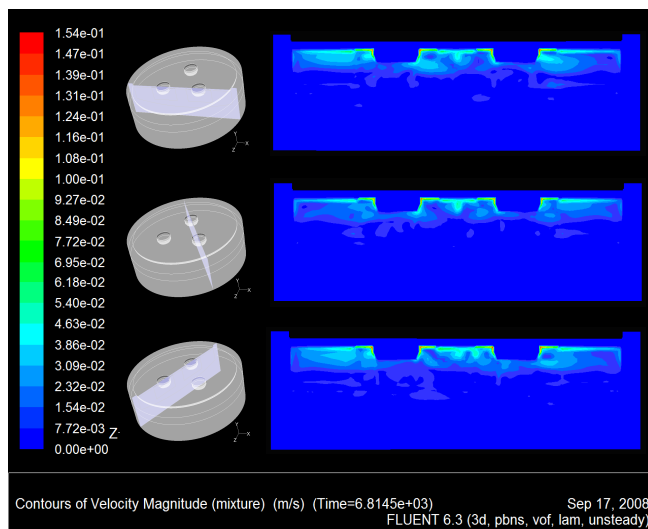


Figure 5.5.5 The contour profiles of velocity magnitude [m/s] within the furnace bath of the model with CO-bubble injection and intermediate slag layer along a vertical cross-section passing through the centre of the electrodes.

### 5.5.5 Importance of bubble induced flow

The flow regime brought about within the slag layer through the CO-bubbles released from the electrode surfaces is viewed as a reasonably favourable flow regime for good operation of the slag layer. Strong slag flow is present in the region where the maximum resistive heat is generated, thus the distribution of heated slag throughout the bath is thereby promoted. Lower flow velocities in the lower part of the slag layer favour the settling of matte droplets but increase the potential for the build-up of unwanted deposits. The low velocity area at the slag-matte interface is a very susceptible area for chromite and magnetite accumulation, as discussed.

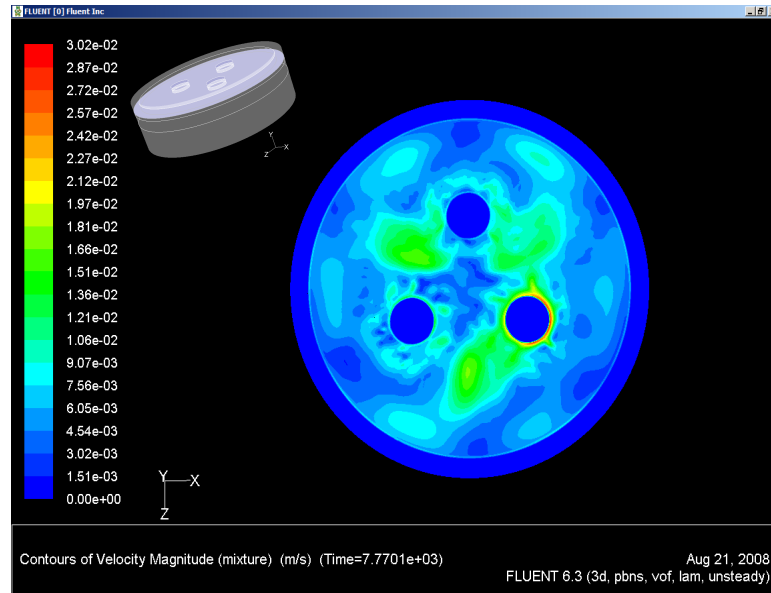
The figures below show the flow contours on a horizontal cross-section through the electrode and show the highest flow to be located halfway between the electrodes. To recall, the highest temperatures within the slag bath were also observed midway between the electrodes (Figure 5.4.2). It is interesting to see the perturbation brought about by the electrodes being amplified in these regions. These areas can be described geometrically in Figure 5.5.7 by intercepting circles of diameter equal to the furnace diameter and positioned with their centre points on the perimeter of the furnace outline. The high flow areas observed under natural buoyancy, Figure 5.5.6 (a) show a shorter active flow area, falling within the shaded region of Figure 5.5.7.

The identification of these high flow areas permits the recommendation for tap-hole positioning, bearing in mind the settling of matte droplets. If the matte droplets are formed where the heat is most concentrated, i.e. at the electrode surface, they have to make their way through the bulk of the slag towards the underlying matte layer [Eric and Hejja, 1995; Xia *et al.*, 2004b]. Matte droplets will therefore most likely be in suspension within the identified regions of high flow activity. If a tap-hole is situated nearby these regions, the potential for entrainment of the valuable matte droplets with the tapped slag will become higher.

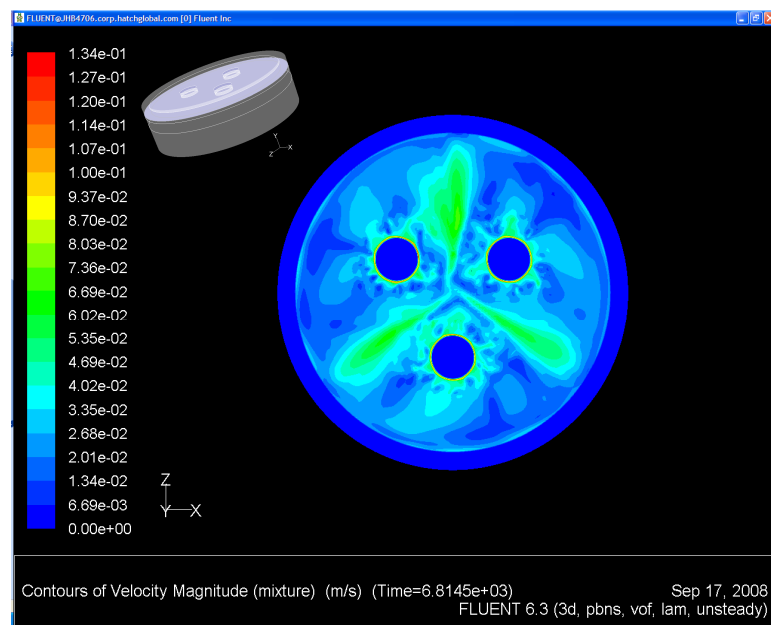
The identified areas of high flow activity do compliment the current furnace design based on the choice of its diameter. The high flow areas are well contained within the bounds of the furnace walls. A smaller furnace diameter would result in the active areas being concentrated too close to the furnace walls while a larger diameter could lead to possible dead volume at the side due to a lack of flow activity.

It is also evident that a deeper electrode immersion will result in an increase in motion within the slag due to the longer path being created for the gas bubbles to travel and exchange momentum before escaping at the surface. The elimination of stagnant slag at

the bottom could therefore be achieved and possibly keep chromite and magnetite deposits in suspension within the slag, preventing them from settling and accumulating. This is again a trade-off in terms of the potential for matte droplets that will be kept in suspension for longer under active slag motion while the risk of a deep electrode immersion on the heat allocation was discussed.



(a)



(b)

Figure 5.5.6 Velocity magnitude (m/s) contour profiles obtained for the 35% electrode immersion model (a) without CO-bubble injection and (b) with CO-bubble injection along a horizontal cross-section through the upper part of the slag layer.



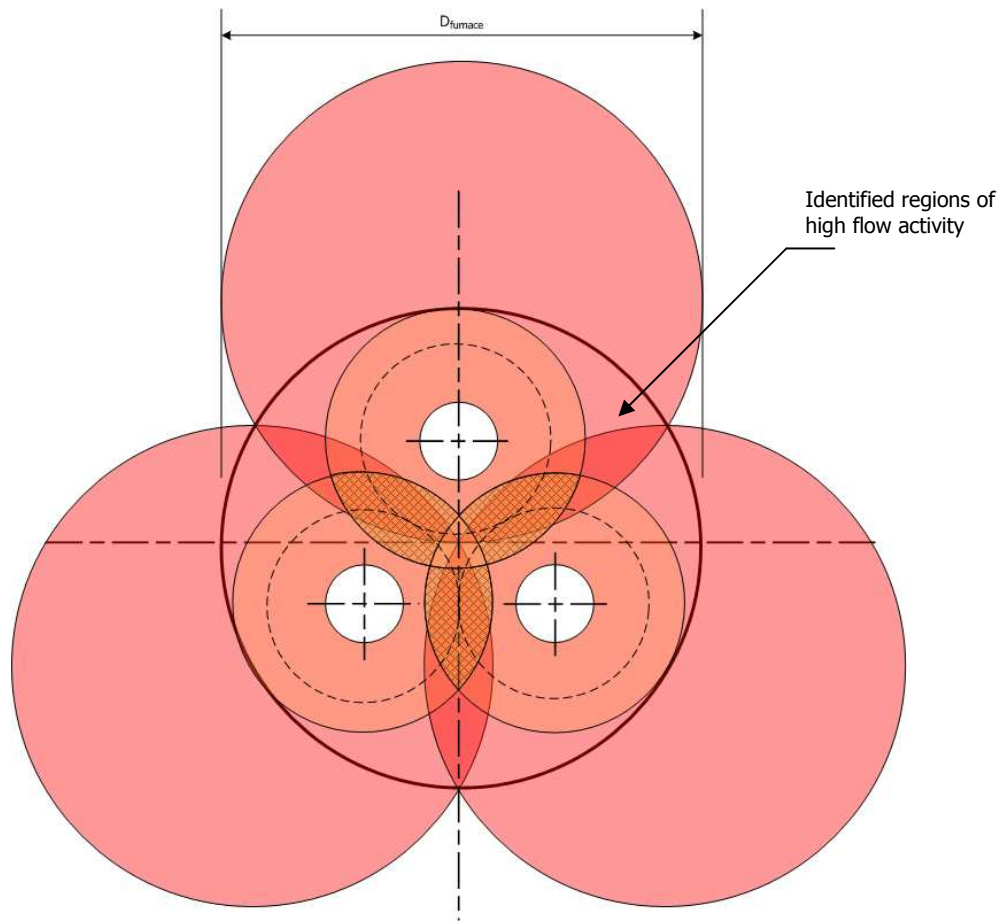


Figure 5.5.7 Geometric representation of the active flow areas identified within the slag layer.

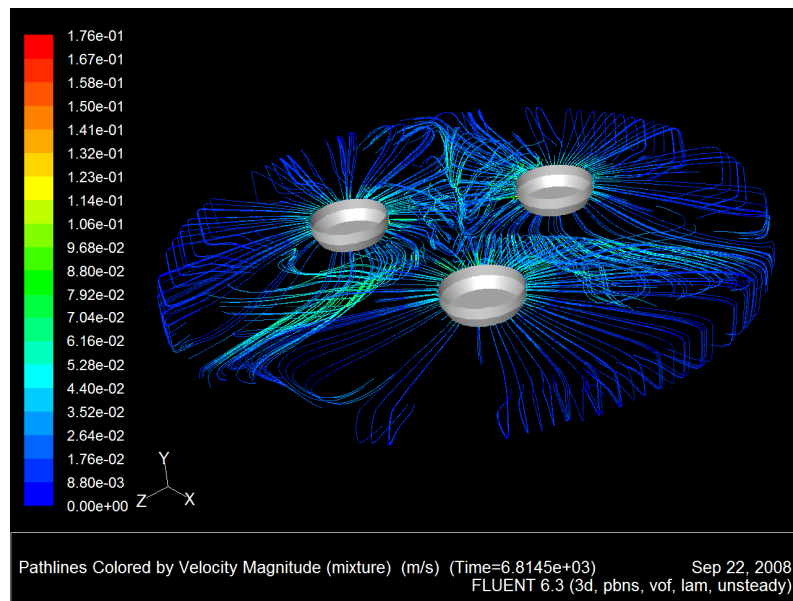
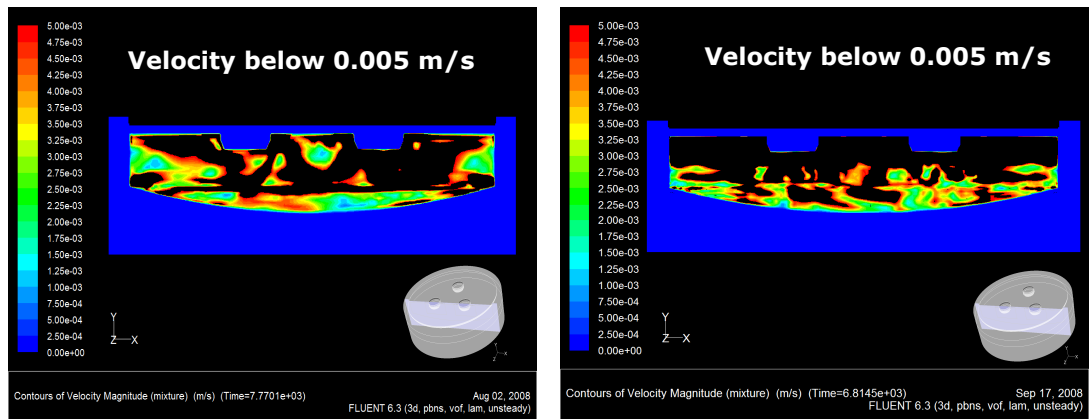


Figure 5.5.8 The flow pathlines predicted for the complete model where CO-bubbles are released from the electrode surfaces.



(a)

(b)

Figure 5.5.9 Velocity contours [m/s] below 0.005m/s criteria for the model (a) without CO-bubble formation and (b) with CO-bubble formation at the electrodes.

A three dimensional view of the pathlines created by the flow streams originating at the electrodes is shown in Figure 5.5.8. Again, the high flow areas halfway between the electrodes are seen. In Figure 5.5.9, a comparison between the low flow areas or dead volume, defined as regions of flow below a conservative 0.005 m/s, is given for flow within the slag where CO-bubbles are absent and injected. It is seen that the presence of bubble momentum considerably eliminates dead volume within the slag.

### 5.5.6 The effect of including turbulence modelling

The understanding of the homogenous temperature obtained for the slag and matte when including turbulence modelling can be furthered when examining the velocity profiles, provided in Figure 5.5.11 (b). A clear over-prediction of the flow regime is seen in the two very large swirls developing underneath the electrode, up towards the furnace sides where it flows directly to the bottom of the slag layer.

A comparison to the laminar profiles, Figures 5.5.10 and 5.5.11 (a), reveal a considerably smaller swirling motion, with the main swirl never reaching the bottom of the slag but changing direction towards the middle of the slag bath halfway down the sidewall of the furnace. The flow regime obtained under active turbulence modelling does not coincide with the accounts of flow within the bottom slag layer identified by Sheng *et al.* (1998) and Utigard *et al.* (1994). Even when including a highly viscous intermediate layer between the slag and matte layers, the flow remains over-predicted and the slag and matte temperatures unrealistic.

### 5.5.7 Flow comparison between models

To compare flow results for the different models investigated, the average and maximum velocities are tabulated below and the vector plots for the flow field within the bath as obtained for the different scenarios are provided thereafter.

*Table 5.5.1 Summary of the average and maximum temperatures determined for the different material layers as predicted by the various furnace models.*

Model	Material layer	Average Velocity [m/s]	Maximum Velocity [m/s]
Complete model with laminar flow, CO-bubble formation and third intermediate phase	slag	0.0198	0.2615
	matte	0.0046	0.0329
Model with laminar flow and no CO-bubble formation	slag	0.0058	0.0363
	matte	0.0043	0.0218
Model with turbulent flow and no CO-bubble formation	slag	0.0120	0.04622
	matte	0.0033	0.01634

The highest velocities are obtained for the model where CO-bubble injection is active. Flow for the model with only natural buoyancy at play revealed very low velocities, particularly within the matte layer.

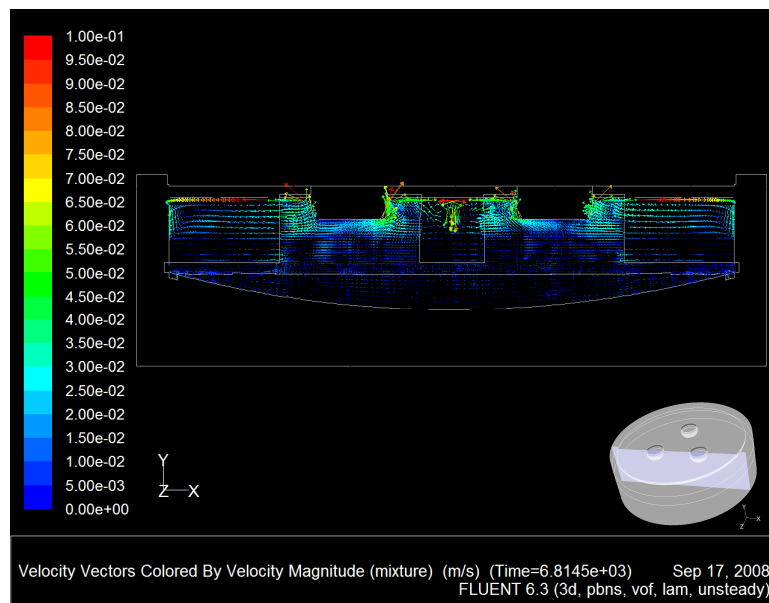
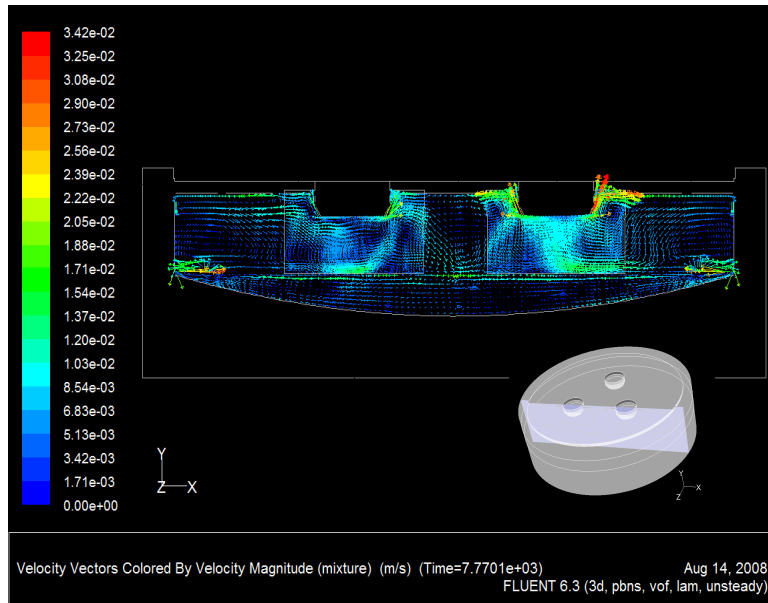
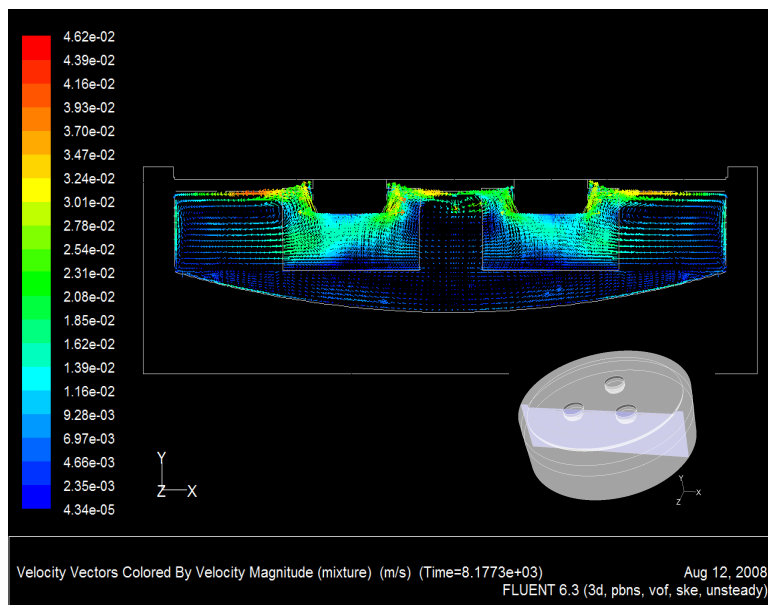


*Figure 5.5.10 Flow vectors [m/s] within the furnace bath for the model with CO-bubble formation and highly viscous intermediate layer.*



(a)



(b)

Figure 5.5.11 Flow vectors [m/s] within the furnace bath for the model (a) without CO-bubble formation and a highly viscous intermediate layer and (b) the model where turbulence modelling was activated.

---

# CHAPTER 6

## CONCLUSIONS

---

A successful investigation into the electrical, thermal and flow behaviour within the circular, three-electrode Lonmin furnace has been performed with the aid of the commercial CFD code Fluent. This was achieved by creating a virtual environment where the actual furnace was described by a three-dimensional geometry, appropriate physical properties and numerical models. Based on the findings from this study conclusions are grouped according to the model variables that were investigated.

### 6.1 Electrical current

---

The electric current path between the electrodes has been identified and characterized. The majority of the current was observed to flow vertically downward from the input electrode towards the more conductive matte layer while little current is seen to flow directly between the electrodes. The electrical current is seen to flow horizontally within the matte layer in the direction of the receiving electrode and again vertically upward through the slag. The path of least resistance is therefore via the matte layer.

Uncertainty regarding the mode of current flow from the electrodes is clarified by the present study. Current flow is seen to be hyperbolic from the input electrode and parabolic towards the output electrode. The evaluation of the current density distributions for three different electrode immersions also made it evident that deeper electrode immersions will result in an increase of current flow by means of the matte layer whereas the portion of current flow between electrodes is increased when operating at lower immersions. The slag resistance was found to increase with decreasing electrode immersion.

## 6.2 Electric potential

---

The electric potential distribution was successfully simulated and found to be well within on-line electric potential operating range. The electric potential gradients were found to decline rapidly in a radial fashion from the electrodes. No electric potential gradients were therefore observed within the matte layer. The matte is therefore not considered to be under considerable magneto-hydrodynamic strain, which validates the important assumption of neglecting magnetically induced forces within the present study.

## 6.3 Energy balance and power distribution

---

An appropriate and comparative temperature and heat distribution within the melt was obtained through a well-established energy balance. The most important heat-losses were considered in the model and included the heat associated with melting and heating-up of concentrate. The required resistive heat according to the energy balance was maintained by adjusting the slag electrical conductivity within the range of typical slag electrical conductivities throughout the simulation process.

The majority, i.e. 98%, of the resistive heat is generated within the slag layer. A total of 17.48MW can be assigned to the process of concentrate smelting compared to the 22MW electrical power input. This total includes the resistive heat and the heats associated with melting and heating-up of concentrate. The Joule-heat distribution was found to follow the trend in the current and electric potential distribution where the highest portion of the generated heat is located in the immediate vicinity of the electrode. It is therefore clear that a very deep electrode immersion runs the risk of overheating the matte layer, as was indicated through the investigation of different electrode depths.

## 6.4 Fluid flow

---

The modelling of the electric smelting furnace has been significantly furthered with respect to the modelling of the two-fluid slag and matte layers. As far as it is known this study presents the first attempt to modelling both the slag and matte as fluid continuums with a dynamic interface and not a non-slip wall boundary as with previous accounts. Flow within the slag layer is well mixed with the highest circulating flow occurring at the electrodes where the warmer slag is heated and ascends due to natural buoyancy and the CO-gas bubbles injected from the

electrode surface. Little flow is observed in the bottom slag layer where the highly viscous slag is present.

A comparison between the model cases with and without CO-gas bubble formation at the electrode tips revealed a large difference in the extent of mixing within the slag. Flow within the slag is approximately half an order of magnitude lower when no CO-gas bubbles are present, thereby indicating its importance in keeping the bath well mixed and distributing the heat evenly. The resulting flow from the gas is also seen to force the fluid to meet halfway between the electrodes and so creating regions of high activity with respect to melting and matte droplet formation.

Flow within the matte was found to be outward towards the top, near the interface, and inward along the bottom hearth. The model without a highly viscous slag layer revealed high velocities at the slag-matte interface. This is considered an indication of a possible drag-force exerted by the slag on the matte. High flow at the slag/matte interface was reduced when incorporating a highly viscous slag layer above the interface.

Turbulence modelling was attempted in the furnace modelling but was found to over-predict the flow, and consequently convection within the melt. Evaluation of the flow regime within the fluid layers revealed the flow to be predominantly laminar.

## 6.5 Temperature

---

The temperature distribution within the material layers has been fully developed. The slag layer was observed to be at a uniform temperature, partially the result of being well mixed. The highest temperatures are however observed underneath and halfway between the electrodes. The bottom of the slag layer is at lower temperature due to the low flow activity within this region resulting from the denser and more viscous slag. This region is therefore a good indication to where chromite and magnetite deposits are likely to form. The temperature distribution within the matte layer can be described as being stratified.

Good comparison to measured temperature trends from previous modelling attempts has been achieved. The average temperatures for the slag and matte did also fall well within the slag and matte tapping temperatures recorded for the actual furnace.

## 6.6 General

---

It is believed that the present study has significantly furthered the modelling of the electric furnace and provided a clearer understanding of the system of electric smelting. CFD has proven to be a valuable tool in analysing the nature of the system within the furnace and it is believed that without CFD, such an investigation would be much more costly and difficult to perform due to the extreme and aggressive environment required for smelting PGM bearing concentrates.



---

# CHAPTER 7

## RECOMMENDATIONS

---

The electric smelting furnace has been identified as a dynamic system that hosts a series of complex phenomena that are interactive in determining the outcome of the smelting process. The current model has accomplished a large extent in describing the furnace system; however further investigations are required for creating a complete and holistic furnace representation. In the light of improving the current model and future modelling attempts, the recommendations are presented in below.

- Model validation has been performed through comparison to previous modelling results and the actual furnace operating range. Further validation is essential for creating complete confidence in the model results. Voltage and temperature measurements within the bath along with additional surface temperatures would be of great value in validating the model predictions.
- The true worth of a CFD model will be achieved by performing a sensitivity analysis based on the effects that have a significant impact on the operation of the actual furnace. This would include the influence of electrode depth on the temperature and flow distribution within the melt that could not be investigated in the current study due to large computational extent of the model and time constraint. Investigations into the effects of material layer depth, geometric modifications, power input and even composition changes would be of great value and should be considered in future modelling. Effects on a smaller scale that could impact the overall operation include CO-bubble diameter, slag-matte surface tension, localized turbulence etc.

- The current study assumes a definitive electrode shape in an attempt to approximate the effect of pencilling. The influence of electrode shape on the distribution of current from the electrode should be further examined.
  
- A highly viscous bottom slag layer was assumed in the last stage of the furnace model, however the exact form build-up within the furnace bath would provide a more accurate influence on fluid flow within the bottom-slag region. Also of high importance is the formation of freeze lining at the colder side-walls, especially in the region of the copper coolers and at the concentrate-slag interface. It is believed that this could impact flow and heat distribution within the furnace and should therefore be studied in future attempts.
  
- Although the influence of induced magnetic forces on fluid flow has been identified as being negligible compared to buoyant forces, the study of its influence on the overall model outcome will provide complete confidence in the assumption and affirm its influence on flow.
  
- Finally, modelling of the exact concentrate melting point will be a great improvement on the current assumption where distinctive smelting zones have been allocated to the concentrate layer.

---

# CHAPTER 8

## REFERENCES

---

Aharoni, A., *Introduction to the theory of Ferromagnetism*, Oxford Clarendon, 1996.

Barnes, A.R. and Newall, A.F., *Spinel removal from PGM smelting furnaces*, Southern African Pyrometallurgy, Jones, R.T., eds., SAIMM, Johannesburg, 5-8 March, 2006.

Barth, O., *Electric Smelting of Sulfide Ores, Extractive Metallurgy of Copper, Nickel and Cobalt*, Queneau, P. ed., Metallurgical Society of AIME, pp. 241-262, 1960.

Bertotti, G., *Hysteresis in magnetism: for physicists, material scientists, and engineers*, Academic Press, New York, pp. 4-11, 1998.

Betteridge, W., *Nickel and its alloys*, Ellis Horwood Limited, 1984.

Biswas, R. and Straw, R.C., *Tetrahedral and hexahedral mesh adaptation for CFD problems*, *Applied Numerical Mathematics* Volume 26, 1998, p. 135-151, Retrieved: from Elsevier library.

Confidential consulting work on electric smelting furnace, 2006.

Celmer, R.S., Kaiura, G.H. and Toguri, J.M., *Chemical reactions and materials transport in the electric smelting of highly roasted nickel-copper concentrates*, Proceedings of the Reinhardt Schuhmann International Symposium on Innovative Technology and Reactor Design in Extraction Metallurgy, Gaskell D.R., Hager J.P., Hoffman J.E., Mackey, P.J. (eds), TMS, pp. 419-431, 1986.

- Choudhary, M and Szekely, J., *Some general characteristics of heat and fluid flow phenomena in electric melting sand smelting operations*, Transactions of the Institute of Mining and Metallurgy, Section C, Vol. 90, 1981, pp. 164-173.
- Cloudhary, M. and Szekely, J., *The effect of temperature dependant electrical conductivity on flow and temperature fields in slags in ERS systems*, Metallurgical Transactions B, Volume 12B, pp. 418-421, June, 1981,
- Cramer, L.A., *The extractive metallurgy of South Africa's platinum ores*, JOM, Vol. 53, Nr.10, pp.14-18, October 2001.
- Crowe, C.T., *Multiphase flow handbook*, CRC/Taylor & Francis, Boca Raton, FI, pp. 13-1 – 13-20, 2006.
- Davidson, P.A., *An introduction to magnetohydrodynamics*, Cambridge texts in applied mathematics, Cambridge University Press, 2001.
- Dilawari, A.H. and Szekely, J., *A mathematical model of slag and metal flow in the ESR process*, Metallurgical Transactions B, Volume 8B, pp. 227-236, June, 1977
- Dilawari, A.H. and Szekely, J., *Heat transfer and fluid flow phenomena in electroslag refining*, Metallurgical Transactions B, Volume 9B, pp. 77-87, March, 1978.
- Dosa, G., Kepes, A. and Ma T., *Computer control of high power electric furnaces*, Challenges in Process Intensification Symposium, 35<sup>th</sup> Annual Conference of Metallurgists of the Metallurgical Society of CIM, Montreal, Quebec, Canada, 24-29 August, 1996.
- Eksteen, J.J., *Confidential research proposal to Lonmin Platinum*, Department of Process Engineering, University of Stellenbosch, 2007.
- Eric, R.H. and Hejja, A.A., *Dimensionlizing, scale-up and operating consideration for six electrode electric furnaces - Part I: Current and heat flow in the slag*, Proceedings of 1995 EPD Congress, Las Vegas, Warren, G.W. (ed.), Warrandale, Pennsylvania, TMS, pp. 223-238, 1995.
- Eric, R.H. and Hejja, A.A., *Dimensionlizing, scale-up and operating consideration for six electrode electric furnaces - Part II: Design and Scale-up considerations for furnaces treating PGM-containing copper-nickel concentrates*, Proceedings of 1995 EPD Congress, Las Vegas, Warren, G.W. (ed.), Warrandale, Pennsylvania, TMS, pp. 239-257, 1995.

- Eric, R.H., *Separation, settling and flow phenomena in electric smelting of Cu-Ni concentrates*, Scandinavian Journal of Metallurgy, Vol. 34, pp. 158-163, 2005.
- Eric, R.H., *Slag properties and design issues pertinent to matte smelting electric furnaces*, Journal of the South African Institute of Mining and Metallurgy, Vol.104, Nr.9, October, 2004 pp.499-510.
- Fluent 6.2 Magnetohydrodynamics (MHD) module manual, January 2005.
- Fluent 6.3, *User's Guide*, September 2006.
- Franke, J., Hellsten, A., Schlünzen and Carissimo, B., *Best practice guideline for the CFD simulation of flows in the urban environment*, COST Action 732, Quality assurance and improvement of microscale meteorological models, 1 May 2007, Retrieved from: [http://www.mi.uni-hamburg.de/fileadmin/files/forschung/techment/cost/cost\\_732/pdf](http://www.mi.uni-hamburg.de/fileadmin/files/forschung/techment/cost/cost_732/pdf).
- Gill, C.B., *Nonferrous Extractive Metallurgy*, Wiley, New York, 1980.
- Hejja, A.A. and Eric, R.H., *Electric conductivity, viscosity and liquidus temperature of slags in electric smelting of copper-nickel concentrates*, Proceedings of 1994 EPD Congress, San Francisco, Warren, G.W. (ed.), Warrendale, Pennsylvania, pp. 621-640, TMS, 1994.
- Hejja, A.A. and Eric, R.H., *Flow and settling phenomena in matte smelting electric furnaces*, Proceedings of 1996 EPD Congress, Anaheim, Warren, G.W. (ed.), Warrendale, Pennsylvania, pp. 27-41, TMS, 1996.
- Hejja, A.A. and Eric, R.H., *Aspects of slag optimization in smelting of Cu-Ni sulphide concentrates*, Proceedings of 1997 EPD Congress, Orlando, Mishra, B. (ed.), Warrendale, Pennsylvania, pp. 179-192, TMS, 1997.
- Henning, B, Shapiro, M., and Le Grange, L.A., *DC Furnace containment vessel design using computational fluid dynamics*, Proceedings of the Tenth International Ferroalloys Congress (INFACON X: 'Transformation through technology'), Cape Town, South Africa, pp. 565-574, 1-4 February 2004.
- Hopkins, S., *Investing in platinum: profit from South Africa's energy squeeze*, discussion posted on Seeking alpha, posted 5 March 2008, Retrieved from: <http://seekingalpha.com/article/67231-investing-in-platinum-profit-from-south-africa-s-energy-squeeze>

- Incropera F.P, De Witt, D.P., *Fundamentals of heat and mass transfer*, Fifth Edition, John Wiley & Sons, Inc, pp. 542 -546, 2002.
- Jardy A., Ablitzer D. Jorget S., *Modelling of slag behavior in non-ferrous smelting electric furnace*, Proceedings of the Reinhardt Schuhmann International Symposium on Innovative Technology and Reactor Design in Extraction Metallurgy, Gaskell D.R., Hager J.P., Hoffman J.E., Mackey, P.J. (eds.), TMS, pp. 419-431, 1986.
- Jio, Q. and Themelis, N.J., *Correlation of Geometric Factor for Slag Resistance Electric Furnaces*, Metallurgical Transactions B, Volume 22B, pp. 183-192, April, 1991.
- Jones, M.T., *Furnace No.1 Slag Bath Modelling*, Lonmin Platinum Process Studies/Furnace Restart Support, Consulting study done by HATCH South Africa, June, 2004.
- Jones, R.T. and Kotzé, I.J., *DC arc smelting of difficult PGM-containing feed materials*, International Platinum Conference, 'Platinum Adding Value', SAIMM, Sun City, South Africa, pp. 33-36, 3-7 October, 2004. Retrieved from:  
<http://www.mintek.co.za/Pyromet/Files/2004JonesConSmelkt.pdf>
- Jones, R.T., *An overview of Southern African PGM smelting*, Nickel and Cobalt 2005: Challenges in Extraction and Production, 44th Annual Conference of Metallurgists, Calgary, Alberta, Canada, pp.147-178, 21-24 August, 2005. Retrieved from  
<http://www.mintek.co.za/Pyromet/Files/2005JobesPGMsmelting.pdf>
- Jones, R.T., *Platinum smelting in South Africa*, South African Journal of Science, Vol. 95, pp. 525-534, November/December, 1999. Retrieved from:  
<http://www.mintek.co.za/Pyromet/Files/Platinum.pdf>
- Llewellyn-Jones, F., *Ionization and Breakdown in Gases*, Methuen and Co. Ltd., London, 1996.
- Matyas, A.G., Francki, R.C., Donaldson, K.M. and Wasmund, B., *Application of new technology in the design of high-power electric smelting furnaces*, The Proceedings of the International Symposium on Non-Ferrous Pyrometallurgy: Trace Metals, Furnace Practices and Energy Efficiency, Bergman R. et al. (eds.), The Metallurgical Society of the Canadian Institute of Mining, Metallurgy and Petroleum, Edmonton, Alberta, Canada, 23-27 August, 1992.
- Mabiza, L., *An overview of PGM smelting in Zimbabwe – Zimplats operations*, Southern African Pyrometallurgy, Jones, R.T., eds., SAIMM, Johannesburg, 5-8 March, 2006.

- Nell, J., *Melting of platinum group concentrates in South Africa*, The Journal of The South African Institute of Mining and Metallurgy, pp. 423-428, August, 2004.
- O'Handley, R.C., *Modern Magnetic Materials – Principles and applications*, Wiley, New York, pp 14 -23, 2000.
- Pan, Y., Sun, S. and Jahanshahi, S., *Efficient and portable mathematical models for simulating heat transfer in electric furnaces*, Sohn International Symposium, Advanced Processing of metals and materials, Vol. 8 - International Symposium on Sulfide Smelting, Kongoli, F. and Reddy, R.G. (eds.), TMS, pp.599-613, 2006.
- Patankar, S.V., *Numerical Heat Transfer and Fluid Flow*, Series in Computational Methods in Mechanics and Thermal Sciences, Minkowycz M.J. and Sparrow, E.M., eds., Hemisphere Publishing Corporation, Washington, 1980.
- Robiette, A.G.E., *Electric smelting processes*, Charles Griffin and Company Limited, 1973.
- Schreiter, T.A., Kempken, J., Degel, R. and Schmieden, H., *Passion for metals*, Southern African Pyrometallurgy, Jones, R.T., eds., SAIMM, Johannesburg, 5-8 March, 2006.
- Sheng, Y.Y., Irons, G.A. and Tisdale, D.G., *Transport phenomena in electric smelting of Nickel matte: Part I - Electric Potential Distribution*, Metallurgical and Materials Transactions B, Vol. 29B, pp. 77-83, 1998.
- Sheng, Y.Y., Irons, G.A. and Tisdale, D.G., *Transport phenomena in electric smelting of Nickel matte: Part II – Mathematical modelling*, Metallurgical and Materials Transactions B, Vol. 29B, pp. 85-94, 1998.
- Shercliff, J.A., *A textbook of magnetohydrodynamics*, Oxford Pergamon, 1965.
- Thiart, G.D., *Postgraduate Course Notes for Numerical Fluid Dynamics 814*, Department of Mechanical Engineering, University of Stellenbosch, January 2007.
- Tseidler, A.A., *Metallurgy of Copper and Nickel*, Ministry of Education of the U.S.S.R., 1958, Translated from Russian by Israel Program for Scientific Translations, pp. 264-272, 1964.
- Utigard, T., *An Analysis of Slag Stratification in Nickel Laterite Smelting Furnaces Due to Composition and Temperature Gradients*, Metallurgical and Materials Transactions B, Volume 25 B, pp. 491-496, August, 1994.

Utigard, T., *Heat and Mass Transfer in Non-Ferrous Smelting Furnaces*, The Brimacombe Memorial Symposium, 1-4 October, pp. 385-396, 2000.

Urquhart, R.C., Rennie, M.S. and Rabey, C.C., *The smelting of copper-nickel concentrates in an electric furnace*, Proceedings of the International Symposium on Copper Extraction and Refining, Las Vegas, NV, Biswas, A.K. and Davenport, W.G. (eds.), TMS-AIME, Warrendale, PA, Feb. 22-26, 1976.

Vermaak, C.F., *The platinum-group metals, a global perspective*, First edition, Mintek, 1995.

Xia, J.L and Ahokainen, T., *Numerical modelling of slag flows in an electric furnace*, Scandinavian Journal of Metallurgy, Vol. 33, pp. 220-228, 2004a.

Xia, J.L., Ahokainen, T. and Kankaanpää, T., *Nickel droplet settling behaviour in an electric smelting furnace*, Metallurgical and Materials Transactions B, Volume 35B, pp. 839-845, October, 2004b.

Young, H.D., *University Physics*, 7<sup>th</sup> edition, Addison Wesley, 1992.



---

# APPENDIX A

## ESTIMATION OF PROCESS MATERIAL PROPERTIES

---

Material properties are needed for representing the materials present in the CFD model. To obtain the most relevant properties, a study of the available relationships was performed and the most appropriate property was selected. The property relationships that are available in literature and that were considered for this study are grouped in this section. This listing could be useful for future modelling attempts.

### A.1 Slag layer thermophysical properties

---

The slag encountered within the smelting of PGM containing nickel sulphide ores can be represented by the characteristics of the  $\text{SiO}_2\text{-FeO-CaO-MgO}$  slag system. It is assumed that the slag does not contain a significantly high concentration of ferric ( $\text{Fe}^{3+}$ ) ions in the form of magnetite such that its effect on the physical properties, especially the slag density and electrical conductivity, will need to be taken into account and require representation by a  $\text{FeO-Fe}_2\text{O}_3\text{-SiO}_2$  slag system. The iron oxide concentration for the current system is below 20 mole pct which implies that conductance due to electrons, induced by the effect of ferric ions, can be neglected [6] and therefore validating the latter assumption.

#### A.1.1 Density [ $\text{kg.m}^{-3}$ ]:

The following sources propose relationships for determining the nonferrous slag density:

- 1.) The relationship representing the measured density of a FeO-MgO-SiO<sub>2</sub> slag system as presented in the study by *Utigard* [12]:

$$\rho(\text{kg}/\text{m}^3) = 2680 + 581 \cdot \frac{\text{wt pct FeO}}{\text{wt pct SiO}_2} - 0.03 \cdot (T - 1450^\circ\text{C})$$

- 2.) Graphical representation obtained from the study done by *Jones* [7] on the Lonmin furnace No.1 that was fitted to a linear relationship (Temperature in °C):

$$\rho(\text{kg}/\text{m}^3) = -0.2514 \cdot T + 3127.7$$

- 3.) The linear relationship presented in the study by *Turkdogan* [11] (Temperature in °C):

$$\rho(\text{kg}/\text{m}^3) = -0.3 \cdot T + 3146$$

- 4.) *Erich* [2] determined the following linear relationship (Temperature in °C):

$$\rho(\text{kg}/\text{m}^3) = -0.38 \cdot T + 3190.35$$

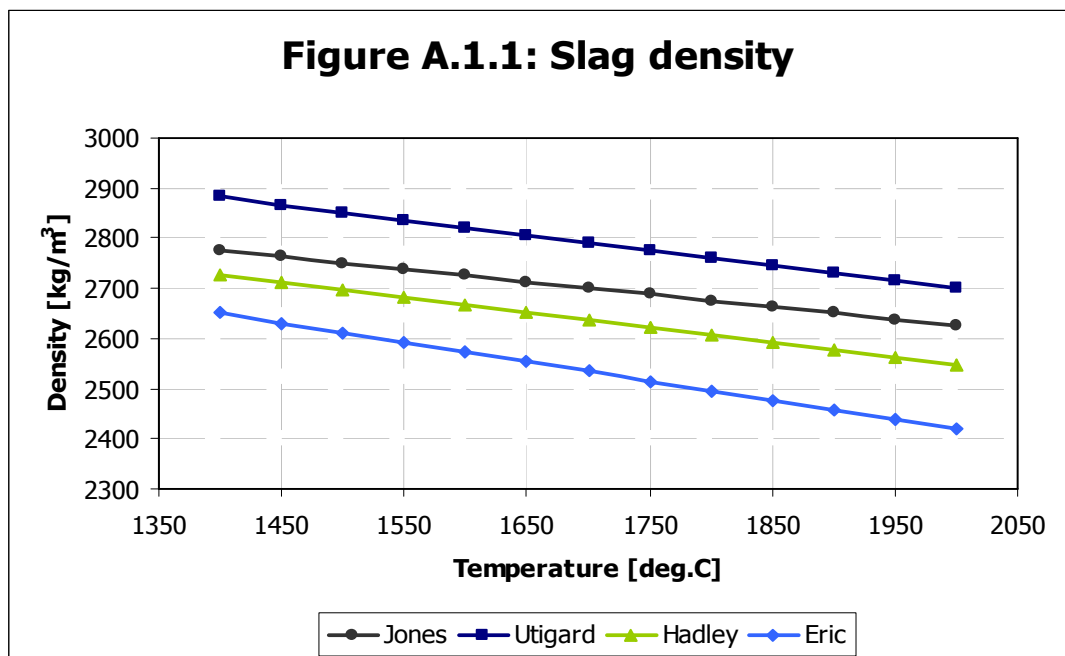


Figure A.1.1. Comparing the various relationships representing the slag density as found in literature.

These relationships were compared, see Figure A.1.1 above, and the relationship proposed by *Jones* [7] was selected for the current CFD modelling since being fairly

recently applied to represent the slag layer of Lonmin furnace No.1, the current system of interest.

### A.1.2 Viscosity [ $\text{kg}\cdot\text{m}^{-1}\cdot\text{s}^{-1}$ ]:

The slag viscosity can be obtained from the following sources:

- 1.) The following relationships for representing the slag viscosity is obtained from the study by *Turkdogan* [11] (Temperature in K):

$$\mu(\text{kg / m.s}) = -11.6447 + \frac{19103}{T}$$

$$\mu(\text{kg / m.s}) = -15.9748 + \frac{26361.5}{T}$$

- 2.) Graphical representation obtained from the consulting study done by *Jones* [7] on the Lonmin furnace No.1 that was fitted to an exponential relationship (Temperature in °C):

$$\mu(\text{kg / m.s}) = 33.377 \cdot e^{-0.0032 \cdot T}$$

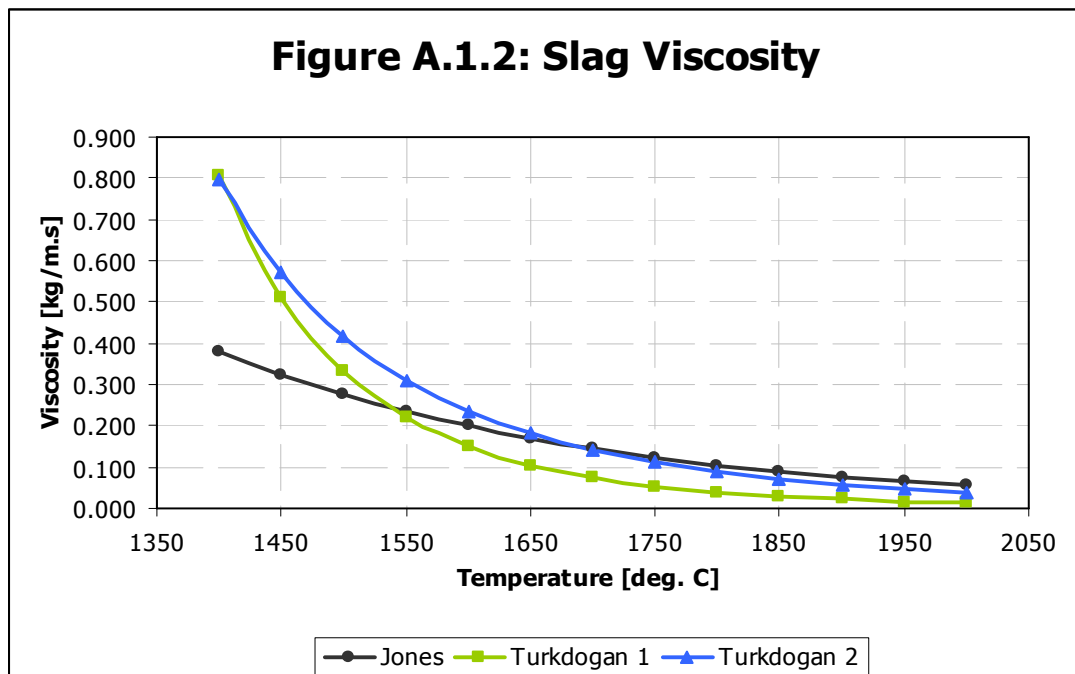


Figure A.1.2. Comparing the various relationships representing the slag viscosity as found in literature.

Similar to the reasoning for selecting the slag density, it is decided to apply the relationship provided by *Jones* [7] for representing the particular slag viscosity.

### A.1.3 Specific Heat Capacity [ $\text{J}\cdot\text{kg}^{-1}\cdot\text{K}^{-1}$ ]:

The specific heat can be obtained from the following sources:

- 1.) The value used for the slag heat capacity in the consulting CFD study by *Jones* [7]: 1 578 J/kg.K.
- 2.) The value used by the On-Line-Heat Balance (OHB) control system for the Lonmin furnace No.1 as retrieved from the operating room on 4 July 2007: 1540 J/kg.K.
- 3.) A value of 1250 J/kg.K was used by *Sheng et al.* [8] for representing the slag at 1250°C.
- 4.) The slag heat capacity based on the weighted average calculated for the first semester of year 2004 (data retrieved from the Furnace No.1 data folder): 1423 J/kg.K. The heat capacities representing the individual components used in this calculation is presented in the following table:

*Table A.1.1 Pure component molecular weight and heat capacity data.*

Component	MW [gram/mole]	Cp [J/mol.K]	Cp [J/kg.K]
SiO <sub>2</sub>	60.09	73.97	1231
CaO	52.08	100.93	1800
MgO	40.30	95.23	2363
Al <sub>2</sub> O <sub>3</sub>	101.96	193.94	1902
FeO	71.85	12.95	180
Cr <sub>2</sub> O <sub>3</sub>	151.99	157.01	1033
Cu <sub>2</sub> S	159.15	97.61	613
FeS	87.91	86.97	989
PGM	195.09	34.75	178
Ni <sub>3</sub> S <sub>2</sub>	240.25	172.62	719
CoS	90.99	44.46	489

- 5.) The approach presented in a confidential study [3] for the estimating the slag heat capacity included the application of a thermodynamic database for calculating the enthalpies of the mixture at different temperatures. Further, a slag melting temperature of 1570°C was assumed and accordingly the latent heats of melting of all minor components present in the slag that melt below 1500°C were grouped into the heat capacity of the solid. Similarly all components melting above 1600°C were

grouped into the heat capacity of the liquid. The result is presented in the following table:

*Table A.1.2 Slag specific heat at various temperatures [3].*

Temperature [°C]	State	Specific Heat [J.Kg <sup>-1</sup> .K <sup>-1</sup> ]
400	Solid	1063
600	Solid	1117
800	Solid	1167
1000	Solid	1211
1200	Solid	1250
1400	Liquid	1373
1600	Liquid	1386
1800	Liquid	1415

Depending on the degree of progress and model complexity, constant values for the heat capacity, as used by *Jones* [7], will be applied initially. The approach presented in the confidential study [3] is used to further the representation of the slag specific heat capacity variation.

#### **A.1.4 Thermal Conductivity [W.m<sup>-1</sup>.K<sup>-1</sup>]:**

The following sources were obtained for representing the slag thermal conductivity:

- 1.) The study by *Jones* [7] used a constant value of  $k = 1.8 \text{ W/m.K}$ .
- 2.) A correlation derived by *Chekhovskoi* [1]:

$$k(\text{W/m.}^\circ\text{C}) = 0.74 + 2.4 \times 10^{-10} \cdot T^3$$

This correlation, developed for a particular coal slag, assumed the convective and electronic components of thermal energy transfer to be negligible and that only the background and radiative modes were responsible for transferring the bulk of thermal energy [3].

- 3.) The study by *Sheng et al.* [8] applied a thermal conductivity of  $8 \text{ W/m.}^\circ\text{C}$ .

The correlation proposed by *Chekhovskoi* [1] compares good with the thermal conductivity used in the CFD modelling by *Jones* [7] on the Lonmin Furnace No.1 and is selected for current modelling purposes.

#### A.1.5 Electrical Conductivity [ $\text{mho}\cdot\text{m}^{-1}$ ]:

The following sources present relationships for modelling the slag electrical conductivity:

- 1.) *Jiao et al.* [6] proposed the following relationships for the conductivity of the nonferrous  $\text{SiO}_2\text{-FeO-CaO-MgO}$  slag system as a function of slag composition as specific temperature:

At  $1500^\circ\text{C}$  the derived correlation for the conductivity [ $\text{mho}/\text{cm}$ ] is as follows:

$$\ln \kappa = -4.45 + 9.15X_{\text{FeO}} + 5.34(X_{\text{CaO}} + X_{\text{MgO}})$$

At  $1400^\circ\text{C}$  the derived correlation for the conductivity [ $\text{mho}/\text{cm}$ ] is as follows:

$$\ln \kappa = -5.21 + 9.92X_{\text{FeO}} + 5.94(X_{\text{CaO}} + X_{\text{MgO}})$$

The Arrhenius law can be used to describe the temperature dependence of the electrical conductivity,  $\kappa$  [6]:

$$\kappa = A \cdot \left( -\frac{E}{R \cdot T} \right)$$

Where E represents the activation energy [J/mole], R the gas constant [J/mol.K] A is a constant and T is the temperature [K]. The expression can be rearranged:

$$\ln \kappa = \ln A - \frac{E}{R \cdot T}$$

To obtain a temperature dependent relationship using the above correlations, the electrical conductivity is evaluated at  $1500^\circ\text{C}$  and  $1400^\circ\text{C}$  respectively and used to determine the activation energy,  $E = -0.0363$  J/mole.

The resulting thermophysical property having units of  $\text{mho}/\text{m}$ :

$$\kappa = 17.64 \cdot e^{[-0.00437(1673-T)]}$$

- 2.) The confidential study [3] used the following relationship obtained from the National Institute of Metallurgy for a "Type A (SiO<sub>2</sub>-FeO-CaO-MgO) + 6% Fe<sub>2</sub>O<sub>3</sub>" slag. The electrical conductivity expressed in units mho/m and  $T$  in Kelvin:

$$\kappa = 100 \cdot e^{\left(-\frac{13140}{T} + 6.067\right)}$$

- 3.) The modelling done by *Sheng et al.* [8] used a constant value of 30 mho/m obtained at 1250°C.
- 4.) The study conducted in fulfilment for a Masters of Science degree by *Hundermark* [4] performed an investigation on the factors affecting the electrical conductivity of slags containing the relevant components, Al<sub>2</sub>O<sub>3</sub>, CaO, Cr<sub>2</sub>O<sub>3</sub>, FeO<sub>x</sub>, MgO and SiO<sub>2</sub>. The following relation for the electrical conductivity (mho/cm) of a slag containing two or more of the mentioned components, was formulated:

$$\begin{aligned} \ln \kappa = & \left(19.9 - \frac{47348}{T}\right) \cdot X_{\text{Al}_2\text{O}_3} + \left(15.4 - \frac{24087}{T}\right) \cdot X_{\text{CaO}} + \left(9.2 - \frac{14151}{T}\right) \cdot X_{\text{MgO}} \\ & + \left(-0.5 - \frac{7478}{T}\right) \cdot X_{\text{SiO}_2} + \left(10.0 - \frac{9140}{T}\right) \cdot X_{\text{FeO}} \cdot \text{Fe}^{2+} \\ & + \left(65.4 - \frac{82447}{T}\right) \cdot X_{\text{FeO}}^2 \cdot \text{Fe}^{2+} \cdot \text{Fe}^{3+} + \left(-2.6 + \frac{6642}{T}\right) \cdot X_{\text{FeO}} \cdot \text{Fe}^{3+} \end{aligned}$$

For the above correlation,  $T$  represents the temperature in Kelvin,  $X$  the mole fractions of the components and Fe<sup>2+</sup> and Fe<sup>3+</sup> the fractions of the ferrous and ferric ions respectively.

The relationships above are compared and found to be in fairly good comparison (See Figure A.1.3 below). For the comparison a zero concentration of the ferric ion (Fe<sup>3+</sup>) was assumed, therefore eliminating the last two terms of the correlation developed by *Hundermark* [4]. It is found that the relationships by *Hundermark* and that used in the confidential study [3] compares very well. It is therefore decided to apply the relationship as used in the confidential study [3] due to its relative simplicity and the fact that the effect of Fe<sub>2</sub>O<sub>3</sub>, although approximate, is taken into account when compared to the complete negligence of the relationship developed by *Jiao et al.*

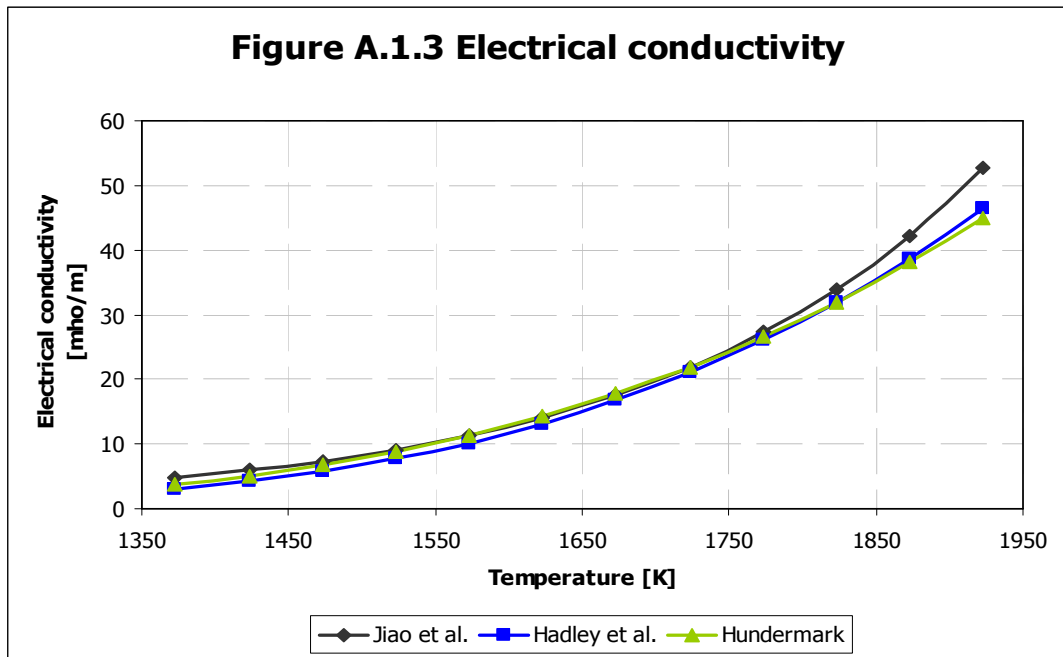


Figure A.1.3. Comparing the various relationships representing the slag electrical conductivity as found in literature.

## A.2 Matte layer thermophysical properties

As stated within the Literature Review, computational modelling work on base metal mattes is very few or not readily available. A review study at the University of Stellenbosch, *Sundström et al.* [10], was recently conducted for estimating the temperature-composition dependent relationships for density, viscosity and surface-and interfacial tension of base metal mattes.

### A.2.1 Density [ $\text{kg}\cdot\text{m}^{-3}$ ]:

The following options are available for representing the matte density:

- 1.) The study by *Sundström et al.* [10] present the following density-temperature-composition relationship for the (Cu-Ni)-Fe-S ternary system:

$$\rho_{matte} = 6358 - 76.3[S] + 9.94[Cu + Ni] - 0.4645(T - 1000^\circ\text{C})$$

For this relationship  $T$  is the process temperature in  $^\circ\text{C}$  and the element composition in mass pct as indicated in square brackets. This relationship presents a maximum error confidence level of 4.3% within a temperature range between  $1100^\circ\text{C}$  and  $1300^\circ\text{C}$ . For the current system of interest the expression reduces to:



$$\rho_{matte} = 4487.99 - 0.4645(T - 1000^{\circ}C)$$

- 2.) For modelling purposes, the consulting study [3] extrapolated a linear density vs. temperature coefficient of  $0.5 \text{ kg/m}^3\text{.}^{\circ}C$ , developed between the temperature range  $1200\text{-}1300^{\circ}C$ . A resulting density of  $4217\text{kg/m}^3$  was applied.
- 3.) The work by *Sheng et al.* [8] uses a matte density of  $4500\text{kg/m}^3$  at  $1250^{\circ}C$ .

Although current operation will require the density relationship to be applied outside the range for which it was developed, the relationship proposed by *Sundström et al.* [10] is selected for modelling.

### A.2.2 Viscosity [ $\text{kg.m}^{-1}.\text{s}^{-1}$ ]:

The following is presented as alternatives for estimating the matte viscosity:

- 1.) The following graphical representation for the viscosity profiles representing the  $\text{FeS-Ni}_3\text{S}_2$  sulphide matte system was obtained from the study by *Sundström et al.* [10]. Further profiles for the  $\text{Cu}_2\text{S-Ni}_3\text{S}_2$  and  $\text{Cu}_2\text{S-FeS}$  systems are also provided but since  $\text{Cu}_2\text{S}$  is of lower concentration compared to  $\text{FeS}$  and  $\text{Ni}_3\text{S}_2$ , the  $\text{FeS-Ni}_3\text{S}_2$  is considered more representative of the present matte system.

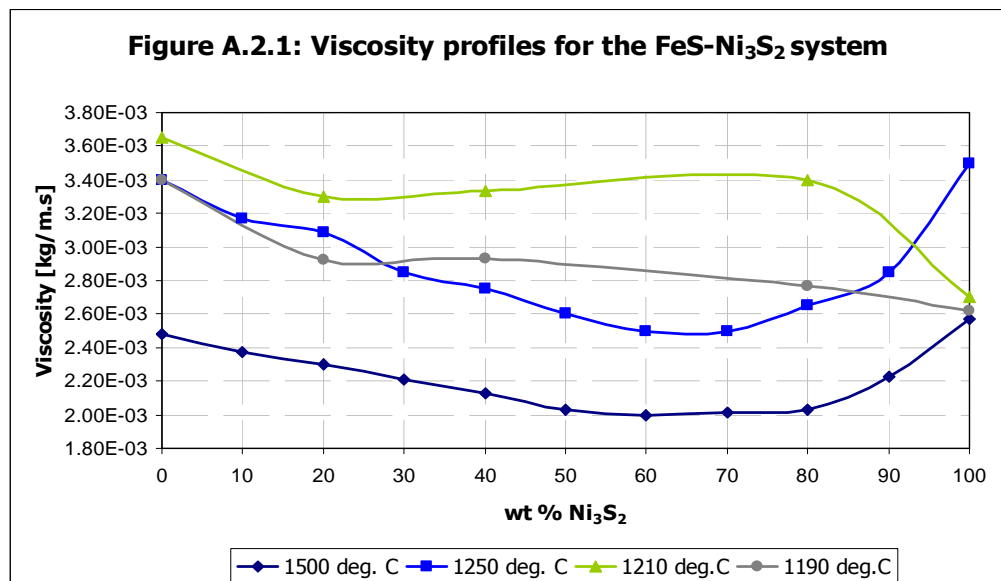


Figure A.2.1. Comparing the various relationships representing the slag viscosity as found in literature.

The dynamic viscosity obtained from the above graph at the applicable Ni<sub>3</sub>S<sub>2</sub> concentration (23%) is 0.00229 kg/m.s at 1500°C and 0.0031 kg/m.s at 1250°C.

- 2.) A confidential study [3] applied a constant matte viscosity of 0.0032 kg/m.s at 1300°C.
- 3.) A viscosity of 0.05 kg.m<sup>-1</sup>.s<sup>-1</sup> at 1250°C was used by *Sheng et al.* [8].

The dynamic viscosity obtained from the studies by *Sundström et al.* and the confidential CFD study [3] is in close comparison. A value for 0.0032 kg/m.s is applied for representing the matte dynamic viscosity.

### A.2.3 Specific Heat Capacity [J.kg<sup>-1</sup>.K<sup>-1</sup>]:

The few options for estimating the matte viscosity are:

- 1.) A value of 890 J/kg.K is employed by the Online Heat Balance (OHB) control system of the Lonmin Furnace No.1.
- 2.) A study [3] used the same approach for estimating the slag heat capacity when determining matte heat capacity. For this case, the latent heats of melting for all components melting below 1100°C (Co<sub>3</sub>S<sub>4</sub> and Ni<sub>3</sub>S<sub>2</sub>) were grouped under the heat capacity of the solid. Similarly the latent heats of melting for all components melting above 1200°C (Al<sub>2</sub>O<sub>3</sub>, CaSiO<sub>3</sub>, CrS, FeO, MgSiO<sub>3</sub> and SiO<sub>2</sub>) were grouped under the heat capacity of the liquid. The results are presented in the following table:

*Table A.2.1 Slag specific heat at various temperatures [3].*

Temperature [°C]	State	Specific Heat [J.Kg <sup>-1</sup> .K <sup>-1</sup> ]
400	Solid	815
600	Solid	811
800	Solid	780
1000	Solid	722
1200	Liquid	871
1400	Liquid	812
1600	Liquid	744
1800	Liquid	667

- 3.) The study by *Sheng et al.* [8] applied a value of 720 J/kg.K for the matte heat capacity.

A similar approach for modelling the matte specific heat capacity will be followed to that discussed for the slag. The value employed by the OHB will be applied initially followed by similar modelling done in the confidential study [3] depending on the model progression.

#### **A.2.4 Thermal Conductivity [ $\text{W}\cdot\text{m}^{-1}\cdot\text{K}^{-1}$ ]:**

A constant thermal conductivity of 17 W/m.K was used by *Sheng et al.* [8]. The value is applied for all modelling purposes due to the lack of alternative sources.

#### **A.2.5 Electrical Conductivity [ $\text{mho}\cdot\text{m}^{-1}$ ]:**

The isothermal electrical conductivity ( $\kappa$ ) of  $9.3 \times 10^4$  mho/m was used by *Sheng et al.* [8]. As with the thermal conductivity, this is the only account for estimating the matte electrical conductivity and is therefore used for current modelling purposes.

### **A.3 Concentrate layer physical properties**

---

The information presented in a confidential CFD study [3] was used for estimating the properties of the concentrate layer:

#### **A.3.1 Density [ $\text{kg}\cdot\text{m}^{-3}$ ]:**

The bulk density of the milled concentrate is reported to be 1400 kg/m<sup>3</sup> [3], and applied.

#### **A.3.2 Specific Heat Capacity [ $\text{J}\cdot\text{kg}^{-1}\cdot\text{K}^{-1}$ ]:**

The specific heat was calculated in a similar manner as the slag and matte heat capacities. The results are presented in the following table:

*Table A.3.1 Slag specific heat at various temperatures [3].*

Temperature [°C]	Specific Heat [ $\text{J}\cdot\text{Kg}^{-1}\cdot\text{K}^{-1}$ ]
800	1030
1000	1068
1200	1103
1400	1133

### A.3.3 Thermal Conductivity [ $\text{W}\cdot\text{m}^{-1}\cdot\text{K}^{-1}$ ]:

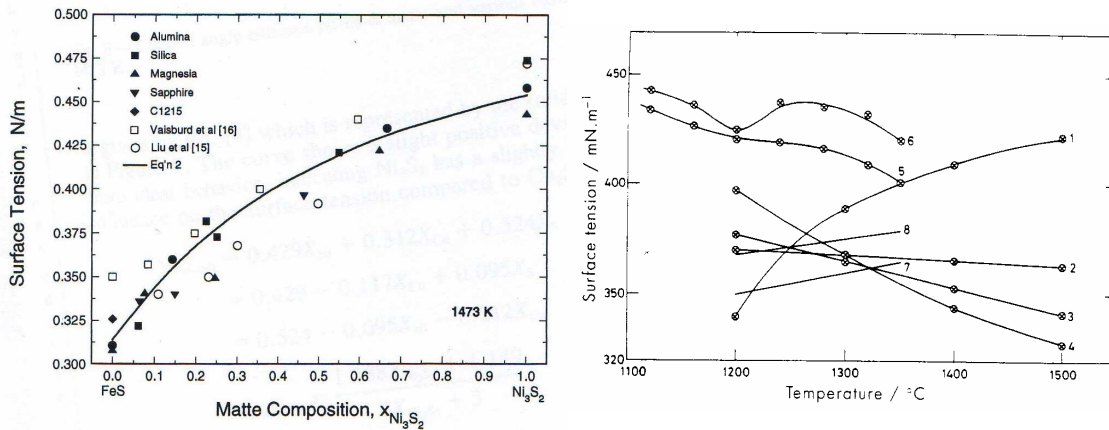
A value of  $1.2 \text{ W/m}\cdot\text{K}$  was applied for modelling the concentrate layer thermal conductivity.

### A.3.4 Electrical Conductivity [ $\text{mho}\cdot\text{m}^{-1}$ ]:

A value of  $1.2 \text{ mho/m}$  was used [3].

## A.4 Slag-matte surface tension estimation

The surface tension along the interface between the slag and matte phase was taken as  $0.4\text{N/m}$ . The surface tension is an average value based on the respective matte and slag surface tensions. The graphs depicted below were used to estimate the surface tension. It can be seen that the matte surface tension vary between  $0.3$  and  $0.5\text{N/m}$  due to composition changes while the slag surface tension exerts a slight variation due to temperature, between  $0.32$  and  $0.45\text{N/m}$  for the temperature range of  $1100$  to  $1500^\circ\text{C}$



Figures A.4.1 a and b. (a) Matte surface tension variation with composition [5], (b) Slag surface tension variation with temperature [9].

## A.5 References

---

- [1] Chekhovskoi, V. and Ulashchik, A.N., *Thermal Conductivity of Slags in the Solid and Liquid States*, *Teplofizika Vysokikh Temperatur*, English, High Temperature, Vol. 25, p.924, 1987.
- [2] Eric, R.H., *Separation, Settling and Flow Phenomena in Electric Smelting of Cu-Ni Concentrates*, *Scandinavian Journal of Metallurgy*, Vol. 34, pp. 158-163, 2005.
- [3] Report containing a confidential CFD consulting study, obtained by the University of Stellenbosch, 2006.
- [4] Hundermark, R., *The Electrical Conductivity of Melter Type Slags*, MscEng Thesis, University of Cape Town, June 2003.
- [5] IP, S.W. and Toguri, J.M., *Surface and Interfacial Tension of the Ni-Fe-S, Ni-Cu-S and Fayalite Slag System*, *Metallurgical Transactions B*, Volume 24B, pp. 657-668, August 1993,.
- [6] Jiao, Q. and Themelis, N.J., *Correlations of Electrical Conductivity to Slag Composition and Temperature*, *Metallurgical Transactions B*, Volume 19B, pp. 133-140, February, 1988.
- [7] Jones, M.T., *Furnace No.1 Slag Bath Modelling*, Lonmin Platinum Process Studies/Furnace Restart Support, Consulting study done by HATCH South Africa, June, 2004.
- [8] Sheng, Y.Y., Irons, G.A. and Tisdale, D.G., *Transport phenomena in electric smelting of Nickel matte: Part II - Mathematical modelling*, *Metallurgical and Materials Transactions B*, Vol. 29B, pp. 85-94, 1998.
- [9] *Slag atlas*, 2<sup>nd</sup> edition, Verlag Stahleisen, Düsseldorf, 1995
- [10] Sundström, A.W. and Eksteen, J.J., *Review of Viscosity, Density, Surface-and Interfacial Tension of Base Metal Mattes*, University of Stellenbosch, 2005
- [11] Turkdogan, E.T., *Physicochemical Properties of Molten Slags and Glasses*, The Metals Society, ISBN 0 904357 54 6, 1983.

- [12] Utigard, T., *An Analysis of Slag Stratification in Nickel Laterite Smelting Furnace Due to Composition and Temperature Gradients*, Metallurgical and Materials Transactions B, Volume 25B, pp. 491-496, August, 1994.

---

# APPENDIX B

## SUPPORTING CALCULATIONS

---

The supporting calculations referred to in the text of the main thesis body are presented in this section.

### B.1 Comparison between buoyancy and Lorentz forces

---

The method presented in Davidson (2001) p. 324-329 and p. 346-347 is followed to determine whether the flow residing in the molten bath is buoyancy or Lorentz force driven flow:

#### B.1.1 Buoyancy driven flow:

The equations of motion and the energy conservation are applied to a streamline close to the wall boundary where the temperature gradient is expected to give rise to buoyant flow. The continuity equation including buoyancy is as follows:

$$\frac{\partial \vec{V}}{\partial t} = -\nabla \left( \frac{P}{\rho} \right) - g\beta(T - T_M)\delta_{ij} + \nu \nabla^2 \vec{V} \quad (\text{B.1})$$

Where  $\beta$  is the thermal expansion coefficient and  $\delta_{ij}$  the Kronecker delta such that if  $\delta_{ij} = 1$  if  $i=j$  and 0 otherwise. The transport equation for heat is,

$$\frac{\partial T}{\partial t} = \alpha \nabla^2 T \quad (\text{B.2})$$

In the above equation  $\alpha$  is the thermal diffusivity. It can be shown that Equations B.1 and B.2 require that the following relations hold for approximating the velocity at the thermal boundary,  $u_b$ :

$$u_b^2/L_T \sim g\beta\Delta T \quad u_b/L_T \sim \alpha/\delta^2 \quad (\text{B.3, 4})$$

If it is further assumed that the core of the thermal boundary is stratified (only varying in the z direction), the energy equation permits:

$$u_{zc}T_c'(z) = \alpha T_c''(z) \quad (\text{B.5})$$

This is used along with the continuity equation presented above, Equation B.1 to approximate the velocity at the core of the thermal boundary layer:

$$u_c \sim \alpha/L_T \quad u_c R \sim u_b \delta \quad (\text{B.6, 7})$$

Equations B.4 to B.7 along with the definition of the Grashof number (Gr) are used to derive the required scaling law for the velocity at the thermal boundary:

$$u_b \sim \frac{\alpha}{R} (Gr)^{3/7} \quad (\text{B.8})$$

### B.1.2 Lorentz-Force driven flow:

To close the loop on a comparison, the velocity brought about by the Lorentz forces in the matte is estimated by integrating  $\vec{F}$  along a streamline close to the furnace wall or hearth, which can be shown to be the following:

$$\oint \vec{F} \cdot d\vec{l} \sim K/2R^2 \quad (\text{B.9})$$

Where K is:

$$K = \frac{\mu I^2}{4\pi^2 \rho} \quad (\text{B.10})$$

If it assumed that electrode radius is small compared to the radius of the vessel, the integration of Equation B.9 at the wall can be shown to reveal:

$$\frac{K}{2R^2} \sim \frac{\pi R}{2} \frac{\tau_w}{\rho \delta_w} \quad (\text{B.11})$$



For which  $\tau_w$  and  $\delta_w$  are the wall shear stress and the characteristic length scale for the gradients of shear stress near the wall. The eddy velocity can be estimated by  $\tau_w/\rho \sim (u')^2$  and therefore Equation B.11 converts to:

$$\frac{K}{2R^2} \sim \frac{\pi R}{2} \frac{(u')^2}{\delta_w} \quad (\text{B.12})$$

From practical experience, Davidson offers the following estimates, typical for induction furnaces, to estimate the velocity brought about by the movement of charge:

$$u' \sim u/3.5 \quad \delta_w \sim R/10 \quad (\text{B.13, 14})$$

The induced velocity can therefore be approximated by:

$$u \sim 0.6 \frac{K^{1/2}}{R} \quad (\text{B.15})$$

### **B.1.3 Buoyancy-Lorentz force driven flow transition criteria:**

The transition point between buoyancy driven flow and electromagnetic induced flow could be estimated by equating Equations B.8 and B.15. The resulting dimensionless parameter will therefore be an indication whether flow would be driven by buoyancy or the Lorentz forces:

$$\chi = \frac{K^{1/2}(Gr)^{-3/7}}{\alpha} \quad (\text{B.16})$$

The surface tension along the interface between the slag and matte phase was taken as  $\sigma = 0.1 \text{ N/m}$ . The transition to Lorentz driven flow will therefore result once  $\chi$  exceeds unity. It is reported by Davidson that classical buoyancy-driven flow occurs at  $\chi$  values less than  $\sim 0.4$ . This dimensionless parameter was evaluated for the matte layer and found to be in the order of 0.4-0.6 when assuming 75% of the current to pass through the matte layer.

## B.2 Flow criteria within the slag bath

---

The estimation of the flow regime through buoyancy within the bulk of the slag requires the evaluation of the Raleigh number, which describes the relative effect of buoyancy and the viscous forces acting on the fluid:

$$Ra = Gr \cdot Pr \quad (B.17)$$

Where

$$Gr = g \cdot L^3 \frac{\rho^2}{\mu^2} (T_c - T_w) \cdot \alpha \quad (B.18)$$

and

$$Pr = \frac{\mu \cdot c_p}{k} \quad (B.19)$$

To evaluate the Grashoff number (Gr), the slag density was calculated at 2725.46 and 2624.90 kg/m<sup>3</sup> according to the temperature dependant relationship identified in Appendix A.1 for the temperature range between 1327°C and 1727°C respectively. The viscosities at these temperatures were estimated at 0.478 and 0.132 kg/m.s. The value for the expansion coefficient,  $\alpha$ , was determined using a linear approach [Hejja and Eric, 1995]:

$$\rho_T = \rho_0 [1 - \alpha(T - T_0)] \quad (B.20)$$

For the mentioned temperatures and densities, an expansion coefficient of  $9.67 \times 10^{-5}/^\circ\text{C}$  was calculated.  $T_w$  is the wall temperature but for the estimation is considered to be the lowest temperature of the slag.  $T_c$  the highest temperature expected in the slag was taken to be 1727°C. The Gr number can be found to be between  $1.23 \times 10^7$  and  $1.5 \times 10^8$ . The Pr number would be between 139.62 and 285.76 for a thermal conductivity,  $k$ , ranging from 1.3 to 2.3W/mK and heat capacity,  $c_p$ , taken at an average value of 1375J/kg.K.

The Ra number therefore falls within the range of  $1.63 \times 10^6$  and  $1.98 \times 10^7$  when assuming a characteristic length scale of 1m. The transition between laminar and turbulent flow occurs at  $Ra = 10^9$ , therefore proving flow resulting from natural buoyancy in the slag to be laminar [Incropera and De Wit 2002]. As stated in the Chapter 5, predominant laminar flow was also estimated for slag flow in a rectangular electric smelting furnace by Hejja and Eric (1995).

---

# APPENDIX C

## USER DEFINED FUNCTIONS (UDF's)

---

The UDF's were programmed in C++ language and converted to C language format as to be compatible with the Fluent interface. An extract of the UDF library that was used for the furnace model is provided within this section.

### C.1 Current input

As an example, the electrical current input specified for electrode 1 is presented.

```
// elec1_input.cpp
//

#include "udf.h"

#define CURR 40000
#define VOLUM 0.87875
#define FREQ 0.0167
#define PI 3.1415927

DEFINE_SOURCE(j_source1_40,c,ct,ds,eqn)
{
    real source1;
    source1 = CURR/VOLUM*sin(2*PI*FREQ*CURRENT_TIME-240*PI/180);
    ds[eqn] = 0.0;
    return source1;
}
```

### C.2 Slag energy sink

The energy sink associated with concentrate getting heated up when descending from the concentrate layer was portrayed by the following UDF:

```

// Energy_sink_1.cpp //
#include "udf.h"

DEFINE_SOURCE(e_sink_slag,c,t,dS,eqn)
{
    real temper = C_T(c,t);
    real source1;

    if (temper > 1523)
    {
        source1 = -((8.32)*1373*(temper-1523))/118.4031;
    }
    else
    {
        source1 = 0;
    }

    C_UDMI(c,t,46) = source1;
    return source1;
}

```

### C.3 Concentrate energy sink

The energy consumption due to smelting and heat-up of concentrate as it descends towards the slag layer is accounted these UDF's. The UDF for representing the central smelting zone of the concentrate (zone1) is taken as an example of the four UDF's written for this purpose with each having different accounts for the smelting energy due to the allocation of different smelting zones.

```

// Energy_sink_1.cpp
//
#include "udf.h"

#define cp_slag 1100

DEFINE_SOURCE(e_sink_conc_z1,c,t,dS,eqn)
{
    real temper = C_T(c,t);
    real source2;

    if (temper > 1524)
    {
        source2 = -((3.336)*cp_slag*(temper-1523) + 770400)/1.694;
    }
    else
    {
        source2 = 0;
    }

    return source2;
}

```

## C.4 Energy sink for the electrodes

Overheating of the sold electrodes, which were assigned similar properties to that of the slag, was prevented by applying a similar energy sink to the electrode volumes as to the slag volume. This UDF is however only a rough approximation since similar mass flow-rates were applied to the electrodes and the slag layer.

```
// Energy_sink_1.cpp
//

#include "udf.h"

#define cp_slag 1373
#define m_slag 8.32

DEFINE_SOURCE(e_sink_slag_out, c, t, dS, eqn)
{
    real temper = C_T(c, t);
    real source3;

    if (temper > 1523)
    {
        source3 = -abs(m_slag*cp_slag*(temper-1523)/0.878);
    }
    else
    {
        source3 = 0;
    }

    return source3;
}
```

---

# APPENDIX D

## RESIDUAL MONITORING

---

An extract of the residual monitoring for the complete and final model is provided. The variable residuals for single time step is seen to fall well below the convergence criteria specified in the solution controls, except the value of the electric potential residual which was specifically specified at a low convergence criteria to enable ten complete iterations for allowing the electrical current to sufficiently diffuse through the domain. The three injections of the discrete phase particles for the particular time-step are also reported. The amount of particles injected is close to the amount of particles escaping from the system, indicating steady state. Examples of the residual monitoring plot obtained for the models with and without turbulence modelling are provided in the figures to follow.

```
Injecting 560 particles at t = 4953.3
Injecting 608 particles at t = 4953.3
Injecting 500 particles at t = 4953.3
  iter continuity x-velocity y-velocity z-velocity      energy      uds-0      time/iter
Injecting 444 particles at t = 4953.3
number tracked = 5690, escaped = 2111, aborted = 0, trapped = 0, evaporated = 0, incomplete = 0
Parallel particle tracking concurrency: 33%

219420 2.8295e-05 9.2333e-05 1.8213e-04 9.2458e-05 1.0194e-07 1.7182e-07 0:03:48 10
219421 4.5706e-03 3.3547e-03 6.7960e-03 3.1701e-03 5.9693e-06 5.4183e-06 0:03:09 9
219422 2.6828e-04 4.7363e-03 8.3496e-03 4.5928e-03 1.1551e-07 6.1337e-06 0:02:50 8
219423 1.2447e-04 1.9094e-03 3.3131e-03 1.8515e-03 1.4997e-07 3.3848e-06 0:02:31 7
219424 9.3378e-05 7.2101e-04 1.4103e-03 7.0014e-04 1.1375e-07 2.1186e-06 0:02:10 6
219425 7.6385e-05 3.2680e-04 7.7098e-04 3.1926e-04 1.0716e-07 1.3656e-06 0:01:49 5
219426 6.2857e-05 2.1382e-04 5.4870e-04 2.1070e-04 1.0488e-07 8.9250e-07 0:01:27 4
219427 5.1181e-05 1.7083e-04 4.2033e-04 1.6924e-04 1.0413e-07 5.8537e-07 0:01:06 3
219428 4.1629e-05 1.4071e-04 3.2257e-04 1.3978e-04 1.0387e-07 3.8408e-07 0:00:44 2
219429 3.4132e-05 1.1458e-04 2.4273e-04 1.1426e-04 1.0399e-07 2.5339e-07 0:00:22 1
```

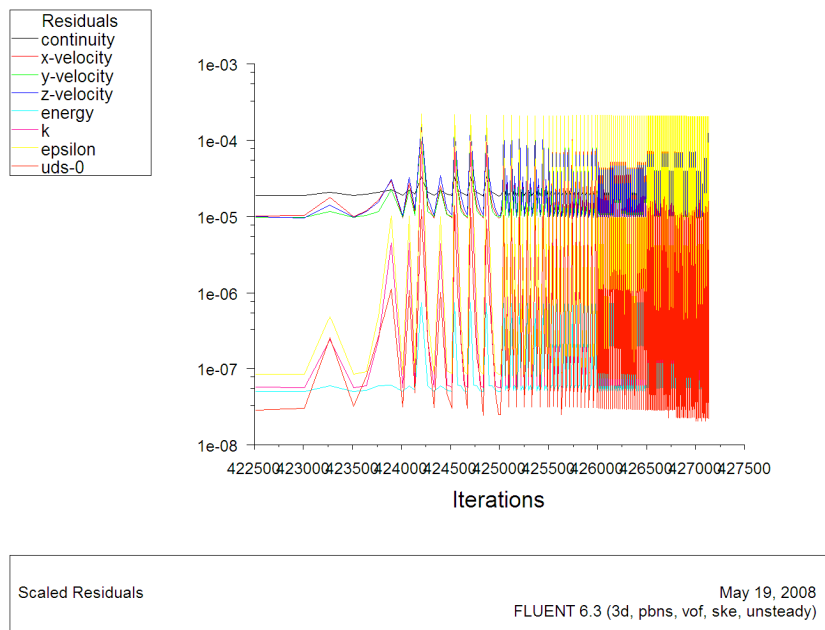


Figure D.2 Example of the scaled residual plot maintained throughout the simulation process for the model where turbulence modelling was included.

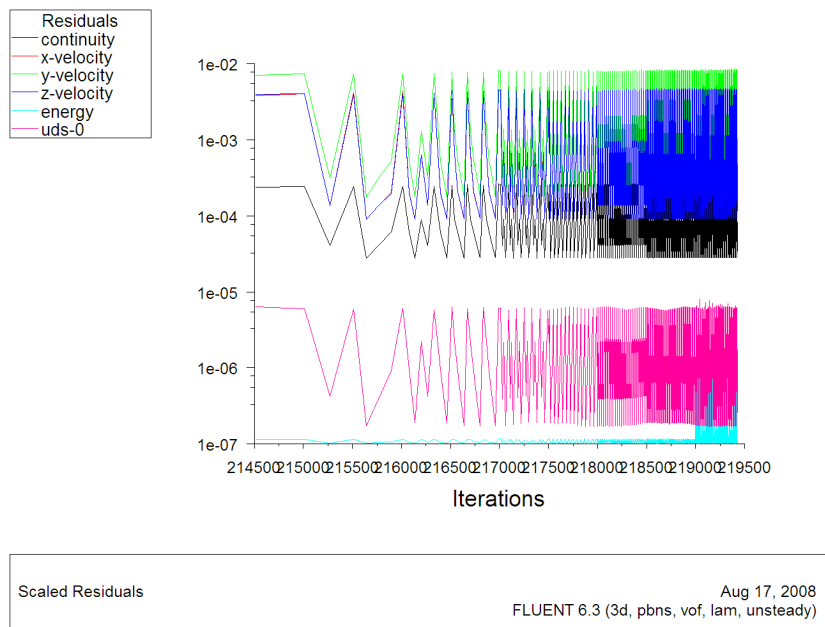


Figure D.2 Example of the scaled residual plot maintained throughout the simulation process for the complete and final model.